UNIVERSIDAD POLITÉCNICA DE MADRID
Escuela Técnica Superior de Ingenieros de Caminos, Canales y Puertos

Analysis of the Mechanical Behavior of PA12 Lattice Materials Fabricated by Additive Manufacturing

D O C T O R A L T H E S I S

Submitted for the degree of Doctor by:

Lucía Cobián González
Master in Materials Engineering

Madrid, 2024


UNIVERSIDAD POLITÉCNICA DE MADRID
Escuela Técnica Superior de Ingenieros de Caminos, Canales y Puertos

Doctoral Degree in Engineering of Structures, Foundations and Materials

Analysis of the Mechanical Behavior of PA12 Lattice Materials Fabricated by Additive Manufacturing

D O C T O R A L T H E S I S

Submitted for the degree of Doctor by:

Lucía Cobián González
Master in Materials Engineering

Under the supervision of:
Dr. Javier Segurado Escudero
Dr. Miguel A. Monclús Palazón

Madrid, 2024

Title: Analysis of the Mechanical Behavior of PA12 Lattice Materials Fabricated by Additive Manufacturing

Author: Lucía Cobián González

Doctoral Programme: Engineering of Structures, Foundations and Materials

Thesis Supervision:

Dr. Javier Segurado Escudero, Catedrático de Universidad, Universidad Politécnica de Madrid / Senior Researcher, IMDEA Materials (Supervisor)

Dr. Miguel A. Monclús Palazón, Senior Research Associate, IMDEA Materials

External Reviewers:

Jesús Rodríguez Pérez, Universidad Rey Juan Carlos

Fernando Naya Montáns, Universidad Carlos III

Thesis Defense Date:

This thesis has been supported by the European Union's Horizon 2020 research and innovation programme for the project "Multi-scale Optimisation for Additive Manufacturing of fatigue resistant shock-absorbing MetaMaterials (MOAMMM)", grant agreement No. 862015, of the H2020- EU.1.2.1. - FET Open Programme.

To my dogs, Zira and Nala

Acknowledgement

I want to express my gratitude to my supervisor, Prof. Javier Segurado, for allowing me to do research with him and for his excellent advice, invaluable guidance, and continuous support. My deepest gratitude goes to my other supervisor, Dr. Miguel Monclus, for his assessment and advice and also for helping me with the project, mainly the experiments. I would sincerely thank Dr. Juan Pedro Fernandez-Blazquez for his invaluable help with the experiments and for generously sharing his extensive knowledge of polymer science. I sincerely thank Mohib Mustafa for his collaboration and assistance, which has made this journey much smoother and more enjoyable. Dr. Sergio Lucarini and Dr. Ling Wu have dedicated their time to explaining everything related to the project and advising me whenever I needed it, and for that, I am extremely grateful. I am truly thankful to Prof. Eric Maire for welcoming me into his research team during my PhD stay in Lyon and for providing me with all the necessary resources and support throughout my research. I would also like to acknowledge the work of Anthony Voitus and Gabriel Zarzoso.

Thanks to all the members of the MOAMMM project's consortium, Prof. Zoltan Major and Prof. Issam Doghri's research groups, the *cirp* team led by Thomas Lück, and in particular to Prof. Ludovic Noels, without whom the project would not have been possible.

Special thanks to Dr. Javier García, Dr. Vanesa Martinez, and José Luis Jiménez for their exceptional technical support in the laboratory. Their dedication surpasses the highest standards of accuracy and quality, and their assistance was invaluable. Last but not least, I wish to extend my heartfelt thanks to my IMDEA colleagues, especially my friends Adrian, Maral, and Thomas, for their warm welcome, support, and the positive environment they created.

Abstract

Lattice materials, composed of the repetition of cells made of struts, can be designed to achieve high specific stiffness and energy absorption with minimal weight. Recent improvements in additive manufacturing allow the fabrication of lattice cells using standard Selective Laser Sintering at the millimetric scale. However, these components often contain internal defects, such as porosity, affecting mechanical properties. It is generally observed that smaller cell sizes tend to reduce the lattice's effective elastic modulus, yet the cause of this size effect is not well understood. The objective of this work is to comprehensively analyze the non-linear behavior of PA12 lattice materials by combining experimental analysis and full-field simulations.

The bulk response of PA12 is characterized experimentally with uniaxial tensile, compression, and shear tests at different strain rates, temperatures, and aging times, combined with microscopic testing techniques such as nanoindentation to calibrate a finite strain VEVP material model that predicts its behavior. Results show that PA12 exhibits a viscoelastic-viscoplastic response, moderate strain rate sensitivity in yield stress, and anisotropy under tension.

In the study of the mechanical behavior of printed PA12 single struts, unit cells, and lattices of different sizes, it was found that smaller lattice cells exhibit a lower effective elastic modulus, a "smaller means softer" trend typical of SLS polymers. Compression tests, nanoindentation, X-ray tomography, DSC, WAXS, SAXS, and numerical simulations determined that this modulus reduction is not only due to defects like porosity or roughness. Instead, but is also results from a combination of incomplete particle melting and nanostructural changes from the printing process, as confirmed by micro- and nanostructural characterizations.

Experimental and numerical studies on the fracture and deformation of PA12 lattice structures revealed that defects from porosity, surface roughness, and strut geometry significantly affect mechanical properties. In-situ tensile and compressive tests on single struts and unit cells showed that lattice stiffness is lower than in bulk PA12. Fractures in single struts were initiated at random surface or internal defects, with crack propagation influenced by printing direction, while fractures in unit cells were mainly influenced by geometry. Numerical simulations using voxelized RVEs from X-ray tomographies, applying FFT and phase-field fracture models, confirmed that surface defects, print orientation, and structural geometry impact the stiffness and failure behavior of PA12 lattices in a complex way. The non-linear response was predicted with FFT using a VEVP material model with calibrated parameters for the bulk and strut scale, closely predicting the material's behavior.

Beyond build orientation in SLS, other printing parameters like contour and hatching settings strongly influence the mechanical properties of AM components, especially near the machine's resolution limit. These factors influence particle coalescence and thermal history, affecting the annealing effect in printed parts. These findings apply to commercial machines optimized for larger samples. Optimizing the parameters for microscale components could minimize defects and coalescence issues, reducing size effects. This study helps understand the critical features for designing lattice meta-materials by linking mechanical behavior to component size, and the methods used could also characterize other polymers in bulk and lattice forms.

Resumen

Estructuras de celosía, compuestas por la repetición de celdas hechas con barras, pueden diseñarse para lograr alta rigidez específica y capacidad de absorción de energía con un peso muy bajo. Los avances en fabricación aditiva permiten producir estas estructuras mediante Sinterización Selectiva por Láser (SLS) a escala milimétrica. Estos componentes suelen presentar defectos, como porosidad, que afectan sus propiedades mecánicas. Se observa que los tamaños más pequeños de celda reducen el módulo elástico efectivo de la estructura, aunque la causa de este efecto de tamaño no está aun comprendida por completo. Este trabajo tiene como objetivo analizar a fondo el comportamiento no lineal de las estructuras de celosía de PA12 combinando análisis experimentales y simulaciones de campo completo.

La respuesta del PA12 masivo se caracteriza experimentalmente con ensayos uniaxiales de tracción, compresión y cizalla a diferentes velocidades de deformación, temperaturas y tiempos de envejecimiento, combinadas con nanoindentación para calibrar un modelo de material VEVP con grandes deformaciones que predice su comportamiento. Los resultados muestran que el PA12 exhibe un comportamiento viscoelástico-viscoplástico, sensibilidad moderada a la velocidad de deformación en el límite elástico y anisotropía en tracción.

En el estudio del comportamiento mecánico de barritas individuales, celdas unitarias y estructuras de celosía de diferentes tamaños impresas con PA12, se encontró que cuanto más pequeñas las celdas, más bajo es su módulo elástico efectivo, exhibiendo la tendencia "más pequeño significa más blando" típica de los polímeros SLS. Los ensayos de compresión, nanoindentación, tomografía por rayos X, DSC, WAXS, SAXS y simulaciones numéricas determinaron que esta reducción del módulo no se debe solo a defectos como la porosidad o la rugosidad, si no que también es el resultado de una combinación de fusión incompleta de partículas y cambios en la nanoestructura derivados del proceso de impresión.

Los estudios experimentales y numéricos sobre la fractura y deformación de estructuras de celosía de PA12 mostraron que los defectos y geometría de las barras afectan considerablemente a las propiedades mecánicas. Los ensayos in-situ de tracción y compresión revelaron que la rigidez de las celdas es menor que la del PA12 masivo. Las fracturas en las barras ocurrieron tanto en defectos internos o superficiales, con la dirección de impresión influyendo en la propagación de las grietas. En las celdas, la geometría tuvo mayor impacto. Las simulaciones numéricas confirmaron que los defectos superficiales, la orientación de impresión y la geometría afectan la rigidez y el comportamiento de fallo de las celosías. Las predicciones de la respuesta no lineal se realizaron con FFT y un modelo VEVP calibrado para las escalas macro y micro, prediciendo con precisión el comportamiento del material.

Más allá de la orientación durante la impresión con SLS, otros parámetros de impresión como las configuraciones de contorno y relleno influyen fuertemente en las propiedades mecánicas de los componentes AM, especialmente cerca del límite de resolución de la máquina. Estos factores afectan la coalescencia de partículas y la historia térmica, lo que influye en el efecto de recocido en las piezas impresas. Estos hallazgos son aplicables a máquinas comerciales optimizadas para muestras más grandes. Optimizar los parámetros para componentes a escala microscópica podría minimizar los defectos y problemas de coalescencia, reduciendo

los efectos del tamaño. Este estudio ayuda a comprender las características críticas para diseñar materiales meta-lattice al vincular el comportamiento mecánico con el tamaño del componente, y los métodos utilizados también podrían caracterizar otros polímeros en forma masiva y en celosía.

Table of Contents

Acknowledgement v
Abstract vi
Resumen vii
List of Figures xi
List of Tables xviii
Abbreviations and acronyms xxi

1 Introduction **1**
1.1 Mechanical Metamaterials 1
1.1.1 Metamaterials: Definition, origin, classification, research and industry interest 1
1.1.2 Classification and properties of mechanical metamaterials 2
1.2 Additive Manufacturing 10
1.2.1 Processes and technologies 11
1.2.2 Challenges and limitations 14
1.3 Estimation of the mechanical response of lattice materials by numerical simulation 15
1.4 Motivation 17
1.5 Objectives and approach 18

2 Materials and experimental methods **19**
2.1 Polyamide 12 (PA12) 19
2.2 Sample preparation 22
2.2.1 Sample fabrication: Selective Laser Sintering (SLS) 22
2.2.2 Sample characteristics and details 22
2.3 Equipment used for uniaxial tensile and compression tests 23
2.3.1 Universal Testing Machine 24
2.3.2 Gleeble 25
2.3.3 Hopkinson Split Pressure Bar 25
2.4 Dynamic mechanical analysis 26
2.5 Nanoindentation 27
2.5.1 Quasi-static nanoindentation and nano-impact tests 27
2.5.2 Nanoindentation mapping 29
2.6 Thermogravimetric analysis 30
2.7 X-ray tomography 30

2.7.1 Porosity calculation . . . 31
2.8 Differential scanning calorimetry . . . 32
2.9 X-ray scattering: WAXS and SAXS . . . 33

3 Numerical analysis techniques 37
3.1 FFT based computational homogenization: The FFTMAD code . . . 37
3.1.1 Galerkin adapted for Lattice Materials . . . 38
3.2 Finite Element adaptation based homogenization . . . 39
3.3 Generation of representative volume elements for simulations . . . 39
3.3.1 RVE generation from tomographies . . . 39
3.3.2 Parametric RVE generation for as-designed geometries . . . 41
3.3.3 FE Mesh Generation . . . 42
3.4 Phase field fracture implementation in FFTMAD . . . 42
3.5 Non-linear response: Finite strains Viscoelastic - Viscoplastic material model 44
3.5.1 Kinematics . . . 44
3.5.2 Viscoelastic part . . . 44
3.5.3 Viscoplastic part . . . 45
3.5.4 Bayesian inference to fit the parameters for the VEVP model . . . 46

4 Multiscale characterization of bulk PA12 49
4.1 Mechanical characterization . . . 49
4.1.1 Uniaxial tensile tests . . . 49
4.1.2 Uniaxial compression tests . . . 50
4.1.3 Conventional relaxation tests . . . 51
4.1.4 Single hysteresis loops . . . 51
4.1.5 Consecutive loading–unloading compression tests . . . 52
4.1.6 Shear tests . . . 53
4.1.7 PA12 mechanical behavior at high temperature . . . 54
4.1.8 Mechanical behavior of aged PA12 . . . 56
4.1.9 Strain Rate Sensitivity of PA12 . . . 59
4.2 Dynamic mechanical analysis of PA12 . . . 61
4.2.1 Isofrequency curves . . . 61
4.2.2 Master curves . . . 63
4.3 Nanoindentation tests for dynamic analysis of PA12 on the macroscopic scale 64
4.3.1 Comparison between nanoindentation values and macro-scale values . 67

5 Characterization of PA12 on lattices and the microscopic scale 69
5.1 Mechanical analysis . . . 69
5.1.1 BCC lattices . . . 69
5.1.2 Unit cells . . . 70
5.1.3 Single struts . . . 72
5.2 Exploring the origins of the size effect in unit cells . . . 73
5.2.1 Effect of humidity on struts . . . 73
5.2.2 Effect of surface roughness and porosity . . . 74
5.2.2.1 Scanning electron microscopy . . . 75

5.2.2.2 X-ray tomography . . . 76
5.2.2.3 Numerical analysis of unit cells and lattices . . . 80
5.2.2.4 Summary . . . 83
5.2.3 Effect of particle coalescence and annealing during additive manufacturing 84
5.2.3.1 Microstructural characterization by nanoindentation mapping 85
5.2.3.2 Differential scanning calorimetry . . . 86
5.2.3.3 Small and wide-angle X-ray scattering . . . 89
5.2.3.4 Summary . . . 92
5.3 From unit cells to lattices . . . 93
5.3.1 Postprocessing after manufacturing . . . 94
5.3.2 Annealing effect during additive manufacturing on the lattices . . . 94
5.3.2.1 Summary . . . 96

6 In-situ experiments and high fidelity simulations 97
6.1 Experimental results from in-situ tests . . . 98
6.1.1 Experimental set-up . . . 98
6.1.2 Experimental results of struts . . . 100
6.1.3 Experimental results of unit cells . . . 102
6.2 Linear elastic-fracture simulations . . . 104
6.2.1 Struts . . . 104
6.2.2 Unit cells . . . 107
6.3 Elasto-visco plastic simulations . . . 107
6.3.1 Model calibration . . . 108
6.3.2 Struts and unit cells simulations . . . 110

7 Conclusions 113
7.1 Future work . . . 116

Bibliography 119

Annex 1 131

Annex 2 135

Annex 3 137

List of Figures

1.1 Graph showing the number of publications about metamaterials published yearly by Elsevier journals. Data obtained from ScienceDirect, 2024. 2
1.2 Principles, main categories, and properties of mechanical metamaterials. (a) Formation of mechanical metamaterials at the material to structural levels. Categories of mechanical metamaterials based on the microstructures and their typical applications. (b) Extraordinary mechanical characteristics of mechanical metamaterials (Jiao et al., 2023). 3
1.3 Some examples of unit cells where the struts arrangement gives them specific properties and behaviors.Two lattice examples at the bottom. 4
1.4 Shoesole and helmet prototypes made with lattice materials developed in the MOAMMM project. 5
1.5 Graph showing the number of publications about lattice/truss materials, published yearly by Elsevier journals. Data obtained from ScienceDirect, 2024. . 6
1.6 Schematic of the structure and the unit cell of relative density for the chiral, anti-chiral, and hierarchical honeycombs studied by Mousanezhad et al., 2016. 7
1.7 Origami-inspired foldable structures (a) Miura origami-inspired canopy (Huang et al., 2023), and (b) tessellated Crystalline-Si solar cell module (Sim et al., 2021). 8
1.8 Examples of pattern transformation metamaterials. (a) Bi-stable auxetic metamaterials based on square and triangular cut motifs studied by Rafsanjani and Pasini, 2016, and (b) phase transforming pattern of elastomeric blocks used in the work by Yang et al., 2016. 9
1.9 Graph showing the number of publications about lattice/truss materials by Elsevier journals and AM technologies patents published yearly. Data obtained from ScienceDirect, 2024 and EPO, 2023. 10
1.10 Schematic figures showing (a) material jetting and (b) binder jetting manufacturing processes. Own elaboration. 12
1.11 Schematic figures showing (a) material extrusion and (b) directed energy deposition processes. Own elaboration. 12
1.12 Schematic figures showing (a) sheet lamination and (b) vat photopolymerization processes. Own elaboration. 13
1.13 Scheme of the powder bed fusion process. Own elaboration. 14

2.1 Condensation reaction between an amine and a carboxylic acid. 20

2.2 PA12 chemical formula 20
2.3 Polyamide 12 (a) α and (b) γ crystal forms. The dashed lines represent hydrogen bonds between the amide groups. 21
2.4 First set of samples. Specimen geometries corresponding to (a) tensile specimens for tests at room temperature (left) and 45ºC (right),(b) compression samples for different strain rates, (c) shear specimens, and (d) samples for dynamic mechanic analysis. Black arrows and the planes formed by these arrows in (c) correspond to layer directions. 23
2.5 Second set of samples. Specimen geometries corresponding to (a) single strut specimens with different orientations and diameters placed on a sample holder for SAXS/WAXS measurements, (b) unit cell geometries, and (c) 10x10x10 lattices composed of different strut diameters for compression testing. 24
2.6 Split-Hopkinson Pressure Bar (SHPB) set up for compression testing. Own elaboration. 25
2.7 Samples used for DMA tests showing the layer directions and the applied oscillating load 27
2.8 Schematics of pendulum-based nanoindentation system. 28
2.9 Schematic representation of X-ray tomography. 30
2.10 Centre cross sections slices from A1 tomographic images and digital design, where (a) is the tomography, (b) is the binary version of the tomography, (c) is the contour of the tomography, and (d) is the as-designed volume 31
2.11 Schematic representation of X-ray scattering on a semicrystalline sample. . . 33
2.12 Schematic representation comparing WAXS and SAXS analysis techniques. . 34
2.13 Schematic of polymer chains arrangement showing the dimensions of d-spacing (d), measured by WAXS and long spacing (L) dimensions estimated by SAXS. 35

3.1 Process for obtaining the RVE for FFT simulations from tomographic volumes. In this case a slide of a single 1.5 mm diameter strut is shown. 40
3.2 Volume reconstruction of the tomographies from the PA12 samples, where (a) is a 3D tomography of part of an auxetic unit cell, (b) the reconstructed auxetic volume, (c) is a 3D tomography of a BCC unit cell, and (d) the reconstructed BCC cell volume. 41
3.3 Example of parametric generation of a lattice unit cell, where (a) is the voxelized geometry, (b) is the voxelized geometry with the phase map implemented, and (c) is the volume mesh. 41

4.1 Average stress-strain curves of PA12 bulk material of different tests and at different strain rates; (a) tensile σ-ε curves, (b) compressive σ-ε curves, (c) relaxation curves, and (d) single hysteresis curves. The curves have been obtained by calculating the average stress on each strain point of every experimental curve. 52
4.2 Cyclic compressive true stress-strain curves of PA12 (a) at different strain rates and (b) detail of the first cycle. 53
4.3 Average shear stress-strain curves at different building directions. 54

4.4 Average stress-strain curves of PA12 at 45 ℃ for uniaxial (a) tensile tests on the parallel (V), (b) tensile tests on the perpendicular (H) direction, and (c) compression tests. 55
4.5 Comparison between (a) elastic modulus, (b) yield stress, (c) ultimate tensile stress, and (d) elongation at break of tensile samples from batch 1 tested at room temperature after 1.6 (blue) and 41 (red) months since printed. 59
4.6 Linear regression of the logarithms of tensile and compressive yield stress and strain rate as a function of strain rate of non-aged PA12 tested at room temperature. 60
4.7 Single cantilever DMA experiments at 1, 3, and 10 Hz. Heating rate 2 ℃/min and deflection of 30 µm. (a) Storage modulus and (b) tan δ of non-aged PA12 samples printed with H and V directions. (c) Storage modulus and (d) tan δ of 41 months aged PA12 samples printed on both directions. 62
4.8 Master curves of PA12 samples printed on both directions obtained from single cantilever DMA frequency sweep experiments. Heating rate 2 ℃/min and deflection of 20 µm. Master curves for (a) storage modulus and (b) tan δ at room temperature, and for (c) storage modulus and (d) tan δ at 45 ℃. . . . 63
4.9 (a) SLS printed octet-like lattice structure; (b) Lattice structure embedded in the resin mount; (c) Array of indentation imprints performed at different maximum loads; (d) Optical image of the strut and node surface area enclosed by the yellow rectangle in (b): the location of selected indentations performed in the node area is enclosed within the red rectangle. 64
4.10 a) Force-displacement curves from quasi-static nanoindentation (colored lines) and nano-impact (black lines). Each nano-impact curve corresponds to each of the impact conditions. Higher impulse force leads to higher applied forces and maximum depths. (b) Strain rate signals for quasi-static nanoindentation (colored lines) and nano-impact (black lines) tests. 65
4.11 Apparent hardness values as a function of indenter penetration depth of quasi-static and nano-impact indentation tests. 66
4.12 a) Apparent hardness as a function of strain rate. The red dot represents the average of the nano-impact values. (b) Compression yield stress was predicted using the inverse analysis in the work Rueda-Ruiz, 2021 and the nanoindentation results. 67

5.1 (a) Average stress-strain curves at $1.5 \times 10^{-3}\ s^{-1}$ of (a) lattices and (b) unit cells. The labels on the legends for each curve refer to the diameter of the strut in mm. 70
5.2 Mechanical tests of single struts. a) Average stress-strain curves of single struts at $2.78 \times 10^{-3}\ s^{-1}$ and b) tensile curves at different strain rates of 1.5 mm diameter struts. 72
5.3 Weight loss and second derivative curves obtained from TGA analysis for (a) bulk sample and (b) 0.7 mm diameter strut. The percentage values shown in each graph correspond to the water content in each sample. 74

5.4 SEM images of 1mm diameter unit cells and lattice struts. (a) Non-treated unit cell, (b) surface-treated unit cell, (c) strut from the center of the lattice, (d) strut from the edge of the lattice, (e) magnification of the central strut, and (f) magnification of the perimeter strut. 76
5.5 Thresholded longitudinal cross-sections from X-ray tomography. (a) single struts with different printing directions and diameters (0.7 - 1.5 mm), where the cylinder drawings at the bottom indicate the layer direction deposited in horizontal (H), vertical (V), and oblique (T), (b) unit cells with strut diameters of 0.5 - 1.5 mm. V.S. refers to vapor smoothing. 78
5.6 Stress map of lattice 10x10x10, simulated with FEM. Stress units in MPa. . 81
5.7 Stress maps over tomographic RVEs of unit cells with diameter struts of a) 0.5 mm, b) 0.7 mm, c) 1.0 mm and d) 1.5 mm. Stress units in MPa. 83
5.8 Optical microscopy images (up) and micromechanical maps (down) obtained by nanoindentation of (a) powders, (b) node from a 1.0 mm strut diameter lattice structure, and (c) macroscopic sample. The rectangle on the optical microscopy images represents the area corresponding to the nanoindentation maps. 85
5.9 DSC thermograms of PA12 samples. The y-axis is inverted. (a) Full DSC curve from old powders and (b) melting peaks of all samples. 88
5.10 Graphs presenting WAXS patterns, peak deconvolution, and identification of the crystalline peaks and amorphous phase (discontinuous line) of PA12 samples of (a) melt with slow cooling (M.s), (b) melt and quenched (M.q), (c) old powder and (d) 1 mm diameter single strut. 89
5.11 Graphs obtained from WAXS patterns of a) height difference between $\gamma_{(001)}$ and γ_m peaks of all samples, and b) evolution of d-spacings calculated for $\gamma_{(001)}$ and γ_m directions from printed samples only. 91
5.12 Graphs from SAXS showing a) SAXS patterns of powders and all 1 mm struts obtained from different geometries, and b) long spacing thickness estimations. 92

6.1 In-situ experimental setup for (a) tensile tests on the struts and (b) compression tests on the BCC unit cells. 98
6.2 Experimental force-displacement curves from single strut in-situ tests with X-ray tomography. 100
6.3 Analysis of strut tested with DVC in (a) the initial state and (b) the step before failure. 101
6.4 Single strut of 1.0 mm diameter with layers in the V direction. S indicates a crack originated in the surface, and P indicates a crack originated in an internal pore. 101
6.5 Stress strain curves of unit cells from X-ray in-situ tests. 103
6.6 Cross section from the final step of in-situ tests with X-ray tomography of unit cells with (a) 0.7 mm diameter struts without surface treatment, (b) 1.0 mm diameter struts without surface treatment, (c) 0.7 mm diameter struts with surface treatment, and (d) 1.0 mm diameter struts with surface treatment. . 103

6.7 Tomographic volume of 1 mm strut printed in oblique direction used for porosity analysis and diameter measurements where (a) raw gray-scale tomography slice, (b) reconstruction from original tomography including defects, and (c) reconstruction with no pores. The reconstructed volume is virtually cut in the middle of the sample for this figure. 104
6.8 Stress-strain curves from the experimental DVC test and predictions using PFF with different parameters. 105
6.9 Sample used for DVC. Up: RVE with pores, Middle: fracture prediction using RVE with pores, and Down: fracture prediction using RVE without pores. Where sdv1 indicates the damage phase field. 105
6.10 Strut of 1.5 mm diameter with layers in T direction showing raw tomographies of the initial and before failure states, and the fracture predictions using different parameters. 106
6.11 Damage prediction on the as-designed BCC unit cell RVE. Where sdv1 indicates the damage phase field. 107
6.12 Non-linear behavior prediction using VEVP model on 1.5 mm diameter single struts using microscopic parameters. 111
6.13 Non-linear behavior prediction using VEVP model on (a) BCC unit cell with 1.5 mm diameter struts using microscopic parameters, and (b) BCC unit cell with 5.0 mm diameter struts using bulk parameters. 112

1 Particle size distribution analysis data of (a) new and (b) old powders. . . . 132
2 SEM images of (a) new and (b) old powders, and magnified images of (c) new and (d) old particle powders. 133

3 Graphs presenting WAXS patterns, peak deconvolution and identification of the crystalline peaks and amorphous phase (discontinuous line) of a) old powders, b) new powders. 138
4 Graphs presenting WAXS patterns, peak deconvolution and identification of the crystalline peaks and amorphous phase (discontinuous line) of the melts with a) slow cooling, b) quenching. 138
5 Graphs presenting WAXS patterns, peak deconvolution and identification of the crystalline peaks and amorphous phase (discontinuous line) of single struts of 0.5 mm diameter a) T, b) V, c) H. 138
6 Graphs presenting WAXS patterns, peak deconvolution and identification of the crystalline peaks and amorphous phase (discontinuous line) of single struts of 0.7 mm diameter a) T, b) V, c) H. 139
7 Graphs presenting WAXS patterns, peak deconvolution and identification of the crystalline peaks and amorphous phase (discontinuous line) of single struts of 1.0 mm diameter a) T, b) V, c) H. 139
8 Graphs presenting WAXS patterns, peak deconvolution and identification of the crystalline peaks and amorphous phase (discontinuous line) of single struts of 1.5 mm diameter a) T, b) V, c) H. 139

9 Graphs presenting WAXS patterns, peak deconvolution and identification of the crystalline peaks and amorphous phase (discontinuous line) of a) 1 mm diameter lattice strut and b) bulk sample. 140

List of Tables

2.1 General properties of PA12 and range of values for the properties of the most common polyamides: PA6, PA66, PA610, PA11, and PA12 (Domininghaus, 1993). The properties, from top to bottom, are water absorption (H_2O absorption), yield stress (σ_y), elongation at break (A%), elastic modulus (E, melting point (T_m), and glass transition temperature (T_g). 20

4.1 Average tensile mechanical properties of PA12 with standard deviation determined following ISO 527-1. 50
4.2 Average compressive mechanical properties of PA12, determined following ASTM D695-15 for low and medium $\dot{\varepsilon}$. For high $\dot{\varepsilon}$, σ_y was obtained by finding the point with maximum slope change in the σ-ε curves. 50
4.3 Average shear properties of PA12 with standard deviation, determined following ASTM 7078M-05 standard. Offset and ultimate shear strength are τ_y and τ_u, respectively. 54
4.4 Average tensile mechanical properties of PA12 at 45 ℃ with standard deviation. 56
4.5 Average compressive mechanical properties of PA12 at 45 ℃ with standard deviation. 56
4.6 Table showing the batches used for the aging study, their fabrication date, testing dates, and the time passed between fabrication and testing. 57
4.7 Comparison of average compressive properties, with standard deviation, between non-aged and aged samples. Values obtained from compressive $\sigma - \varepsilon$ curves. 57
4.8 Average tensile properties with a standard deviation of aged PA12 after 41 months. 1/41 mo states for batch 1 and 41 months. 58
4.9 Strain rate sensitivity factor n of PA12 at room temperature (RT), 45 ℃, and aged 22.4 and 41 months. 61
4.10 Hardness (H) and indentation modulus (E_r) obtained from the nanoindentation test over a wide range of strain rates. The maximum force (Max. F) in the case of the nano-impact tests is the impulse force applied at a distance of 20 µm resulting in the strain rates shown in Figure 4.10b. 66

5.1 Dimensions of unit cell samples. 71
5.2 Effective stiffness and ultimate compressive strength of unit cells obtained from compression tests at $1.5 \times 10^{-3}\ s^{-1}$. 71
5.3 X-Ray tomography scan resolution for each type of sample. 77

5.4 Comparison of theoretical and measured diameters from single struts, where H, V, and T represent the layer directions perpendicular, parallel, and oblique to the strut length, respectively. Measurements of struts from unit cells were not possible. . . . 79
5.5 Porosity from single struts calculated from tomographies. . . . 80
5.6 Porosity of unit cells calculated from tomographies. V.S. refers to vapor smoothing and NON to non-surface treated. . . . 80
5.7 Effective elastic modulus predictions of unit cells using defect-free (CAD design) and tomographic RVEs. Material parameters are inputs for the material model, and the predicted stiffness is the one obtained in the simulation. E_{macro} represents the effective Young's modulus value obtained from the macroscopic characterization, whereas $E_{diameter}$ is the input material parameter used with each of the respective RVEs to obtain the closest values to the experimental results of the respective unit cell sizes. . . . 82
5.8 PA12 average modulus of powder, strut, and macroscopic samples nanoindented areas. . . . 86
5.9 Melting points, melting enthalpy and crystallinity of powders, melt samples, and 3D printed samples. . . . 87

6.1 Strain rate and displacement for each step of the in-situ compression tests of unit cells with 0.7 and 1.0 mm struts diameter. . . . 99
6.2 Bulk material loading conditions used for BI . . . 108
6.3 Uniform distribution ranges of the viscoelastic material parameters. Where $i = 1, ..., 8$, the units of G_i and K_i are MPa, and g_1 and k_1 are s. . . . 109
6.4 Viscoelastic material parameters for the macro and micro scale obtained with Bayesian inference fitting after using MAP. . . . 109
6.5 Uniform distribution ranges of the viscoplastic material parameters for the macroscale (bulk level) and the microscale (strut level). Where η is in MPa $\cdot$ s, and t_0, c_0, H_t^0 and H_c^0 are in MPa. . . . 110
6.6 Viscoplastic material parameters for the macro and micro scale obtained with Bayesian inference fitting after using MAP. . . . 110

1 EOS PA2200 highlighted properties from the material data sheet available at EOSGmbH, 2024 webpage. . . . 131
2 Average particle size of EOS PA2200 new, mix and old powder. D50 means that 50 % of particles are smaller and larger than the specific value. . . . 131

3 Average tensile properties with a standard deviation of aged PA12 after 22 months. . . . 135

Abbreviations and acronyms

ν	Poisson's ratio
2D	Two-Dimensional
3D	Three-Dimensional
AM	Additive Manufacturing
BCC	Body-Centred Cubic
BI	Bayesian Inference
DIC	Digital Image Correlation
DMA	Dynamic Mechanical Analysis
DSC	Differential Scanning Calorimetry
DVC	Digital Volume Correlation
E	Young's Modulus
FEM	Finite Element Method
FFT	Fast Fourier Transform
G	Shear Modulus
K	Bulk Modulus
MCMC	Markov Chain Monte Carlo
PA12	Polyamide-12
PDF	Probability Distribution Function
RVE	Representative Volume Element
SHPB	Split-Hopkinson Pressure Bar
SLS	Selective Laser Sintering
T_g	Glass transition temperature
TGA	Thermogravimetric analysis
TTSP	Time-Temperature Superposition Principle

UCS Ultimate compressive stress

UPM Universidad Politécnica de Madrid

UTS Ultimate tensile stress

VEVP Viscoelastic-Viscoplastic

Chapter 1

Introduction

This thesis is focused on the experimental characterization and numerical simulation of polymer-based lattice materials. The research presented here has been performed in the framework of a European project, FET-Open MOAMMMM.

This work starts with an introductory chapter, Chapter 1, which provides the reader with an overview of metamaterials and additive manufacturing, exploring their main advances and current challenges. Through the introduction, both the achievement and present challenges are examined, along with potential research routes to overcome these obstacles. The motivation and objectives will also be introduced in Chapter 1. Chapters 2 and 3 will present the experimental and numerical techniques implemented, respectively. The results obtained from the material characterization in the macroscopic scale, the microscopic scale, and the analysis of the effect of fabrication defects will be discussed in Chapters 4, and 5. Chapter 6 will include a discussion and comparison between the cracking process observed during in-situ tests and the predictions obtained in simulations with phase-field fracture. In Chapter 6, the mechanical response observed during the characterization in the micro-scale and the non-linear response simulated with a viscoelastic-viscoplastic material model will also be explored. The conclusions of the work will be summarized in Chapter 7, which will end with a section dedicated to the activities related to improvements for future work.

1.1 Mechanical Metamaterials

1.1.1 Metamaterials: Definition, origin, classification, research and industry interest

Metamaterials are artificial materials designed to have properties that are not found in nature. These manufactured materials can exhibit unique properties and fulfill multifunctional requirements with a combination of specified mechanical, thermal, optical, and acoustic properties, leading to applications in some engineering and industry fields (Yu et al., 2018; Al-Othman et al., 2022).

The metamaterial concept was first proposed by the Russian theorist Veselago in 1968 for

magnetic properties. The researcher hypothesized the existence of artificial materials with negative permeability (forms a magnetic dipole in the opposite direction to the imposed magnetic field, and negative permittivity (property of a metal whose frequency band is below its plasma frequency) was theoretically possible (Veselago, 1968). Still, it was not until 1995 that Prof. Sir John Pendry suggested a way to manufacture structures with negative permittivity and permeability (Pendry et al., 1999). In 2000, D. R. Smith et al., 2000 experimentally showed that a periodic array of the structures proposed by Prof. Pendry could exhibit negative permeability and permittivity simultaneously at the same frequency. Since then, the research interest in metamaterials has rapidly escalated in many different areas, including physics, materials science, chemistry, and engineering (Guo and Luo, 2023). The scientific interest in the area can be illustrated by the increasing number of publications in metamaterials in the last two decades, as represented in Figure 1.1.

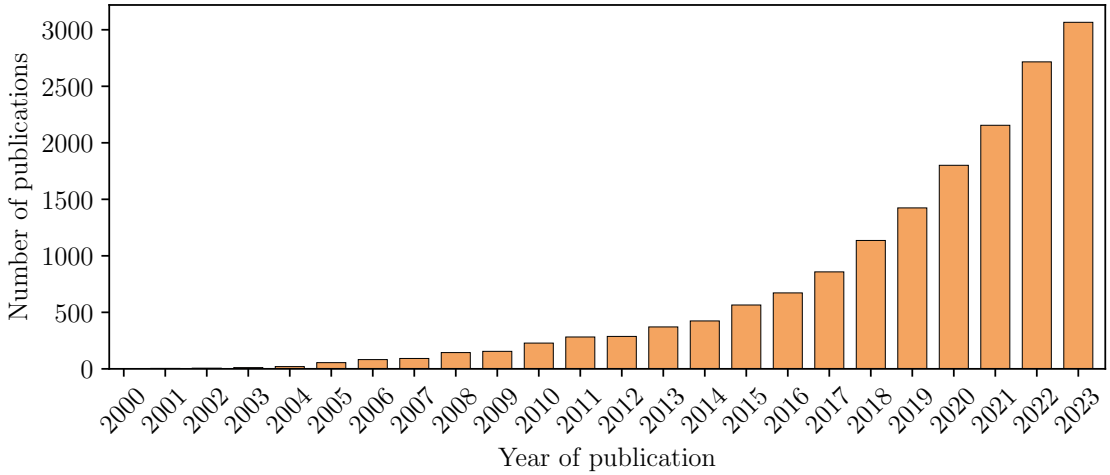

Figure 1.1: Graph showing the number of publications about metamaterials published yearly by Elsevier journals. Data obtained from ScienceDirect, 2024.

The industrial interest in metamaterials is also very clear and is also progressively increasing. In 2016, the market size was 316 USD million, with an expected market growth of 18 % from 2017 to 2025. By 2022, the market size was 900 USD million, and the market growth rate from 2023 to 2032 is expected to be 32 %, with a market size expected to increase to 14500 USD million by 2032. According to the end use, the leading industries are automotive, military, electronics, and medical. (GrandViewResearch, 2016; PrecedenceResearch, 2022).

1.1.2 Classification and properties of mechanical metamaterials

Metamaterials can be classified into four main types: optical, acoustic, thermal, and mechanical, depending on the properties modified by their design (Yu et al., 2018). Contrary to other metamaterial types whose behavior mainly depends on the properties of the materials they are made from, the unique properties of mechanical metamaterials are very much dependent on the arrangement of their fundamental building units to create a structure (Findeisen et al., 2017). The building units in mechanical metamaterials refer to the unit cells arranged in

a periodic pattern and range, in general, from the µm to the mm scale. In contrast, the structural level ranges from mm to the macroscale. By tuning the structural parameters of the mechanical metamaterial, such as the unit cell geometry, connectivity between them, size, and volume fraction of unit cells, the mechanical behavior of the metamaterial can be modified to present unique properties and achieve requirements that conventional monolithic materials cannot attain.

Mechanical metamaterials can be designed to have an optimum combination of properties, such as high stiffness, good impact response, and low weight. Also, mechanical metamaterials can be designed to achieve some specific non-conventional response such as very low or even negative compressibility, which is obtained by a tailored Poisson's ratio or some special non-linear behavior (Suard et al., 2015; Yu et al., 2018; Maconachie et al., 2019). Moreover, mechanic metamaterials can be designed to present different structural parameters, creating structures with mechanical properties that can change abruptly or gradually from one area to another.

The behavior of mechanical metamaterials is determined by the design of their unit cells, which can be categorized into five basic types: lattice, chiral/anti-chiral, hierarchical, origami, and pattern transformation-based metamaterials. An example of this classification is shown in Figure 1.2.

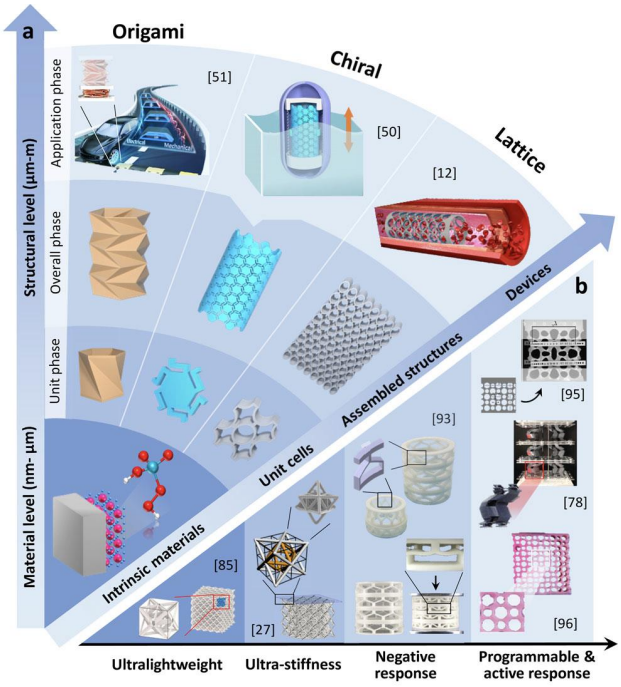

Figure 1.2: Principles, main categories, and properties of mechanical metamaterials. (a) Formation of mechanical metamaterials at the material to structural levels. Categories of mechanical metamaterials based on the microstructures and their typical applications. (b) Extraordinary mechanical characteristics of mechanical metamaterials (Jiao et al., 2023).

Lattice metamaterials

Lattice materials are artificial lattice structures composed of a periodically connected framework of struts or beams. In lattice metamaterials, the stiffness depends on lattice geometry and volume fraction (relative density). The stiffness and strength of lattice structures is optimized by designing the periodic arrangement of the struts/beams such that loads applied at the macroscale deform the unit cells at the microscopic scale in the most efficient manner. Depending on the target response of the metamaterial, the structural elements within the single unit cell can be assembled to perform predominantly in bending or uniaxially (Suard et al., 2015; Jiao et al., 2023;Yu et al., 2018). Furthermore, the engineered arrangement of the struts can tune the degree of anisotropy a lattice can have.

Due to the versatility of the arrangements the struts can have to form a unit cell, lattice materials can present a wide variety of mechanical properties and behaviors, as shown in Figure 1.3.

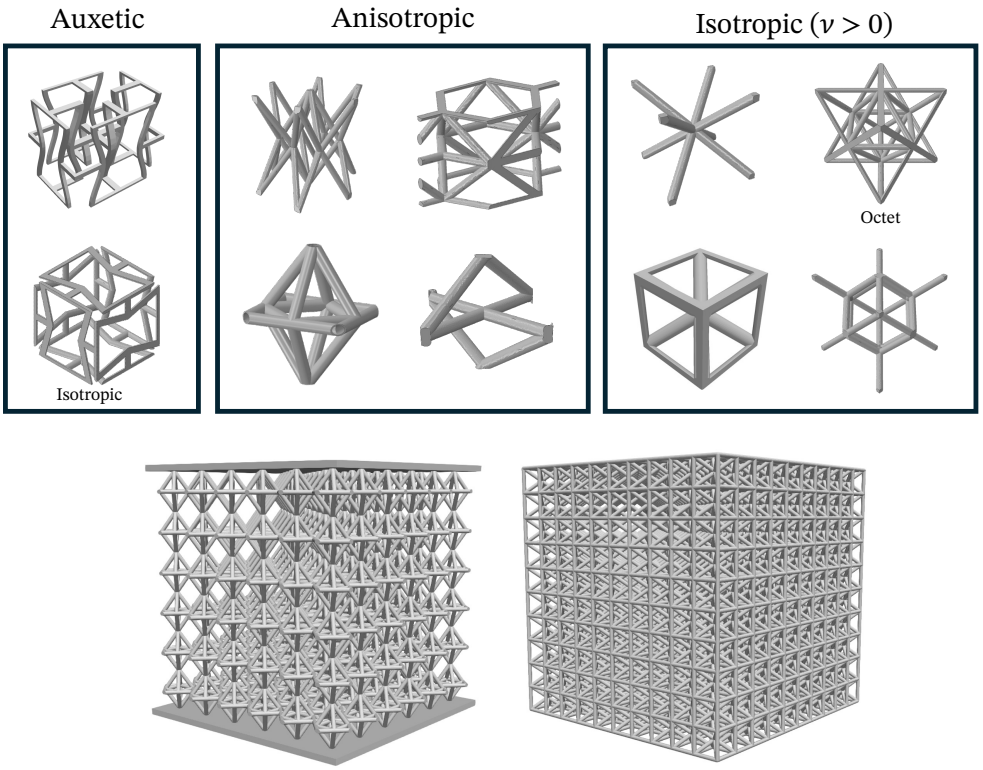

Figure 1.3: Some examples of unit cells where the struts arrangement gives them specific properties and behaviors.Two lattice examples at the bottom.

They can be designed to have a specific ratio between stiffness and weight, which can range from Young's modulus/ density ratios close to that of bulk metals Zheng et al., 2014 to very soft lattices. This property can be applied to multiple fields, such as in medicine for bone replacement implants, where lattice materials can reproduce the bone structural behavior with internal open space to let cells colonize the implant are essential requisites (Parthasarathy et al., 2011; Kohli et al., 2023). In addition, bones present anisotropic behaviors to optimize

load distribution inside the body, and the design of these types of lattice materials could fulfill the requirements needed (Bückmann et al., 2012; Yu et al., 2018).

Some unit cell configurations present remarkable energy absorption behavior for strain rates up to 1000 s^{-1}, such as the well-known octet truss geometry, which, in addition, presents isotropic elastic response, a linear relation between stiffness and volume fraction, and a constant Poisson's ratio independent of the volume fractions (Deshpande et al., 2001; Tancogne-Dejean et al., 2016; Yu et al., 2018). The behavior of this type of lattice materials for impact has been analyzed in multiple research (L. Smith et al., 2024). Lattices with good shock absorption behavior can be used in automotive and aircraft components, helmets, and shoe soles, among other sectors. Two examples of these applications are represented in Figure 1.4, where the prototypes shown have been designed within the project in which this thesis has been developed, MOAMMM.

(a) **(b)**

Figure 1.4: Shoesole and helmet prototypes made with lattice materials developed in the MOAMMM project.

On impact, lattices absorb energy as a combination of elastic stored energy, dissipation through viscous elastic/plastic phenomenon, dissipation through permanent plastic deformation, or dissipation through strut breakage. Alternatively, a reversible way to obtain a good energy absorption and damping response is by triggering an instability response. These instabilities can be achieved by tuning the bending properties of the beams or struts that form the unit cell (thickness, length, and width) such that the cell becomes a bi-stable metamaterial based on bucking elements. Bi-stable materials are designed to have an intended instability mode and stable equilibrium configurations, enabling reversible deformation to absorb impacts multiple times without losing their functionality (Findeisen et al., 2017). They can be applied, for example, in helmets for contact sports like rugby or crash safety systems in the automotive industry.

In addition, the structural units can be arranged to confer the structure an auxetic behavior, which is present in structures with negative Poisson ratios (Bückmann et al., 2012). When auxetic materials are subjected to compressive loads, their cross-section contracts, whereas under tensile loads, their cross-section expands (Rafsanjani and Pasini, 2016; Yu et al., 2018).

These materials present a good impact response as the lattice densifies under the area of the impact, which could be potentially used to reinforce projectiles to enhance their penetration or, on the contrary, on surfaces to stop the projectile from penetrating. In addition, auxetic structures can also be designed to present a bi-stable configuration to be used as stents on arteries as they can be inserted through a small cavity inside the body, preventing invasive surgery, and then stretched to the artery's diameter, opening up the blockage (Mir et al., 2014).

Due to the multiple material properties and behavior lattice materials can have to achieve specific properties, their research interest has been increasing since the last decade (Jiao et al., 2023). Figure 1.5 reflects this growth interest with only the increasing number of publications about lattice materials every year, especially since 2014.

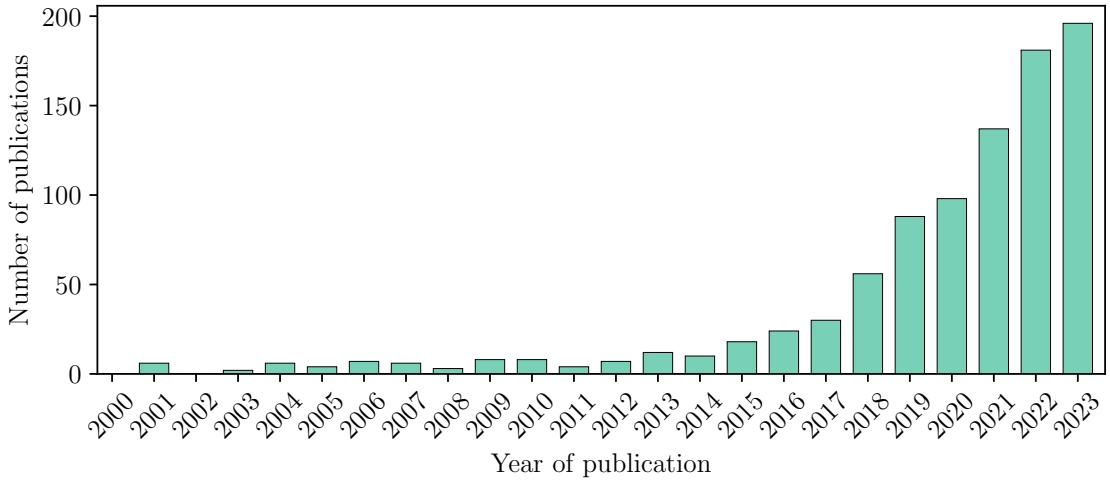

Figure 1.5: Graph showing the number of publications about lattice/truss materials, published yearly by Elsevier journals. Data obtained from ScienceDirect, 2024.

Chiral, anti-chiral and hierarchical metamaterials

Chiral and anti-chiral metamaterials are structures characterized by structural units with a configuration that cannot be superimposed onto their mirror image (Jiao et al., 2023). The unit cells generally comprise a central node with a cylindrical or polygonal geometry. The nodes are tangentially attached with ligaments that work under flexion when a load is applied, producing a rotation in the node. Chiral metamaterials are those where the unit cells are connected with nodes on the opposite side of the ligaments, and when the nodes are connected on the same side, they are anti-chiral (Mousanezhad et al., 2016; Yu et al., 2018; W. Wu et al., 2018). In hierarchical metamaterials, the cylindrical or polygonal geometry comprising the central node is attached to ligaments perpendicular to the node's surface, resulting in a structure composed of elements that are structured themselves. Some examples of the architecture of these materials are shown in Figure 1.6.

As lattice metamaterials, some hierarchical metamaterials present remarkable stiffness/low weight ratios and are characterized by an almost linear increase of in-plane stiffness with

density but a decrease in shear modulus. On the contrary, by sacrificing Young's modulus, they can be designed to present high shear moduli (Mousanezhad et al., 2016; Yu et al., 2018). These materials present in-plane stiffness 3.5 times higher than that of conventional hexagonal honeycomb. These tunable materials can be used in aircraft applications to control the structural performance of aircraft components such as wings or blades, vibration absorption, or non-pneumatic tires (Haghpanah et al., 2013).

Chiral, anti-chiral, and hierarchical metamaterials can present auxetic behavior with large deformations, where shear modulus decreases with the degree of chirality. In addition, they can be tuned to present isotropic or anisotropic behavior (Mousanezhad et al., 2016; Yu et al., 2018). The use of chiral and anti-chiral metamaterials for vibration attenuation is being studied for airfoil design applications. In addition, due to the large deformations, they can be applied for flexible substrates or morphing systems for flat-curved surfaces. Furthermore, they can also be applied for stents in medical applications (W. Wu et al., 2019).

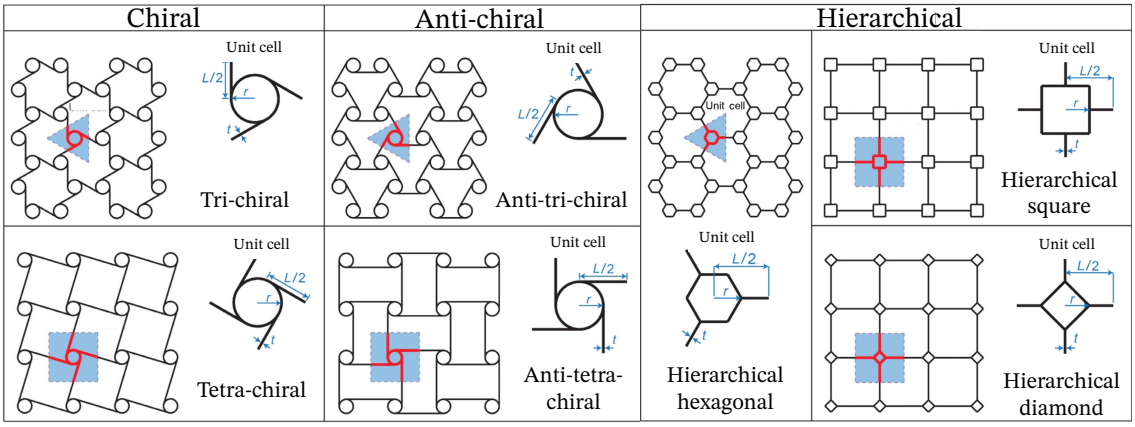

Figure 1.6: Schematic of the structure and the unit cell of relative density for the chiral, anti-chiral, and hierarchical honeycombs studied by Mousanezhad et al., 2016.

Origami inspired metamaterials

Origami metamaterials are structures presenting unit cells that consist of sheets folded in specific periodic patterns. 3D origami structures, called cellular origami metamaterials, are composed of interconnected origami layers stacked together(Yu et al., 2018; Jiao et al., 2023). The design of these materials is based on a plate-hinge compliant mechanism where the energetic landscape arises from torsional spring interactions rather than central-force linear springs (Yu et al., 2018). Origami materials present a clear advantage in deformation, as they deform by folding/unfolding the material along creases instead of deforming rigid faces (Lv et al., 2014).

Origami-based metamaterials present enhanced flexibility, deformability, and compactness due to their folding mechanisms. The folded patterns can be tuned to present a wide range of Poisson's ratios, from negative to positive values, even at the same time, as the case of the Miura-ori fold pattern, which presents auxetic behavior in-plane deformations and a positive Poisson's ratio for out-of-plane bending. They can show tunable stiffness and bi-stable behavior with different folding tesselations (Yu et al., 2018).

Due to these materials' enhanced deformability and compactness, they have multiple applications in robotics, energy absorption, medicine, automotive safety, such as airbags, or space exploration, for components such as foldable structures (Figure 1.7a), photovoltaic panels (Figure 1.7b), or telescope lenses (Lv et al., 2014; F. Liu et al., 2024).

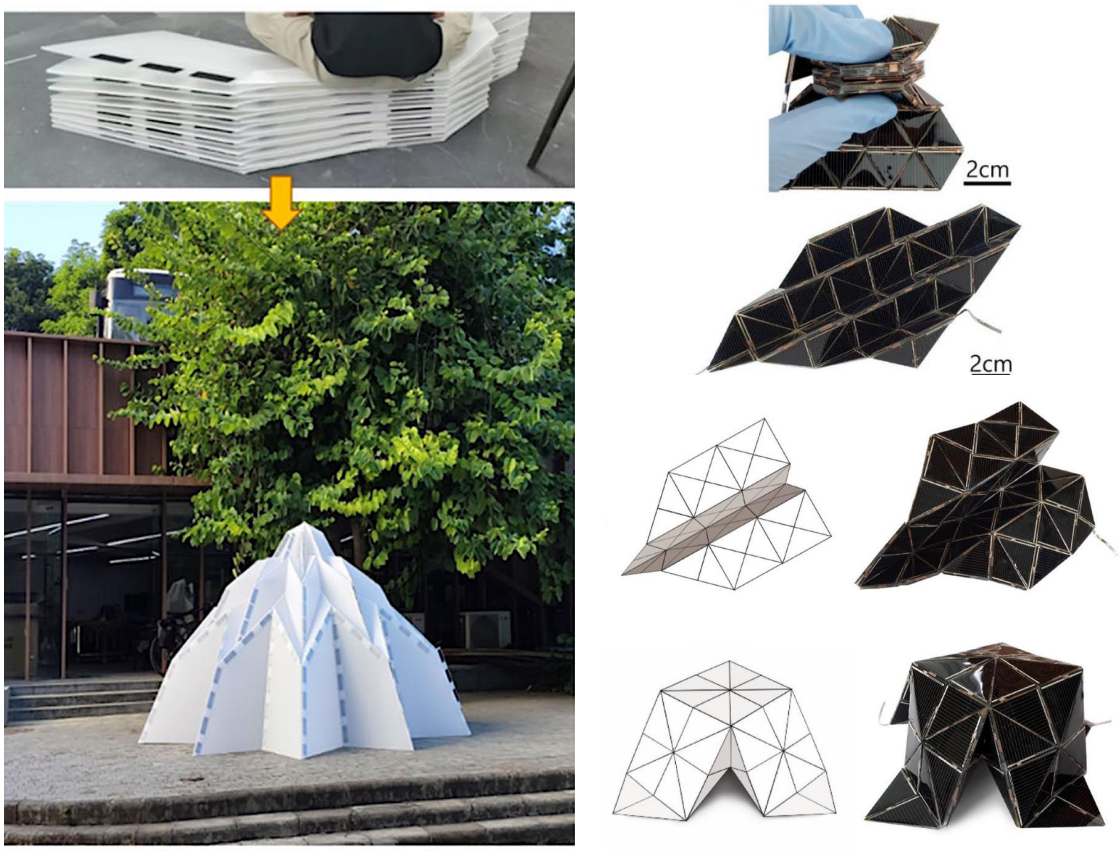

(a) **(b)**

Figure 1.7: Origami-inspired foldable structures (a) Miura origami-inspired canopy (Huang et al., 2023), and (b) tessellated Crystalline-Si solar cell module (Sim et al., 2021).

Pattern transformation metamaterials

Pattern transformation metamaterials are structures whose mechanical response is based on the different elastic buckling modes a particular array of building units presents (Yu et al., 2018). In general, building units are connected together through their vertices by hinges, as seen in Figure 1.8a. When an external force is applied, the hinges bend, inducing a rotation in the building units and producing a pattern transformation. Some patterns are designed to present bi-stability when snap-through instabilities occur. These materials are designed to present auxetic behavior, bi-stable behavior, and tunable stiffness (Yu et al., 2018).

A special case of pattern transformation metamaterials is the paper-cutting inspired frameworks called kirigami-based metamaterials, which can present auxetic and bi-stable behavior at the same time, which can be used, for example, for medical stents and resizeable screens (Rafsanjani and Pasini, 2016; Yu et al., 2018).

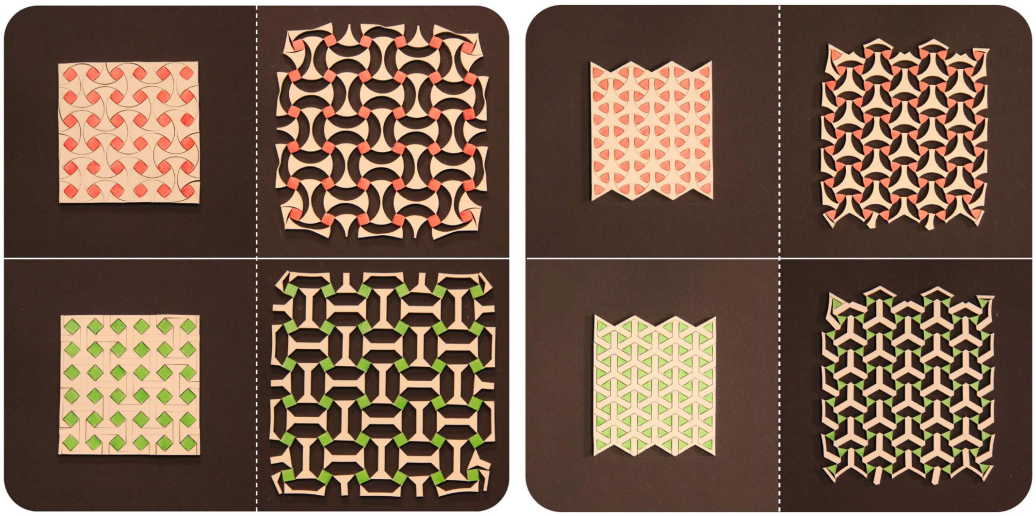

(a)

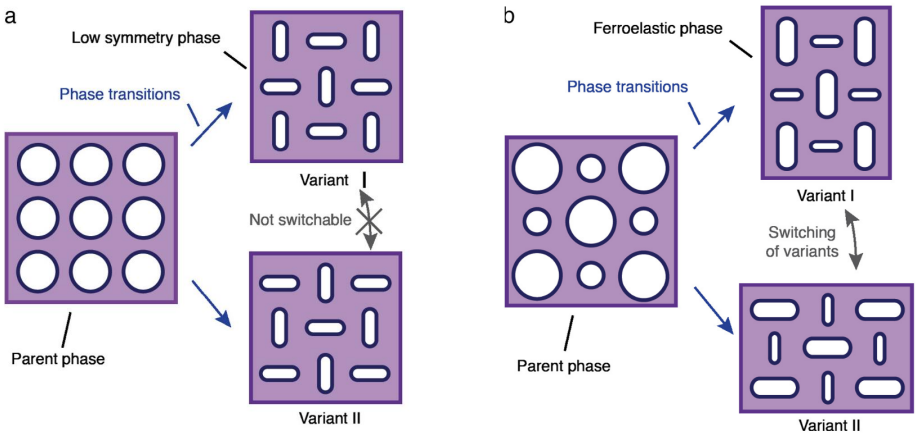

(b)

Figure 1.8: Examples of pattern transformation metamaterials. (a) Bi-stable auxetic metamaterials based on square and triangular cut motifs studied by Rafsanjani and Pasini, 2016, and (b) phase transforming pattern of elastomeric blocks used in the work by Yang et al., 2016.

One of the most well-known pattern transformation metamaterials, which does not rely on hinges but resembles rigid regions connected by beams, consists of a sheet or plate with an array of circular pores, see Figure 1.8b, with different shapes (circular, elliptical, irregular), sizes, and tessellation distribution (square, triangular, trihexagonal, and rombitrihexagonal tiling). Different shapes and sizes can be on the same sheet or plate, making possible the design of materials with the desired Poisson's ratio or stiffness (Yu et al., 2018). When an external force is applied, the pore shapes change to a periodic configuration of alternating elongated ellipses of high aspect ratios oriented in an orthogonal way. This instability is reversible, meaning the material recovers when the external load ceases (Yu et al., 2018; Bar-Sinai et al., 2020). These materials can be used for shock absorption applications.

1.2 Additive Manufacturing

Mechanical metamaterials present complex geometries, and their manufacturing process was difficult or not possible until the emergence of additive manufacturing techniques (AM), which make it possible to build lattice materials in an extended scale range, from millimetric to nanometric (Suard et al., 2015).

Additive manufacturing is a fabrication method that consists of depositing material layer by layer to obtain a three-dimensional piece or component. This method was originated in the 1980s as a quick prototyping method to produce prototype models for product development swiftly and easily. However, currently, it finds diverse applications beyond its initial purpose. It possesses the capability to fabricate intricate geometric pieces that are unattainable using traditional manufacturing methods (Tofail et al., 2018; Gibson et al., 2021; EPO, 2023). Its applications span various fields, including aerospace, automotive, energy, medical, consumer goods, construction, and personal hobbyist projects.

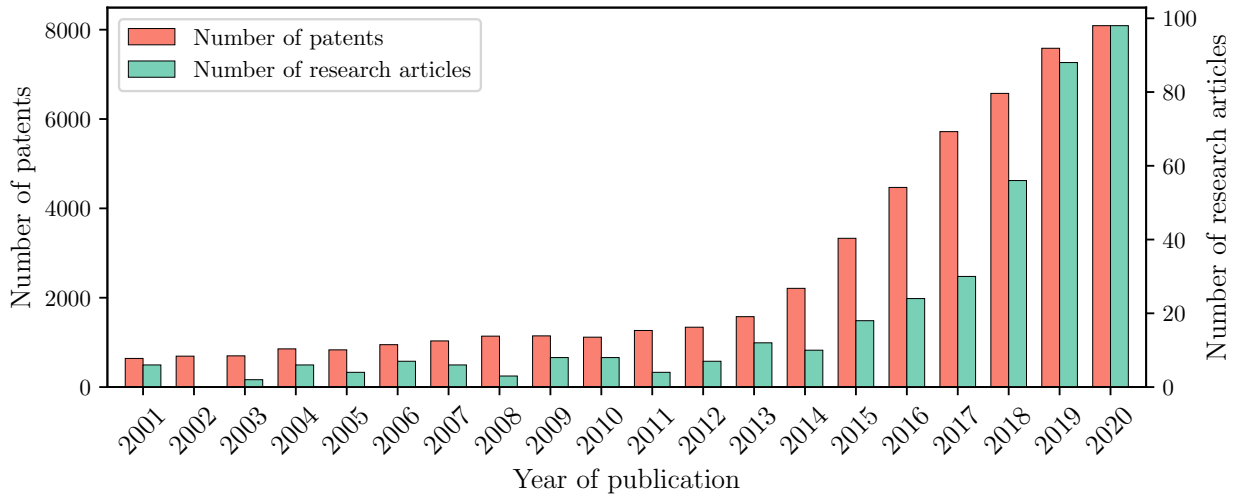

Figure 1.9: Graph showing the number of publications about lattice/truss materials by Elsevier journals and AM technologies patents published yearly. Data obtained from ScienceDirect, 2024 and EPO, 2023.

The growth of the additive manufacturing market is fast. The overall worldwide revenue growth in products and services has tripled its value in the last 6 years, and from 2021 to 2022, the growth rate reached 18.3 %, reaching 18 USD billion in 2022. It is estimated that the market for additive manufacturing will reach 120.19 USD billion by 2030 (Scott, 2023; NovaOne, 2023). Nevertheless, the additive manufacturing market is an active area of research and is developing rapidly; in fact, 30 % of the annual revenue is invested in research and development. The development of new additive manufacturing technologies is reflected in the number of patents filed annually. Since 2013, the compound annual growth rate of patent publications is over 26 %, where over 8000 patents related to AM were published (EPO, 2023). This growth reflects a direct correlation between the research interest and development of lattice/truss metamaterials, and the increase in the use of additive manufacturing for industrial

applications and new technologies. Figure 1.9 shows the number of research publications about lattice metamaterials and patents about AM technologies published yearly, where the correlation between both can be observed.

1.2.1 Processes and technologies

Additive manufacturing involves several steps to produce a component, starting from computer-aided design (CAD) to the 3D printing process (Tofail et al., 2018; Gibson et al., 2021).

First, the model's 3D geometry is created using a CAD program or X-ray tomography. Following this, the model is transformed into .stl format, describing the outside surfaces of the 3D model. Subsequently, it undergoes conversion into a format that calculates slices and guides the additive manufacturing machine on the x, y, and z axes to deposit material accurately. Moreover, adjustments can be made to the dimensions and orientation of the 3D model to optimize material usage and improve finish quality (Tofail et al., 2018; Gibson et al., 2021).

In order to print the part, parameters for the machine must be configured, such as layer thickness, speed, or energy source power. Once these parameters are established, component manufacturing begins. Afterward, the finished part is removed from the machine and subjected to post-processing to eliminate supports and meet finishing requirements (Tofail et al., 2018; Gibson et al., 2021).

In comparison to other manufacturing techniques, additive manufacturing allows the fabrication of parts with complex geometries, including intricate internal features or flexible and light hollow structures like lattice metamaterials. In addition, the digital design is converted directly into a physical component without significant alterations, which allows to manufacture directly a component in its final shape with no additional processing. This implies a reduction in product development time, a faster transfer to market and maximizes the material utilization, leading to a zero or low material waste manufacturing process. In addition, additive manufacturing generates customized or on-demand components with no additional tooling or manufacturing costs, moving away from manufacturing based on mass production (Tofail et al., 2018).

A wide range of materials, including metallic, ceramic, polymers, and even biomaterials, can be used for producing components of a wide range of dimensions with additive manufacturing. Different AM processes are required depending on the material and dimensions of the component. According to ASTM 52900:2015 AM processes are classified into seven groups (Tofail et al., 2018): Binder jetting, material jetting, material extrusion, directed energy deposition, sheet lamination, vat photopolymerization, and powder bed fusion.

Binder jetting (BJ) and Material jetting (MJ)

The materials employed for this purpose may include polymers, ceramics, metals, biomaterials, and solutions or dispersions applied in liquid form. These are deposited as droplets onto a surface, subsequently undergoing bonding processes. In the case of MJ (Material Jetting), the material is deposited as a blend with the binder (Figure 1.10b), whereas in BJ (Binder

Jetting), the binder is sprayed onto a powder bed through a nozzle (Figure 1.10a), acting as a binding agent. MJ processes produce small and high-resolution products that require support material, whereas BJ processes allow the building of large volumes with limited mechanical properties at a relatively low cost (Tofail et al., 2018; Gibson et al., 2021).

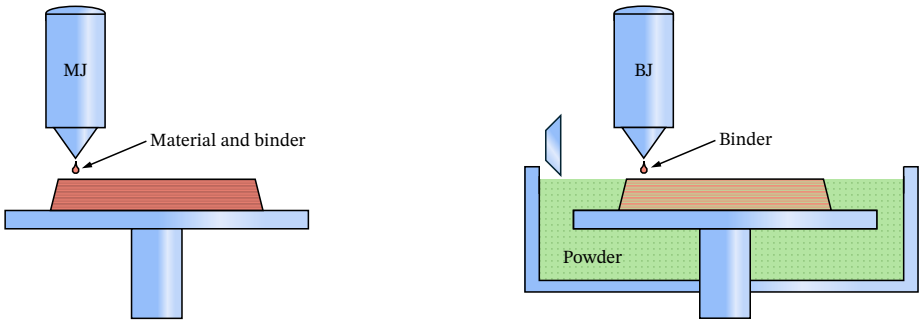

(a) **(b)**

Figure 1.10: Schematic figures showing (a) material jetting and (b) binder jetting manufacturing processes. Own elaboration.

Material extrusion (ME)

Material extrusion technologies, such as fused deposition modeling (FDM) or fused layer modeling (FLM), use polymers and composite filaments as feeding material that is selectively pushed out through the nozzle and deposited layer by layer with the desired cross-section to create components, as shown in Figure 1.11a. These technologies are one of the most economical and widespread used. The main disadvantage of these technologies is that the finished component presents a strong layered texture that leads to structural anisotropy and is not suitable for getting fine details (Tofail et al., 2018; Gibson et al., 2021).

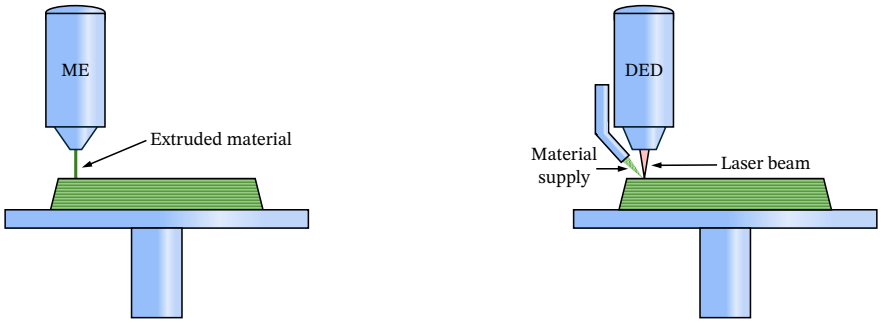

(a) **(b)**

Figure 1.11: Schematic figures showing (a) material extrusion and (b) directed energy deposition processes. Own elaboration.

Directed energy deposition (DED)

Directed energy deposition involves adding material in a molten state using an energy beam, such as an electric arc, plasma, focused electron beam, or laser beam emitted from a deposition head, to fabricate components. The deposition head also contains the nozzle, which is the part responsible for feeding the material. Figure 1.11b shows a representation of this process. The material generally used is metal in the form of powders or wires, but ceramics and polymer hybrids can also be used. It is used in the industry to make large and high-quality dimension components at fast manufacturing velocities without the need for a flat surface to start the deposition process. This makes this technology excellent for repair applications. The medium-low precision of this technology makes it not suitable for small components. In addition, the quality of the finishing surface is low (Tofail et al., 2018; Gibson et al., 2021).

Sheet lamination (SL)

Sheet lamination, represented in Figure 1.12a, is a process that consists of cutting material sheets of polymer, metal, ceramic, or hybrid material with a laser that deposits one entire layer in a single step. The layer is pressed and stacked to the other layers of the component by adhesive, thermal bonding, clamping, or ultrasonic welding. Components using this technology are manufactured ar high speeds and low cost. However, its dimensions are limited to a small size and require post-processing (Tofail et al., 2018; Gibson et al., 2021).

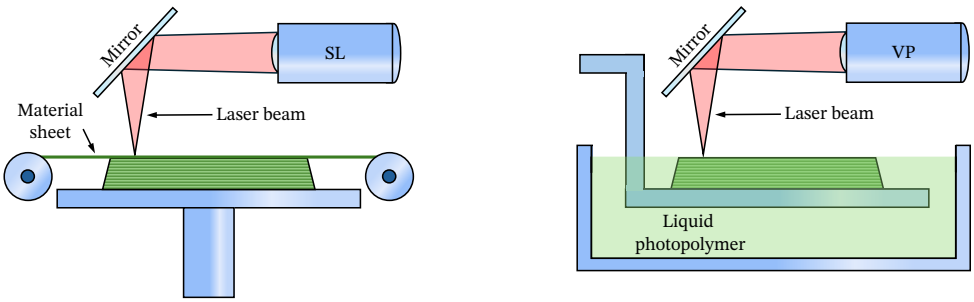

(a) **(b)**

Figure 1.12: Schematic figures showing (a) sheet lamination and (b) vat photopolymerization processes. Own elaboration.

Vat photopolymerization (VP)

A light source locally cures a liquid photopolymer in a vat with high precision, creating medium to small-sized components with excellent surface finish and details. Figure 1.12b shows a representation of this process. The counterpart of this technique is that components created with this process tend to have low useful life and poor mechanical properties, although material research and development is improving rapidly. In addition, raw materials are expensive. After the component is built, it needs to be extra-cured with UV light. In the case of lattice materials, this presents an additional problem since the light might not reach

the deepest structural units and not be cured properly. Stereolithography (SLA) was the first technology developed with this process and widely used on the commonly named resin 3D printers. (Tofail et al., 2018; Gibson et al., 2021).

Powder bed fusion (PBF)

This process is based on thermal energy that melts a local region of the powder bed of the build material by a laser or electron beam as the source power. The powder is remelted again to fuse the adjacent powder together, layer by layer, by applying powder that covers the surface of the last layer (Figure 1.13). The thin layer thickness ($\approx$ 0.1 mm) and laser spot size (0.2-1 mm) that can be achieved with PBF make it suitable for building components with high resolution for fine details and good macroscopic surface finish, which is essential for lattice metamaterials and other components for industrial applications. There is a wide variety of polymer, metal, polymers, composites, and hybrid powder materials available, making this technology one of the most versatile for creating components for different applications, which is leading to an increased interest in industry and investment. Technologies based on PBF processes are electron beam melting (EBM), which is used for conductive materials; selective laser melting (SLM), which is used for metals and ceramics; and selective laser sintering (SLS), which is used for thermoplastic polymers. These technologies present the highest number of tool manufacturers across Europe, the USA, and Japan (Tofail et al., 2018; Gibson et al., 2021).

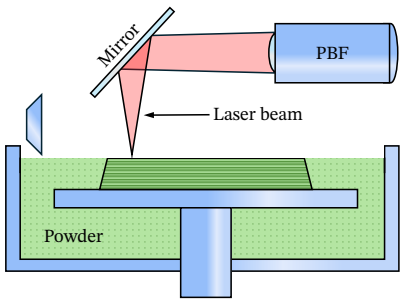

Figure 1.13: Scheme of the powder bed fusion process. Own elaboration.

1.2.2 Challenges and limitations

Despite additive manufacturing is potentially the best technique for creating components with complex geometries, AM technologies are still young and nowadays present some limitations. Their success relies on other factors that conventional manufacturing processes have been maturing over the last couple of centuries.

Large-volume production is not yet optimized for additive manufacturing processes as the productivity rates of the machines are relatively low, and raw materials are still more expensive in comparison to conventional manufacturing raw materials and processes, which increases

production costs for AM components (Tofail et al., 2018; Flores et al., 2020; Al Rashid et al., 2021).

As mentioned previously, every additive manufacturing process builds 3D components layer by layer, which means that AM uses a 2D building tessellation strategy on the building direction limited by the machine resolution, which leads to differences between the virtual and built volume (Tofail et al., 2018). This difference may result in discontinuities, dimensional inaccuracy, poor surface finish, internal defects such as porosity or trapped material, and structural or mechanical anisotropies. These defects can lead to modifications of the structural integrity and mechanical performance of the designed component, such as a variation in the local density or modifications in the local stress distribution acting as crack initiators. In addition, the complex thermal history can produce complex microstructures on the component and feed material, leading to undesired mechanical behavior on the component and degrading the feed material in some AM processes (Suard et al., 2015; Amani et al., 2018; Tofail et al., 2018).

In the end, the success of additive manufacturing processes depends on the product's final quality and how well it can perform its function. To achieve success in the market, it is necessary to guarantee that AM components meet the characteristics established by the design. However, due to the lack of standards and norms, which are abundant for conventional manufacturing techniques, it is difficult to assess the quality of the final printed product. There are no appropriate measurement strategies to confirm that the component will present the properties to perform the desired function. It is then essential to develop strategies to overcome the defects formed during the AM process, but most importantly, the techniques to characterize those defects: surface roughness, defects at the microscopic level, porosity, etc. (Tofail et al., 2018).

1.3 Estimation of the mechanical response of lattice materials by numerical simulation

Experimental campaigns to determine the mechanical response of new lattice geometry or studying the impact of some process parameters in the actual lattice performance is a very expensive and inefficient way to design and optimize the response of a lattice metamaterial. A cheaper and faster alternative way to optimize the manufacturing process and assess the AM product's mechanical performance is to combine testing with computational modeling. Computer simulation tools allow to numerically evaluate the processing parameters, geometry, or mechanical properties to assess the quality of the final product by numerical simulations implementing a specific material model.

Focusing on the mechanical response of the meta-material, an ideal infinitely periodic array of lattice unit cells, full-field homogenization is the most reliable approach. This method consists of obtaining the overall mechanical response of the lattice material at the macroscopic level as well as the microscopic fields with high precision by numerically solving a boundary value problem on a representative volume element (RVE), which consists of a cell of the lattice. Full-field homogenization can be used to predict the performance of a perfect lattice designed

by CAD but also allows the evaluation of the influence of the fabrication defects on the mechanical behavior of AM components if these defects are explicitly included in the RVE.

Two numerical methods are frequently used to solve computational homogenization problems, Finite Element Method and Fast Fourier Transform based methods, which have been applied to lattice materials in several studies.

Finite element method (FEM)

The most common full-field homogenization approach used in numerical analysis is the Finite Element Method (FEM). This method consists of solving the weak form of a partial differential equation where the spatial domain —here the representative volume element— is discretized in a mesh that can conformably adapt to the actual shape of the lattice. FEM has several advantages being, the most remarkable one its ability to represent the geometry of any domain very accurately by using automatic algorithms for meshing with tetrahedral elements. FEM has been profusely used to obtain the response of lattice metamaterials, enabling detailed analysis of their mechanical behavior (Geng et al., 2018). Researchers have employed FEM to study stress distribution, deformation modes (Wang et al., 2023), instabilities (Bertoldi, 2017), and the impact of geometric parameters on the overall performance of lattice structures (Feng et al., 2021). It has also been widely used to predict failure mechanisms (Amani et al., 2018, Shaikeea et al., 2024), optimize lattice designs for specific applications (Ćurković, 2021), and assess the influence of defects on mechanical properties (Amani et al., 2018, 2020; Sombatmai et al., 2021; Vanderesse et al., 2011). These simulations often complement experimental studies, providing valuable insights into the behavior of lattices under various loading conditions. The limitation of FE in the case of lattice materials is that very small elements have to be used to accurately represent the geometry of the bars. This fineness can lead to very large models, which can result in computationally expensive, especially when combined with periodic boundary conditions. In addition, including explicitly the defects within the bars becomes challenging both for the difficulties in meshing and also for the size of the resulting models (Lucarini, Cobian, et al., 2021).

Fast Fourier transform (FFT)

The Fast Fourier Transform (FFT) based homogenization method is a simulation framework designed specifically to compute the mechanical response of periodic heterogeneous materials as lattice materials. The periodic boundary value problem is solved by transformation to Fourier space which can be performed efficiently with the use of the FFT algorithm. The method requires a regular mesh so the cubic RVE is divided into voxels, each assigned specific mechanical properties. FFT solvers have been successfully applied to any type of heterogeneous materials, including metals, composites, foams, etc. A deep review of the use of FFT methods in micromechanical problems can be found in Lucarini, Upadhyay, and Segurado, 2021. However, in the case of lattice materials, the method presents some challenges in dealing with the infinite contrast of stiffness between the material of the lattice and the empty space, which should be included in the RVE. On the other hand, the very higher efficiency in periodic problems with respect FEM solvers allows to use very fine grids

and considers, without the need of any complex meshing, explicitly the defects. The first adaptation of FFT solvers for lattice materials was recently proposed in Lucarini et al., 2022 and has been used in this work.

1.4 Motivation

A very large number of studies can be found that relate the lattice structure with mechanical response for any kind of material and AM manufacturing technique. However, the number of studies that analyze in detail the behavior of lattice materials with defects and how the printing quality is affected by the strut size is scarce. Many studies found in the literature show a reduction in the stiffness of small-diameter struts compared to the response of bulk specimens. In addition, in these studies, the numerical simulations based on FE and representative volumes based on strut's tomographies overestimate the stiffness of the struts compared to the experimental values (D. Bruson and Iuliano, 2023; Hossain et al., 2021; Sombatmai et al., 2021; Suard et al., 2015; M. Wu et al., 2024). The potential origin of this reduction includes porosity and other geometrical features that affect the effective cross-section along the struts, as well as changes in the microstructure of the printed material due to the different thermal histories depending on the printed geometry.

To be able to design components based on lattice materials manufactured by 3D printing, it is essential to understand the reasons behind the difference in the behavior between bulk specimens and strut-sized parts.

Most of the experimental analyses of this size-dependent response are performed for 3D printed metallic materials, but the origin of these effects in metals (e.g., grain sizes and orientations changes due to the different thermal histories depending on the part dimensions) cannot be extrapolated to polymer-based materials fabricated by laser sintering. In particular, there are very few works that study the mechanical behavior of additive-manufactured PA12 struts in detail, analyzing the size effect. Some studies can be found, such as the work by Zhu and Majewski, 2020, which studies the effect of the energy input on the pore formation and melting degree between particles, but a full assessment linking these effects with the part size is still missing.

Numerical simulations, which include the actual material defects and roughness, are fundamental to complement the experimental studies and to help in designing the lattice with the desired properties. Although Finite Element Method (FEM) is the most common full-field homogenization approach, it presents difficulties in including the defects measured experimentally (by X-Ray tomography, for example) since the meshing of these geometries results in a very large number of degrees of freedom. This leads to very resource demanding computations (Suard et al., 2015; Amani et al., 2018; Lhuissier et al., 2016). Considering this difficulty, another option to do numerical simulations that do not require a mesh are methods based on the Fast Fourier Transform algorithm (FFT). With this technique, 3D printed unit cells with all the internal features reconstructed from the tomographic images can be directly simulated and, in parallel, characterize the same 3D printed cells with tests. This will allow integrated numerical and experimental studies of additively manufactured materials. Nevertheless, due to several numerical difficulties, only a few examples of the use of this technique for AM

materials exist, making the scope of these studies very limited.

1.5 Objectives and approach

This thesis work is endorsed in the European project MOAMMM -*Multi-scale Optimisation for Additive Manufacturing of fatigue resistant shock-absorbing MetaMaterials*. This project is focused on the development of a data-driven process to predict the microscale properties and mechanical response of additive-manufactured metamaterials to design optimized shock absorption devices. One key point to reach that end is an in-depth analysis of the mechanical behavior of PA12 lattice materials, which was the author's main task within this project and is the main purpose of this thesis.

The objective of this thesis is to analyze the non-linear behavior of PA12 lattice materials at different scales through experimental testing and full-field simulations, including the potential size and defect effects.

From the experimental point of view, the material's mechanical properties were measured on different scales by uniaxial tensile and compression tests on PA12 (Polyamide 12) at different strain rates, temperatures, and aging times on the macroscale, where the bulk samples were used, and the microscale by testing: single struts, unit cells, and lattice samples with a BCC geometry and different strut diameters and cell dimensions. The properties of the macroscopic and microscopic scales were then compared to analyze how the printing quality affects their mechanical properties. Sample morphology and defects were characterized using X-ray tomography and SEM imaging. Nano-indentation maps were also performed to obtain the Young's modulus distribution over the sample surface. The nanostructure, crystallinity, and annealing degree among the different samples were studied with differential scanning calorimetry (DSC) and small and wide-angle X-ray scattering (SAXS and WAXS). Experimental characterization also included in-situ tensile and compressive tests performed on individual struts and unit cells to assess the fracture behavior at different scales.

Numerically, the PA12 experimental data obtained from the characterization was used to calibrate the constitutive material models that predict their behavior for the simulations. The numerical analysis of the effect of defects was performed using the tomographies as RVEs and an FFT solver specifically adapted for the homogenization of struts and lattice materials (Lucarini et al., 2022). For fracture analysis, a phase-field fracture model implemented in FFT was used. A non-linear response prediction was conducted using FFT with a calibrated viscoelastic-viscoplastic material model tailored to represent both bulk and strut scales. These simulations allowed us to quantify the relative effect of the defects on the property changes and establish, together with the experiments, if these defects are solely responsible for the size effects found or if the material condition for the different thermal histories also plays a role.

Chapter 2

Materials and experimental methods

The aim of this chapter is to describe the main characteristics and properties of Polyamide12 material, sample fabrication, and the experimental tools and techniques used for the mechanical and microstructural characterization of additively manufactured PA12 samples and lattices at all scales. The mechanical behavior was analyzed by monotonic tensile, compression, hysteresis, relaxation, and shear tests at different strain rates. Dynamic mechanical analysis (DMA) was used to obtain the dynamic response under oscillating loading. Nanoindentation, both static and dynamic, was used to study the local mechanical properties in specific areas of the material.

Additionally, nanoindentation maps were created to observe the distribution of properties in different regions and relate the properties with the microstructure. To complement the microstructure analysis, X-ray tomography was used to observe and analyze the internal and surface defects in the samples, providing insight into their structural integrity.

Finally, differential scanning calorimetry (DSC) and X-ray scattering were used to study the crystallinity degree as well as the structure at the micro- and nano-scale levels, such as the nature of the different crystalline phases present and the organization of the polymeric chains in the material.

2.1 Polyamide 12 (PA12)

Polyamides (PA) are linear thermoplastic polymers obtained by the polycondensation of two monomers, a dicarboxylic acid with a -COOH group and a carbon chain with one amino group -NH_2. During polycondensation, the two monomers are involved in a chemical reaction that occurs in several stages, involving the loss of a water molecule for the formation of the polyamide polymer, as shown in Figure 2.1. The carboxylic group of the acid monomer reacts with the amino group, linking both monomers by a secondary amide group (-COHN-) and releasing water (Domininghaus, 1993). A standard polyamide is then a series of linear chains of $n-1$ methylene groups joined together by an amide group at the n^{th} position. In the case of PA12, the amide group is at the 12^{th} position linking chains of 11 methylene groups, as shown in Figure 2.2.

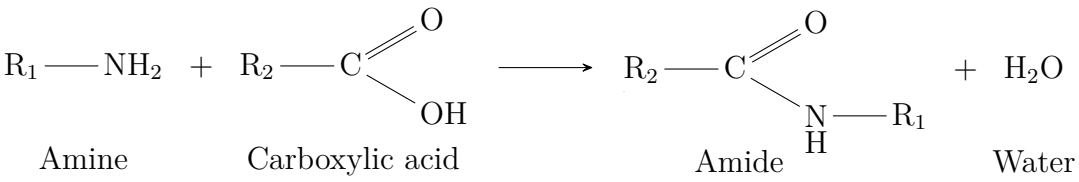

Figure 2.1: Condensation reaction between an amine and a carboxylic acid.

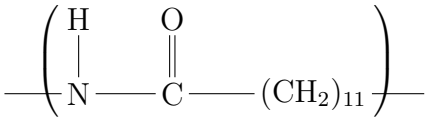

Figure 2.2: PA12 chemical formula

In general, polyamides are characterized by the following properties: (Domininghaus, 1993):

- high strength, stiffness, and hardness
- high heat distortion temperature
- high wear resistance
- good damping capacity
- non-toxicity
- good procesability

Table 2.1: General properties of PA12 and range of values for the properties of the most common polyamides: PA6, PA66, PA610, PA11, and PA12 (Domininghaus, 1993). The properties, from top to bottom, are water absorption (H_2O absorption), yield stress (σ_y), elongation at break (A%), elastic modulus (E, melting point (T_m), and glass transition temperature (T_g).

	PA12	**Other PA**
H_2O absorption [%]	0.7 - 1.1	0.2 - 3.5
σ_y **[MPa]**	45	40 - 65
A%]	300	150 - 500
E [MPa]	1600	1000 - 2000
T_m **[°C]**	175	175 - 255
T_g **[°C]**	49	49 - 60

Table 2.1 shows the general properties of PA12 and the range of values in which the properties of the most common polyamides are found: PA6, PA66, PA610, PA11, and PA12. The material properties of polyamides are mainly determined by the amount of -$CONH_2$ groups as they link the monomers within the polymer chain and other components from other chains or external to the chains. The frequency of the amide group in a polyamide chain affects the intermolecular forces, as hydrogen bonds are formed between the amide groups of different chains, the NH- from one chain to the O- from other chains. For this reason, PA6 presents

higher cohesive forces than PA12 and manifests a higher stiffness and melting point. However, high cohesive forces present a significant drawback, as water absorption increases as the amide group content increases (Domininghaus, 1993). Water and humidity condition the mechanical behavior of Polyamides, resulting detrimental to their mechanical properties, as a small percentage of water intake (0.6 % in PA12) results in swelling, deterioration of tensile and fracture properties, and an increase in toughness and ductility, know as the plasticization effect of water (Paolucci et al., 2020; Seltzer et al., 2011; Touris et al., 2020). In addition, due to the intermolecular forces created by hydrogen bonds, PA6 presents one of the highest melting points among polyamides, whereas PA12 presents the lowest melting point, as shown in Table 2.1.

Due to its polymorphic behavior, PA12 can present two main crystal structures, α and γ, depending on the hydrogen bonds formed between the chains and processing conditions. The α phase is formed under specific pressure and temperature conditions (Chen et al., 2018; Hejmady et al., 2022; Ma et al., 2020).

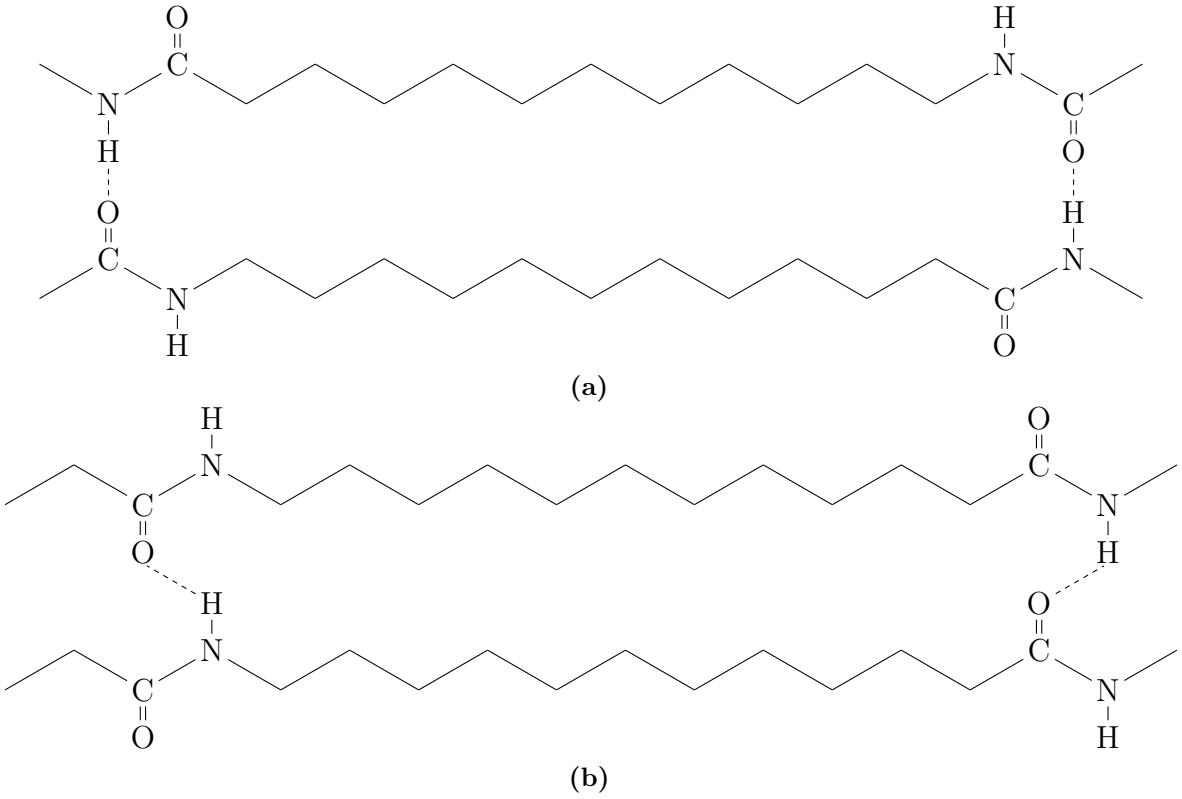

Figure 2.3: Polyamide 12 (a) α and (b) γ crystal forms. The dashed lines represent hydrogen bonds between the amide groups.

The α phase is a monoclinic structure that presents chains aligned antiparallel where the hydrogen bonds can be formed without the rotation of the amide groups, as depicted in Figure 2.3a. This α phase is formed under specific conditions, such as cooling under high pressure. Components obtained by injection molding or cold drawing present the α crystal structure. It can be detected with analysis techniques such as DSC (see section 2.8) or WAXS (in section

2.9), where it is detected by the presence of two melting peaks at around 168 and 175 ℃ in the case of DSC or two distinct reflection peaks at $2\theta \approx 20°$ and $\approx 24°$ in the case of WAXS (Chen et al., 2018; Hejmady et al., 2022; Ma et al., 2020).

In contrast, the γ phase is a hexagonal structure that presents parallel aligned chains, where the amide plane is twisted 60° out of the methylene groups (-CH_2) plane to form hydrogen bonds between the amide groups, as shown in Figure 2.3b. The γ phase is formed under slow cooling or annealing between 90 and 130 ℃, and it is the most stable phase of PA12. However, if the material is quenched under its T_g, the mesomorphic γ' structure is formed. The γ phase can be detected by the presence of a single melting peak at 175 ℃ or a reflection peak at $2\theta \approx 22.7°$ from the DSC or WAXS analysis, respectively (Chen et al., 2018; Hejmady et al., 2022; Ma et al., 2020).

Typical applications of Polyamide 12 include injection molding components, such as bearings, components for underwater use, insulation or parts for pumps, as well as extrusion products such as insulating films, cable sheathing, or tubes, for example (Domininghaus, 1993). In addition, Polyamide 12 holds the top position in the market among all polymers. In fact, almost 90 % of the components currently fabricated by SLS are made with polyamide (Wudy and Drummer, 2019).

2.2 Sample preparation

2.2.1 Sample fabrication: Selective Laser Sintering (SLS)

All 3D printed PA12 samples were fabricated using *EOS PA2200* powder on the commercial SLS machine *EOS FORMIGA P100* at *cirp*, Heimsheim, Germany. The machine is equipped with a 0.4 mm diameter laser, which determines the minimum resolution of the machine and follows a contour and hatching strategy to print all the samples. In this strategy, the laser beam first exposes the contour of the piece's corresponding cross-section after the powder layer is deposited. Then, the laser beam moves within the contour to hatch the internal surface of the cross-section. In addition, printing parameters used for this manufacturing strategy were maintained constant for all types of samples as the printing parameters employed for commercial *EOS PA2200* powder material were internally locked due to intellectual property. In addition, the powder used for printing was an equal (50/50) mix of virgin (new powder) and remaining powder that had been used in a previous 3D printing process (old powder). Details about the general properties of *EOS PA2200* found in its datasheet and the characterization of the powder morphology can be found in Annex 1.

2.2.2 Sample characteristics and details

The additive-manufactured samples conformed to two main sets of samples. The first set corresponded to standard tensile, compression, shear, and dynamic mechanical analysis specimens printed in different directions that were used to characterize Polyamide 12 at the macroscopic level. Figure 2.4 shows the different types of macroscopic samples used.

The second set of samples was composed of individual struts, unit cells, and lattices of different

sizes, as shown in Figure 2.5. Single struts were printed in three different directions, with layers perpendicular (H), vertical (V), and at 45 degrees with respect to the direction of the applied load (Figure 2.5a). Due to the small strut dimensions, the samples were printed in sprues of struts of the same diameter and printing direction to facilitate manipulation and avoid shipping damage from the manufacturer to the laboratory. For each diameter and dimension, two sprues containing 14 samples each were printed.

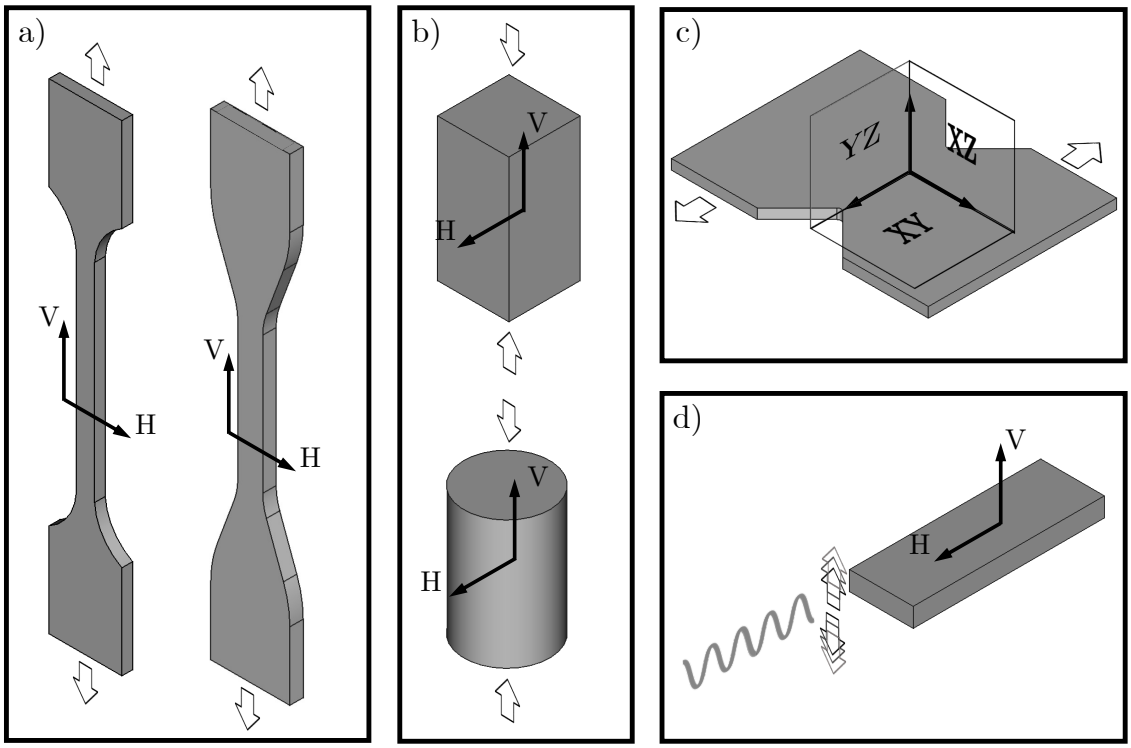

Figure 2.4: First set of samples. Specimen geometries corresponding to (a) tensile specimens for tests at room temperature (left) and 45ºC (right),(b) compression samples for different strain rates, (c) shear specimens, and (d) samples for dynamic mechanic analysis. Black arrows and the planes formed by these arrows in (c) correspond to layer directions.

The specimens of each geometry were printed in the same batch to reduce variability in the results between sets. After printing, all the samples underwent a de-powdering process and were sandblasted to remove excess powder. Specifically, the lattices contained loose powder entrapped inside, and it was necessary to manually remove the excess powder from inside the lattices after the sandblasting process and before mechanical testing, especially on the lattices with 0.5 mm diameter struts. In addition, some unit cells were vapor-smoothened in a vacuum at 100 ℃ with phenol to reduce surface roughness.

2.3 Equipment used for uniaxial tensile and compression tests

To conduct a detailed study of mechanical properties for various experimental conditions, several machines were used to cover the widest possible range of testing conditions.

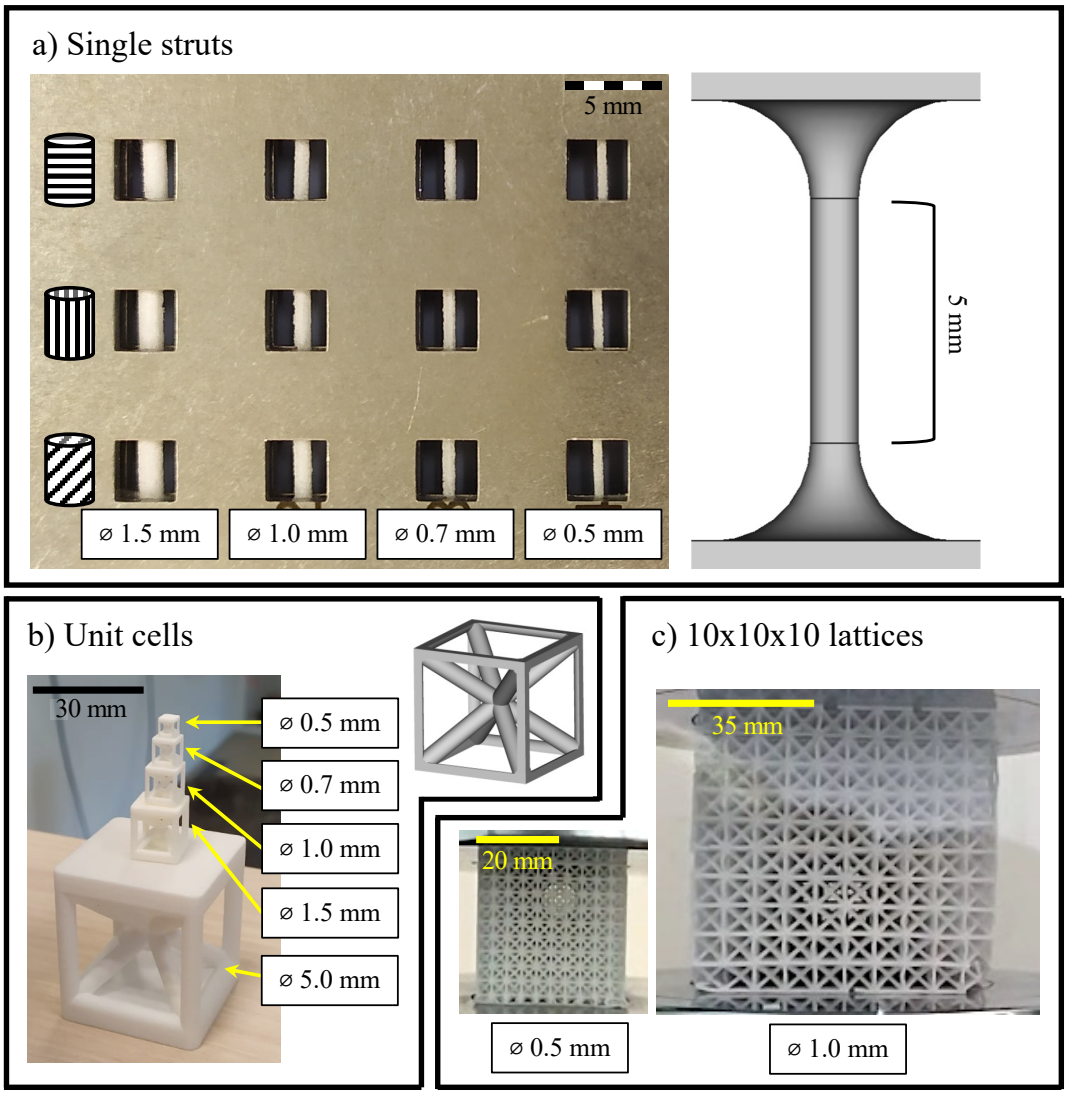

Figure 2.5: Second set of samples. Specimen geometries corresponding to (a) single strut specimens with different orientations and diameters placed on a sample holder for SAXS/WAXS measurements, (b) unit cell geometries, and (c) 10x10x10 lattices composed of different strut diameters for compression testing.

2.3.1 Universal Testing Machine

The universal testing machine is used for mechanical tests, typically tensile and compression tests. This machine is equipped with a movable crosshead that applies compressive or tensile loads to the sample. In addition, the load applied to the sample is directly measured by a load cell, and displacement is usually measured using an extensometer. In the case of polymeric materials, which can experience large deformations, such as PA12, using an extensometer is not always possible, and displacement can only be measured by the machine's moving cross-head.

2.3.2 Gleeble

The *Gleeble 3800 GTC* is a machine used to perform physical simulations where the samples can be subjected to various conditions by controlling temperatures, heating/cooling rates, displacements, and loads, which can also be combined. This allows the reproduction of the thermal and mechanical conditions that materials are subjected to during actual fabrication and application processes.

2.3.3 Hopkinson Split Pressure Bar

In order to analyze the elastoplastic behavior of a specimen at high strain rates, the Hopkinson Split Pressure Bar (HSPB) test is performed. It also allows us to study the effect of thermal softening and strain rate sensitivity. The test is based on the principle of one-dimensional wave propagation. The set-up consists of two Inconel bars, incident and transmission bars, and a striker (Figure 2.6) where the sample is placed between the bars. The incident bar is loose, enabling longitudinal displacements, whereas the transmission bar is fixed. Consequently, when the striker is ejected, and the incident bar is hit, a compressive wave travels through the incident bar to the end of this bar, where it splits into the reflected wave, which travels backward through the incident bar, and the transmission wave, transmitted to the transmission bar through the specimen. The bars remain in the elastic regime, whereas the specimen can suffer plastic deformation. A gas gun ejected the striker. In addition, two strain gauges are attached, transversally and longitudinally, in the middle of both bars to measure the incident, as well as reflected waves on the incident bar and transmitted waves on the transmission bar to make measurements. The strain gauges are in a Wheatstone bridge and connected to a computer through an oscilloscope's channels, which record voltage variations through time as waves travel through the bars (Siviour and Jordan, 2016). To reduce the ringing and shaping of the pulse, a sheet of thin cardboard is placed in contact between the striker and the incident bar.

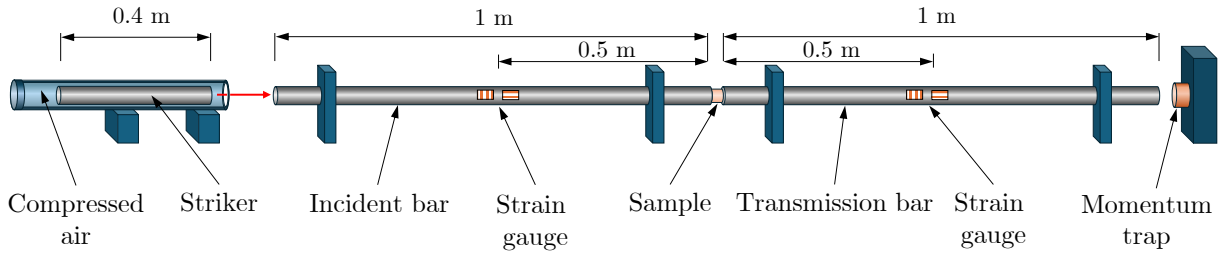

Figure 2.6: Split-Hopkinson Pressure Bar (SHPB) set up for compression testing. Own elaboration.

One-dimensional wave propagation theory is based on 3 assumptions: 1) the bars present a constant cross-section and are made of homogeneous and isotropic materials, 2) the bars are under an elastic regime, and 3) the sample has to be in a dynamic stress equilibrium state. For the SHPB data analysis, the D'Alembert solution to the 1D wave equation is applied (Rueda-Ruiz, 2021), and the engineering strain can be obtained by the following equation:

$$\varepsilon_{eng} = \int_0^t \dot{\varepsilon}_{eng} dt = \int_0^t \frac{V_a - V_b}{l} dt = \int_0^t \frac{c(\varepsilon_i - \varepsilon_r - \varepsilon_t)}{l} dt \tag{2.1}$$

Where ε_{eng} is the engineering strain, t is time, V_a and V_b are the velocities at both sides of the sample, l is the sample length, c is the speed of sound in the bars, obtained by $c = \sqrt{E_{bar}/\rho_{bar}}$, where E_{bar} is the Young modulus and ρ_{bar} is the density of the bar's material. The incident, reflected, and transmitted strain pulses are ε_i, ε_r, and ε_t, respectively.

The engineering stress is calculated using the force measured in the transmission bar as the signal is less noisy. Equation 2.2 shows how to compute engineering stress (σ_{eng}, where F_b is the force in the transmission bar, A_{bar} is the cross-section of the bar, and A_{sample} is the sample's initial cross-section.

$$\sigma_{eng} = \frac{F_b}{A_{sample}} = \frac{A_{bar} E_{bar} \varepsilon_t}{A_{sample}} \tag{2.2}$$

2.4 Dynamic mechanical analysis

Dynamic mechanical analysis (DMA) is a characterization method used to determine the storage modulus E', loss modulus E", and the damping coefficient tan δ as a function of temperature, frequency, or time. E' measures the energy stored in the specimen and is related to the elastic modulus, whereas E" measures the dissipation energy and is related to the viscous modulus. The damping coefficient tan δ relates E' and E" (tan δ = E'/E"). The continuous measurement of E' and E" as a function of temperature or frequency allows to monitor transitions in the crystalline structure of the polymer. Consequently, DMA is a useful technique for measuring the glass transition temperature T_g and other minor phase or structural changes in polymers (Ebnesajjad and Khaladkar, 2005).

The information given by DMA analysis can also be used to characterize a polymer's molecular structure as it can give insight into the number of relaxing units, their size, and mobility (Pukánszky Jr. et al., 2008). Polymer materials typically exhibit two relaxation processes: the α relaxation, which occurs near the T_g, and the β relaxation, which is smaller in amplitude and occurs at temperatures below T_g. While the α relaxation corresponds to more complex and correlated movements of long chains, the β relaxation is connected to localized atomic or molecular motions (Cerveny et al., 2002).

DMA tests were performed on bulk samples printed by *cirp GmbH* in two orthogonal directions: flatwise and edgewise, as illustrated in Figure 2.4d and Figure 2.7. Each sample measured 30 mm in length, 10 mm in width, and 3 mm in thickness. The analyses were carried out using a *DMA Q800* from *TA Instruments*. Two types of DMA tests were conducted on PA12: temperature sweep and frequency sweep.

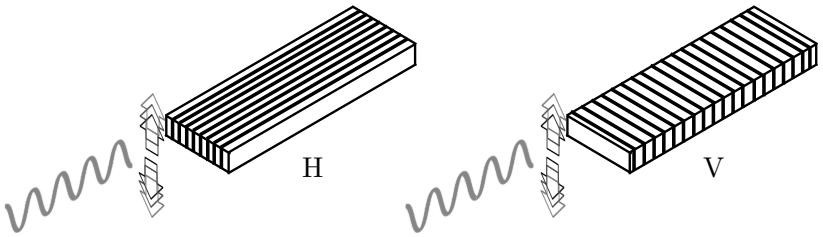

Figure 2.7: Samples used for DMA tests showing the layer directions and the applied oscillating load

2.5 Nanoindentation

Two different kinds of nanoindentation tests were made for different purposes. One type of test, performed at different strain rates, was done to compare the dynamic mechanical properties between the lattices and bulk material. The second type of test, based on modulus mapping and performed in a different nanoindentation system, was used to characterize and identify the different phases present in the material.

2.5.1 Quasi-static nanoindentation and nano-impact tests

Nanoindentation experiments were conducted using a *NanoTest* nanoindentation instrument from *Micro Materials Ltd. (UK)*, equipped with a diamond Berkovich indenter. The area function of the indenter had been previously calibrated with a standard fused silica sample. This instrument consists of a pendulum-based device that uses force actuation and displacement sensing, with the ability to perform energy-controlled nano/micro-impacts. Figure 2.8 provides a schematic overview of the system's key components. Force is applied through a magnet-electromagnetic coil couple, and the pendulum moves around a frictionless pivot. The displacement sensor comprises two capacitor plates aligned with the indenter tip. The instrument components and experimental setup are described in detail in Rueda-Ruiz et al., 2020.

Conventional quasi-static nanoindentation, paired with nano-impact testing, offers direct insight into load-displacement behavior over a wide range of strain rates; components fabricated with SLS can be directly tested with this technique. With these tests, it is possible to accurately assess the polymer's response within lattices with strut diameters below 1 mm. Furthermore, nanoindentation allows for testing in small, defect-free areas, isolating the response of the bulk material from the effects of any microscopic defects.

To display load-displacement curves from the nano-impact tests, the raw data was converted into force-displacement curves by identifying the first peak of the force signal (representing the initial impact of the indenter on the material's surface) and adjusting it to zero. The displacement signal was also offset to zero and corrected for frame compliance and thermal drift. Higher impulse forces (and consequently higher impact velocities) result in greater applied forces due to the higher inertia contribution.

The instantaneous indentation strain rate is defined as $\dot{h}/h$ (Cheng and Cheng, 2004),

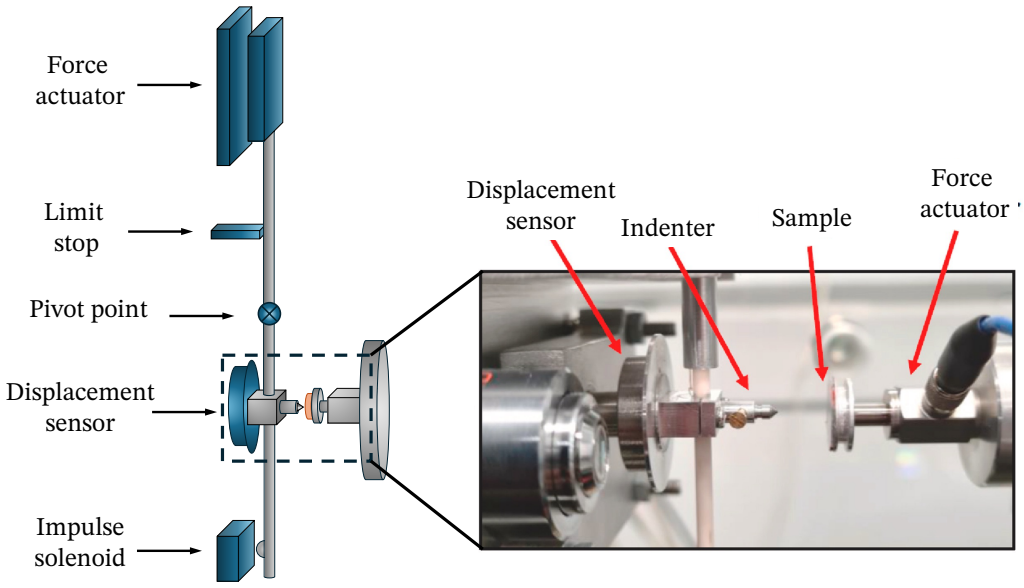

Figure 2.8: Schematics of pendulum-based nanoindentation system.

where h represents the displacement and $\dot{h}$ is the displacement rate, obtained by numerical differentiation of the displacement vector with respect to the time vector. The quasi-static nanoindentation tests were performed using an exponential loading scheme. This resulted in a strain rate that remained constant with respect to indentation depth. However, the strain rate in nano-impact tests could not be controlled (Wheeler, 2009) and varied significantly, starting at very high values (approximately $10^4 s^{-1}$) at the moment of impact and decreasing to zero at the maximum depth, where the indenter stops and rebounds.

To minimize viscoelastic effects on the unloading curve, a 20-second dwell time at the maximum load was implemented during the quasi-static tests, as suggested by Briscoe et al., 1998. Hardness values were determined using the maximum depth recorded before the dwell period to capture rate sensitivity. At the same time, elastic moduli were calculated from the maximum depth following the dwell in accordance with the ISO 14577 standard for instrumented indentation tests. Table 4.10 summarizes the results. Hardness and indentation modulus values show minimal dependence on size, as observed by similar quasi-static results at 25 mN and 50 mN. Hardness values show strain rate dependence, consistent with the reduction in maximum depth in the load-displacement curves at higher strain rates observed. The indentation moduli are notoriously higher compared to macro-scale measurements, typically found in nanoindentation of polymers. This discrepancy is often attributed to the fact that polymers do not fulfill the assumption of elastic unloading that the ISO 14577 standard is based on. Additionally, nano-impact modulus values are slightly higher due to creep effects during unloading, as there is no holding period at maximum load.

Apart from the material measurements obtained by nanoindentation, hardness, and elastic modulus, it is also possible to obtain material parameters that are comparable to those from macro-scale testing, such as yield stress and hardening exponents (Dao et al., 2001). This is accomplished through inverse analyses, which turn indentation metrics into material parameters that can be used in a constitutive model. A common approach uses dimensional

analysis to determine dimensionless functions that relate the indentation data with the parameters of the material model under study. These dimensionless functions are then calibrated using finite element modeling (FEM) (Dao et al., 2001). Recently, Rueda-Ruiz, 2021 developed an inverse analysis technique based on both dimensional analysis and finite element modeling to extract rate-dependent properties of pressure and rate-sensitive materials from nanoindentation data. Since polymers are both pressure and rate-sensitive, this method can be applied to determine the material properties of PA12 that can be compared with macro-scale results. The inverse analysis assumes a linear elastic material (with no viscoelastic effects) and that plasticity is defined by a Drucker-Prager yield criterion that considers the inherent pressure sensitivity of polymers. The approach also assumes perfect plasticity with no hardening. The rate dependency is introduced through a power-law function that relates the compressive yield stress as a function of the strain rate. The dimensional analysis results in the dimensionless function:

$$H = \left(\frac{\dot{h}}{h}\right)^{m} \Pi_H \left(\frac{k\left(\dot{h}/h\right)^{m}}{E_r}, n, \beta, \theta\right) \tag{2.3}$$

where k and m are the power-law function parameters, β is the pressure sensitivity parameter, and θ is the indenter angle. The parameters to be determined are k, m, and β, whereas hardness (H) and indentation modulus (E_r) are obtained from indentation. For the inverse analysis, an input parameter is the pressure sensitivity parameter (β) with a value of 10° (Kimberley et al., 2019; Manaia et al., 2020; Nishida et al., 2013), and two master curves obtained with FEM are used to determine the strain rate sensitivity of the yield stress, m, and the constraint factor Π_h, which relates σ_y with hardness.

The other inputs for the analysis are the apparent hardness H_{ap} and E_r. The apparent hardness is used instead of H as it avoids the uncertainty associated with the estimation of the contact area by using the nominal area, defined by the indenter area function, and the displacement directly measured by the instrument. As a result, the apparent hardness does not consider the sink-in or pile-up of the material around the indenter. The apparent hardness, H_{ap}, is determined by the P/A ratio, where P is the applied force and A is the indenter area function derived from the displacement signal directly measured from the indentation curves.

2.5.2 Nanoindentation mapping

Nanoindentation maps of the samples were performed using a *Hysitron TI950 Triboindenter from Bruker (US)* equipped with a Berkovich diamond tip with a geometry calibrated with a standard fused silica sample of well-known Young's modulus (E = 72 GPa). Each mapping test involved a 20 x 20 array of indents with a spacing of 3.8 µm in the x and y directions. Nanoindentation maps were obtained using the extreme property mapping (XPM) mode of the instrument, which allows the performance of up to 6 indents per second by rapid movements (≈ 10 µm/s) of the piezo transducer between indents and using loading, holding, and unloading times of 0.1 seconds. The indentation load for these tests was 1.5 mN. To obtain the modulus maps, the load-displacement data at each point was then analyzed by using the Oliver and Pharr method (Oliver and Pharr, 1992).

2.6 Thermogravimetric analysis

Thermogravimetric analysis (TGA) is a technique that quantitatively records the mass change in a sample as a function of temperature and time as it is heated up in a furnace to temperatures up to 1600 ℃. This technique is used to measure or track any kinetics, conversion, or mechanism of any process where a mass change is involved. Some of these processes include sample degradation due to oxidation or evaporation of volatile compounds such as water (Saadatkhah et al., 2019).

The analyzer consists of a furnace equipped with a microbalance connected to a sample pan and a temperature programmer and controller. The temperature of the sample is measured by a thermocouple in contact with the sample pan, and the balance weighs the sample mass change. The furnace is connected to the exterior by a purge gas tube through which the volatiles are exited (Saadatkhah et al., 2019).

2.7 X-ray tomography

X-ray tomography is a non-destructive technique that allows the visualization of the interior of solid objects and digitally obtains the volume. The tomography is presented as a series of images, where each image is a slice of the object of a certain thickness, which contains a cross-section of the sample across a plane, like a slice of bread. The digital representation of the object's volume is obtained by stacking all the slices together (José Baruchel, 2000).

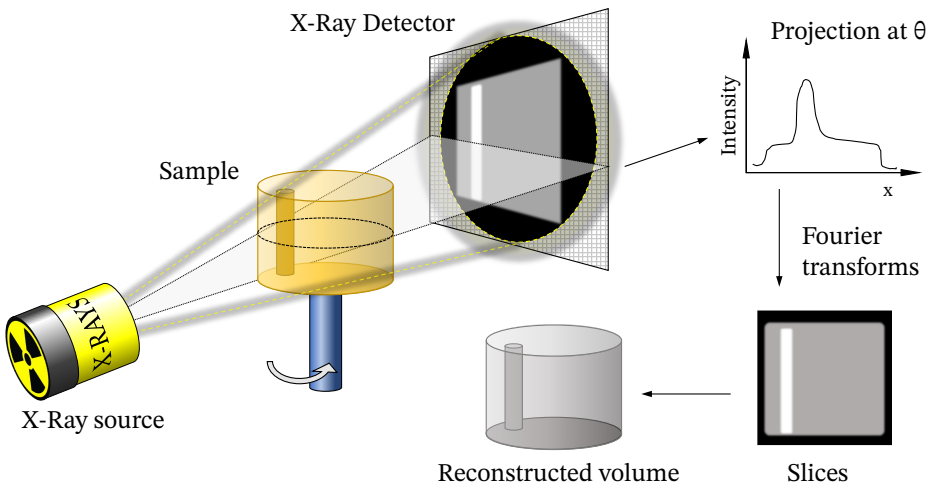

Figure 2.9: Schematic representation of X-ray tomography.

X-rays interact with the object by the Lambert-Beer law; they are attenuated inside the material, and a detector captures the intensity of the attenuated ones. The incident beam is attenuated along the material by its composition and density variations. The sum of the attenuations of the different X-ray paths along the material at a specific angle constitutes a projection (Fig.2.9). The material is rotated through 180° to obtain a set of projections. Then, the tomographic reconstruction is done using the Fourier Slice theorem, which states that a

1D Fourier transform of the projection function at a certain angle is a line in a 2D Fourier representation of the object. The full 2D Fourier representation of the object is built from the projection set at the angle range from 0 to 180°. With a 2D inverse Fourier transform, the object is reconstructed and presented as a stack of grey-scaled images (José Baruchel, 2000; Herman, 2010).

After the tomographic scans, volumetric images were generated using a standard filtered back-projection algorithm. After the volume is reconstructed, the 3D images are post-processed and analyzed using ImageJ. The raw volumes were segmented, transforming the greyscale images to binary to eliminate all possible processing problems caused by noise, background, or uneven illumination and increase the contrast between material and pores. Using ImageJ, the porosity was obtained by calculating the effective cross-section of each slice and dividing it by the equivalent cross-section with all the internal pores closed. In addition, the representative volumes for the simulations were obtained directly from the raw reconstructed volumes by downscaling them to the resolutions shown in Table 5.3 to optimize simulation times. At the end, each RVE is rendered with approximately 256^3 voxels. A detailed description of how the tomographies are converted into RVEs is explained in section 3.3.1.

2.7.1 Porosity calculation

To study the porosity from the grey-scaled tomographic images (Fig.2.10a), the image stack was processed to produce binary images using the *ImageJ* software package. The sample volume was calculated by counting the black and white pixels of the image stack. The volume obtained, called real volume, considers the internal defects and surface roughness (Fig.2.10b). To quantify the porosity of the 3D-printed lattices, two methods were used:

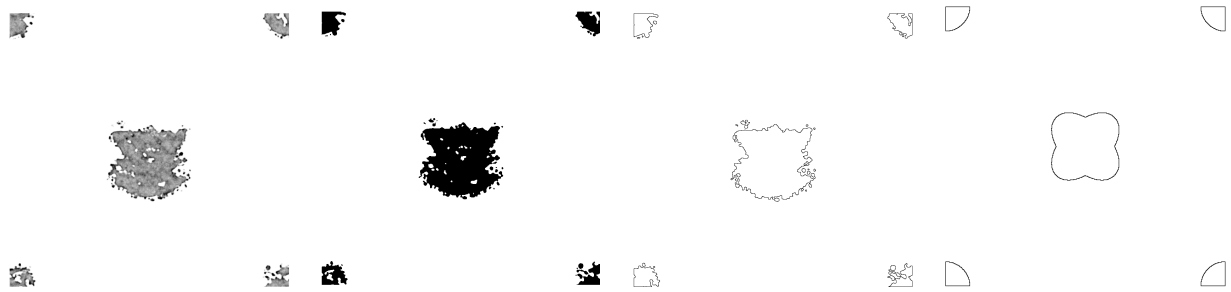

Figure 2.10: Centre cross sections slices from A1 tomographic images and digital design, where (a) is the tomography, (b) is the binary version of the tomography, (c) is the contour of the tomography, and (d) is the as-designed volume

With the first method, the internal porosity was studied. To calculate the internal porosity, a reference volume was obtained by counting the pixels inside the surface contour of the images, where the internal porosity is filled with pixels (Figure 2.10c). In this way, the reference volume was the same as the real one but without internal defects. Internal porosity was calculated with equation 2.4, where P_i means internal porosity, V_{real} the real volume, and V_{ref} the reference volume, where the internal pores have been manually removed.

$$P_i = 1 - \frac{V_{real}}{V_{ref}} \tag{2.4}$$

The second method explains the difference between the real volume (3D printed) and the as-designed volume (computer-designed) on which the real volume is based. The original volume, as designed, is the ideal one and has no internal defects and surface roughness. Its value was obtained by counting the pixels inside its surface contour (Fig.2.10d). The relation between both volumes was called virtual porosity, which is calculated with equation 2.5, where P_v means virtual porosity and V_{des} the as-designed volume.

$$P_v = 1 - \frac{V_{real}}{V_{des}} \tag{2.5}$$

2.8 Differential scanning calorimetry

Differential scanning calorimetry is a thermodynamically analytical technique used to directly measure the heat flow associated with the phase transitions of a material as a function of temperature. It is commonly used to study the thermal properties of polymers, pharmaceuticals, biomolecules, and other materials (Drzeżdżon et al., 2019; Gill et al., 2010).

A differential scanning calorimeter is equipped with a furnace that contains two pans. The sample of interest and a reference are placed on each pan and the temperature inside the furnace is precisely controlled over a specific temperature ramp and heating rate. Each pan is attached to a sensor that measures the heat flow as the temperature in the furnace varies. In DSC, the difference in the heat flow between the sample and the reference as a function of time and temperature is measured. The calorimeter measures the heat flow required to maintain both sample and reference at the same temperature, and the measurements are recorded on a computer. The resulting DSC scan with the reference data subtracted is plotted as a thermogram that presents peaks corresponding to endothermic and exothermic reactions as the sample is heated or cooled (Drzeżdżon et al., 2019; Gill et al., 2010).

During the melting of a polymer (endothermic reaction), the material absorbs heat until the energy is enough to produce the free movement of the chains, which is reflected as an endothermic peak. On the contrary, during crystallization, the polymer chains acquire low energy equilibrium positions, releasing heat, which is shown as an exothermic peak on the thermogram. With the endothermic or exothermic peak maximum position, the melting and crystallization temperatures can be obtained (Drzeżdżon et al., 2019; Gill et al., 2010).

In addition, DSC can be used to find other transition temperatures, latent heats, phase transitions, or even estimate the degree of crystallinity as:

$$\chi_c = \frac{\Delta H}{\Delta H_m} \times 100 \tag{2.6}$$

Where ΔH corresponds to the enthalpy of fusion of the sample, calculated as the area under the first heating curve ranging from its T_g, 53 ℃ (Cobian et al., 2022), calculated in section

4.2, to 200 ℃, and ΔH_m is the enthalpy of fusion of a theoretical 100 % crystalline PA12 with a value of 209.2 J/g (S. Gogolewski and Gastorek, 1980).

2.9 X-ray scattering: WAXS and SAXS

X-ray scattering is a powerful tool used to determine the structure of materials at the atomic and molecular level by observing the interaction between an incident monochromatic X-ray and the internal structure of the sample. In general, scattering is produced when a wave with a specific wavelength goes through a series of periodically spaced obstacles, with a separation similar to the wavelength of the radiation, which causes the X-rays to change direction, energy, or both. The interference of the scattered waves results in a scattering pattern that provides details about the arrangement of the obstacles and insights into the molecular or atomic structure and composition of the material.

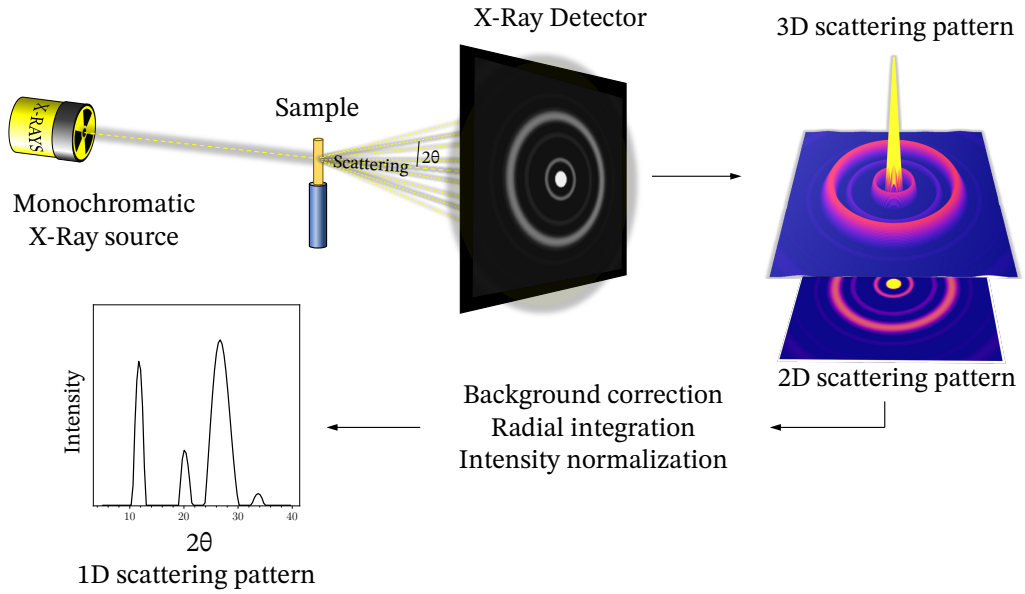

Figure 2.11: Schematic representation of X-ray scattering on a semicrystalline sample.

This technique is based on Bragg's Law which states that when a monochromatic X-ray beam hits a crystalline material, the incidence angle θ is the same as the angle at which it is scattered back, resulting in constructive interferences when the difference in the paths traveled by the scattered rays, d, is an integer multiple, n, of the X-ray's wavelength λ, or destructive interferences when this is not fulfilled. In general, the first-order scattering ($n = 1$) presents a higher intensity than those of superior order ($n > 1$) (Güemes Gordo and Martín Piris, 2012).

$$n\lambda = 2dsin\theta \tag{2.7}$$

The X-ray source comprises a high-voltage generator that applies a voltage between an anode and a cathode. In general, the cathode uses a tungsten filament that, when heated up by

an electrical current, emits electrons. The electrons are accelerated by an electric field and reach the anode at high velocity. The anode is made of a pure metal, generally copper or molybdenum, so when the accelerated electrons hit the anode, an electron from the internal orbitals of an anode's atom is excited to a higher state. After returning to a stable position, an outer shell electron occupies the position left behind by the excited one, emitting energy in the form of electromagnetic radiation with wavelengths corresponding to the X-ray spectrum. Up to this point, the X-rays used in X-ray tomography and X-ray scattering are the same. However, for X-ray scattering, a monochromatic beam is needed, and it is achieved by using a filter that selects a band within a maximum in the spectrum known as K_α. In the case of a Cu anode, $\lambda_{CuK_\alpha} = 1.5418$ Å, and for Mo, $\lambda_{MoK_\alpha} = 0.7107$ Å, which are of the same order of magnitude as the atomic-scale structure of materials (Güemes Gordo and Martín Piris, 2012).

To sum up, the X-rays emitted by the anode hit the material and interact with its crystalline structure, causing the X-rays to scatter in various directions that produce constructive or destructive interferences. The constructive interferences lead to bright spots, rings, or discs in the detector if the material is crystalline, semicrystalline, or amorphous, respectively. However, when the interferences are destructive, they lead to dark areas on the detector. The intensity and angles of the scattered X-rays are detected by the detector. This information is used to create the scattering patterns, where the bright spots, rings, or discs are converted into peaks with infinitesimal, large, and larger widths, respectively, which are later analyzed to determine the atomic or molecular structure of the sample. The process to obtain 1D scattering patterns is explained later in this section. Figure 2.11 shows a schematic representation of this technique on a semicrystalline sample. As the X-rays need to cross the samples, the specimen thickness is limited to a few mm.

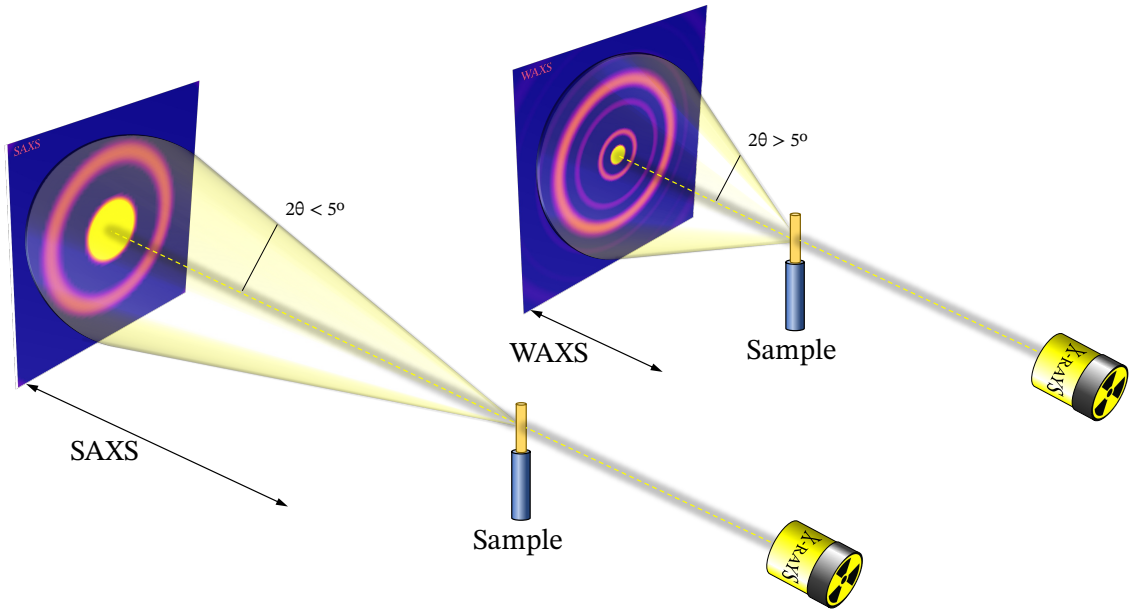

Figure 2.12: Schematic representation comparing WAXS and SAXS analysis techniques.

In this work, two scattering techniques are used: wide-angle and small-angle X-ray scattering,

abbreviated as WAXS and SAXS, respectively. An illustrative example of the differences between WAXS and SAXS is shown in Figure 2.12.

The Wide-angle X-ray Scattering (WAXS) technique provides information about short-range order in a material, making it useful to study it at the atomic scale to get the crystallinity and d-spacing and identify crystalline and amorphous phases of materials. WAXS analysis measures wide scattering angles, where 2θ is over 5°. These patterns are achieved by placing the samples close to the detector, at distances close to 50 cm (L. Liu et al., 2013; Rigaku, 2024).

Small-angle X-ray Scattering (SAXS) is used to study larger structures at nanometric and micrometric scales, such as macromolecules, spherulite size, and the long spacing of polymers semicrystalline materials (see Figure 2.13). SAXS measures scattering at angles below 5°, providing information about the size, shape, and distribution of particles in a sample. Compared to WAXS, for SAXS analysis, the sample is placed further away from the detector, at distances higher than 600 cm (L. Liu et al., 2013; Rigaku, 2024).

In addition, Figure 2.13 illustrates a schematic representation of a spherulite from a semicrystalline polymer, indicating the amorphous and crystalline regions, the d-spacing (d), and long spacing (L) dimensions that can obtained from WAXS and SAXS, respectively.

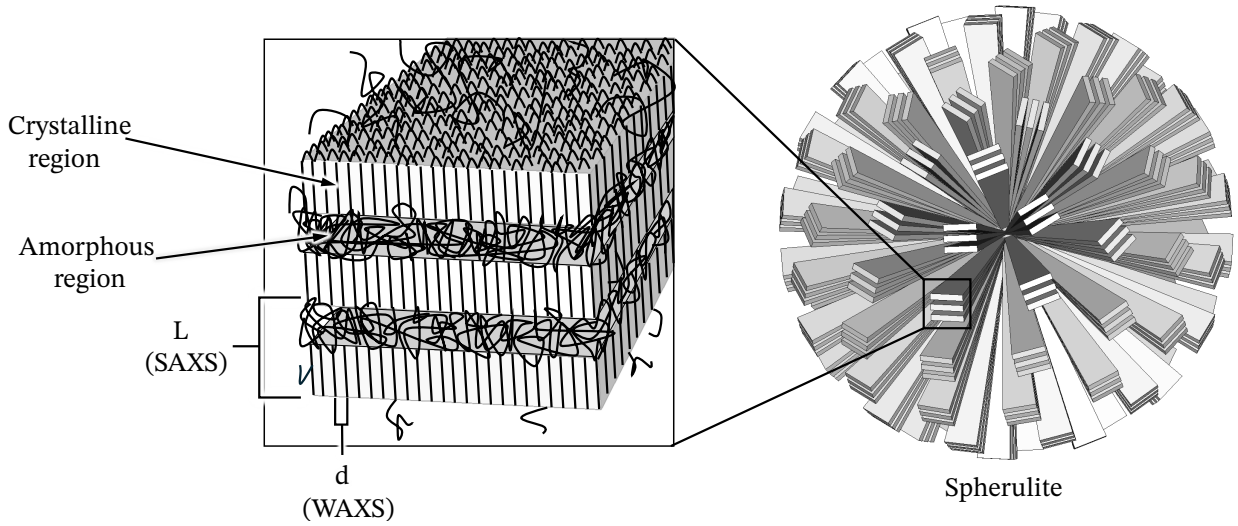

Figure 2.13: Schematic of polymer chains arrangement showing the dimensions of d-spacing (d), measured by WAXS and long spacing (L) dimensions estimated by SAXS.

The 2D data from SAXS and WAXS was first processed using the *SAXSanalysis™* commercial software. First, a background correction was performed on the scattering data, and then the 2D patterns were radially integrated to obtain 1D scattering patterns, which were normalized by their intensity. In the end, the intensity was plotted against the scattering vector q in the case of SAXS and the angle 2θ in the case of WAXS patterns. 2θ and q can be related to equation 2.8, where d is the d-spacing. In addition, a Lorentz correction (2.9) was applied to the scattering intensity on SAXS patterns (Cser, 2001).

$$q = \frac{2\pi}{d} \tag{2.8}$$

$$I = I_0 q^2 \tag{2.9}$$

1D patterns were fitted with Voigt functions using the software Fityk to identify the peak position. In the WAXS scattering pattern, some peaks correspond to the amorphous halo and others to the crystalline phases. The crystallinity degree can be obtained as:

$$X_c = \frac{\sum A_{ci}}{\sum A_{ci} + A_a} \times 100 \tag{2.10}$$

where A_{ci} is the area under the crystalline peak i and A_a is the area under the amorphous halo. The total area value under the WAXS 1D scattering pattern is the sum of all the peaks. The d-spacings on the WAXS peaks and thickness of the long spacing (L) are calculated using Bragg's Law (equation 2.7), d is d-spacing or long spacing in the case of WAXS and SAXS polymer patterns, respectively.

Chapter 3

Numerical analysis techniques

3.1 FFT based computational homogenization: The FFTMAD code

Fast Fourier Transform (FFT) based homogenization is a simulation framework approach that aims at obtaining the mechanical response of heterogeneous materials based on the numerical simulation, using Fast Fourier-based solvers, of the response of a Representative Volume Element (RVE) of the material microstructure. The RVE is loaded with macroscopic stress or strain, and the solver obtains, under periodic boundary conditions, the strain and stress micro fields with an average equal to the macroscopic prescribed fields. For these FFT-based homogenization simulations, the code FFTMAD is used. FFTMAD is a generalist FFT-based homogenization code developed at IMDEA Lucarini et al., 2022, which will be the framework for the FFT homogenization of lattice materials. It is designed in four modules: input generation, material definition, solvers, and post-processing modules. The input generation module generates the RVE, which is defined as a voxel-based distribution of phases in a volume. The material models can be introduced with the material module by a UMAT, a general subroutine defined for Abaqus FE code. The simulation outputs are the local stress-strain fields, which can be visualized with *Paraview*.

The most useful characteristics of FFT-based approaches are the very low computational cost (compared with FE) for problems involving periodic boundary conditions and the direct simulation of a regular discrete volume without the need for a mesh. Instead, the volume is divided into a uniform grid with units called voxels, with some mechanical properties associated, including empty spaces that are considered materials with negligible stiffness. Several algorithms can be found to solve the homogenization problem, which consists of finding the strain and stress fields at the microscale that are compatible and in equilibrium. FFT approaches' convergence rate and accuracy strongly depend on the contrast between the phases represented in the domain. In the case of lattice structures, the contrast is infinite because of the phases is indeed empty space. In a recent article, Lucarini et al., 2022, a particular FFT framework based on the Galerkin FFT approach, the use of alternate frequencies, and surface smoothing have been proposed as a very efficient approach for lattice materials.

3.1.1 Galerkin adapted for Lattice Materials

The Fourier-Galerkin approximation is taken as the initial point. This approach has a fast convergence rate for limited phase contrast. This method is adapted for lattices by changing the iterative linear solver, introducing an alternative differentiation scheme, and using mixed macroscopic control (Lucarini et al., 2022). The resulting method is presented in this section.

For a given heterogeneous periodic discretized domain Ω, the weak form of the equilibrium in small strains can be written as,

$$\mathcal{F}^{-1}\left\{\widehat{\mathbb{G}}\left(\boldsymbol{\xi}\right):\mathcal{F}\left\{\boldsymbol{\sigma}\left(\boldsymbol{x}\right)\right\}\right\}=\mathbf{0} \tag{3.1}$$

where the Fourier transform and the inverse Fourier transform are represented by $\mathcal{F}$ and $\mathcal{F}^{-1}$ respectively, $\boldsymbol{x}$ is the position, $\boldsymbol{\xi}$ the spatial frequency vector, $\boldsymbol{\sigma}$ is the Cauchy stress, and $\widehat{\mathbb{G}}$ is the Fourier transform of a linear operator which projects any arbitrary tensor field into its compatible part (Vondrejc et al., 2014). The discrete form of the eq.3.1 is a linear system of algebraical equations in which the value of the strain $\boldsymbol{\epsilon}$ at the center of each voxel is the unknown.

In this case, $\boldsymbol{\xi}$ corresponds to the modified frequencies, following the work of Willot, 2014, which provide a smoother response and better convergence. These frequencies are

$$\xi'_p = i2\frac{N_p}{L_p}\tan\left(q_p/2\right)\prod_{p=1}^{d}\frac{1}{2}\left(1+e^{(iq_p)}\right) \quad \text{with} \quad q_p = 2\pi\frac{n_p - N_p/2}{N_p} \in [-\pi,\pi] \tag{3.2}$$

where $i=\sqrt{-1}$ is the imaginary unit and L_p, n_p and N_p are the length of the cell edge, n^{th} voxel and the total number of voxels in direction p, and $d=1,2$ or 3 is the space dimension. The Fourier transforms are computed using the direct and inverse Discrete Fourier Transform and are carried out using the FFT algorithm. This algorithm is the main reason for the high performance of spectral solvers (Lucarini et al., 2022).

The macroscopic state is provided as a combination of macroscopic strain components kl, $\boldsymbol{\varepsilon} = \varepsilon_{kl}(\boldsymbol{e}_k \otimes \boldsymbol{e}_l)^{sym}$ or macroscopic stress components KL, $\boldsymbol{\sigma} = \sigma_{KL}(\boldsymbol{e}_K \otimes \boldsymbol{e}_L)^{sym}$ with $kl \cap KL = \emptyset$. For these general loading conditions, the expression of the projector operator in the Fourier space follows (Lucarini and Segurado, 2019):

$$\widehat{\mathbb{G}}_{ijkl}(\boldsymbol{\xi}) = \begin{cases} \mathbb{I}^s_{ijKL} & \text{if } \boldsymbol{\xi}=\mathbf{0} \text{ for components } KL \\ 0_{ijkl} & \text{if } \boldsymbol{\xi}=\mathbf{0} \text{ for components } kl \\ 0_{ijkl} & \text{for Nyquist frequencies} \\ \left[\mathbb{I}^s_{ijkl}\xi_j\xi_l\right]^{-1}\xi_j\xi_l & \text{for } \boldsymbol{\xi}\neq\mathbf{0} \end{cases} \tag{3.3}$$

where $\mathbb{I}^s$ is the fourth order symmetric density tensor and $\mathbb{G}$ should be symmetrized to account for major and minor symmetries.

In the case of lattices, the system of equations of Eq. 3.1 does not have a unique solution because of the presence of voids where the strain field is undetermined. Therefore, the Minimal

Residual (MINRES) solver is used as the iterative linear solver to obtain an equilibrium and compatible solution (Lucarini et al., 2022).

3.2 Finite Element adaptation based homogenization

FE will be used as a complementary simulation technique to obtain the response of computer-designed geometries without considering internal defects. As in FFT, the method defines an RVE corresponding to one or several lattice cells. The problem is solved using a standard non-linear FEM approach in which the only special characteristic is the use of periodic boundary conditions. According to (Segurado and Llorca, 2013), periodic boundary conditions are imposed on opposite sides of the mesh of the representative volume to obtain a homogenized response from FE simulations. If the mesh is considered to be inside an imaginary bounding box whose concurrent edges define an orthogonal basis $\boldsymbol{e}_1$, $\boldsymbol{e}_2$ and $\boldsymbol{e}_3$ with corresponding coordinates x_1, x_2, x_3, some mesh nodes are in contact with the concurrent bounding box faces. Periodic boundary conditions impose constraints on the displacement of those nodes $\boldsymbol{u}$, such that the relative displacement between two nodes located on the same planar positions of opposite faces is constant and equal to the macroscopic prescribed deformation gradient $\boldsymbol{F}$ as

$$\begin{aligned}
\boldsymbol{u}(x_1, x_2, 0) - \boldsymbol{u}(x_1, x_2, L_3) &= (\boldsymbol{F} - \mathbb{1})\boldsymbol{L}_3 \\
\boldsymbol{u}(x_1, 0, x_3) - \boldsymbol{u}(x_1, L_2, x_3) &= (\boldsymbol{F} - \mathbb{1})\boldsymbol{L}_2 \\
\boldsymbol{u}(0, x_2, x_3) - \boldsymbol{u}(L_1, x_2, x_3) &= (\boldsymbol{F} - \mathbb{1})\boldsymbol{L}_1
\end{aligned} \tag{3.4}$$

where L_i are the dimensions of the bounding box and $\boldsymbol{L}_i = L\boldsymbol{e}_i$. With these boundary conditions, the deformed configuration of the RVE is still periodic and fills the space by translation. The displacement vectors are prescribed by setting the displacement of three master nodes corresponding to each concurrent bounding box face. The FE software Abaqus is used for Finite Element Method simulations in this work.

3.3 Generation of representative volume elements for simulations

Two different kinds of representative volume elements (RVEs) have been used for numerical analysis. The first kind of RVEs have been directly obtained from the tomographies taken with the procedure explained in section 5.2.2.2, whereas the second kind of RVEs are the ones made from as-designed samples with a lattice generator script or the help of computer-aided software. The procedure for obtaining tomographic (as-printed) and for as-designed RVEs are explained in sections 3.3.1 and 3.3.2.

3.3.1 RVE generation from tomographies

The volume obtained by the tomographies as the combination of all the images in the stack, Figs.3.2a and 3.2c can be reconstructed in different formats to perform different analyses and

simulations.

Volume reconstruction from tomographies to voxels makes it possible to directly simulate in FFT-based solvers the actual shape of the additively manufactured samples including the internal defects. To do this, the tomographic binary images in the stack, with a resolution of thousands of pixels, were reduced to images around 256 pixels per side, rendering a volume of 256^3 voxels approximately, which is the optimal working size for FFTMAD simulations. The reason for downsizing a binary image stack instead of the original tomographic gray-scaled images is to avoid the excess information and noise that occur when the latter are downsized. Downsizing gray-scaled images leads to blurring effects, making it difficult to distinguish defects. When the binary images are downsized, new smaller greyscale images are produced, as *ImageJ* software package takes the average color value of a pixel and its neighbors when downsizing an image as shown in Figure 3.1.

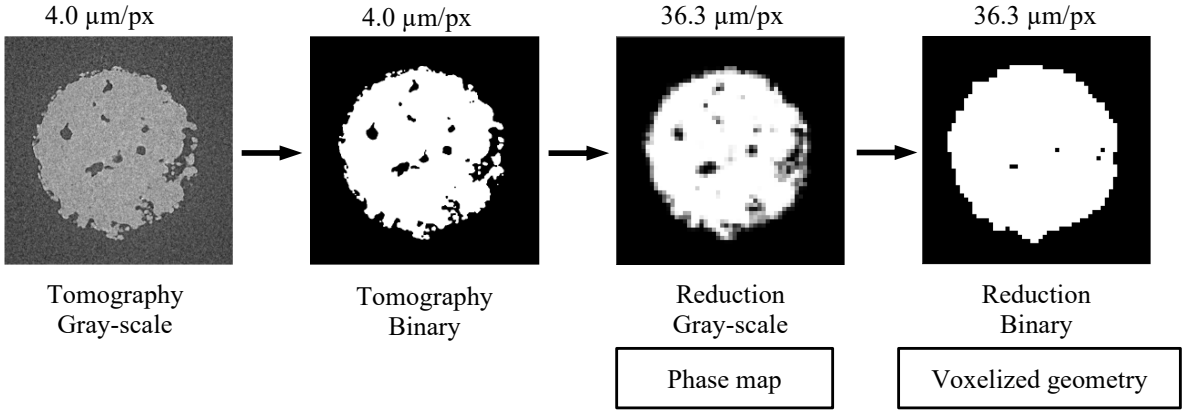

Figure 3.1: Process for obtaining the RVE for FFT simulations from tomographic volumes. In this case a slide of a single 1.5 mm diameter strut is shown.

These grey-scaled reduced images were used to create the phase map, which is a continuous field that assigns values between 0 (void) and 1 (material) to voxels, creating a smooth transition at the interface to improve numerical stability and accuracy during FFT simulations. The voxelized volume was obtained by producing binary images from the reduced grey-scale images. The voxelized volume and phase map combination gives the smoothened surface volumes shown in Figs.3.2b and 3.2d.

This reconstruction process is fast, simple, and can be automatized. These characteristics make FFT-based homogenization advantageous over finite element methods (FEM), where a very fine smooth mesh has to be generated to represent surfaces with roughness and internal defects directly from tomographic images. The meshing process requires the use of complex meshing algorithms and the intervention of a user and results in very large models, computationally very expensive. When creating a mesh that demands excessive computational resources, it is common to use different meshes: a coarser one for the general geometry of the sample and finer meshes for defects (Amani et al., 2018, 2020; Sombatmai et al., 2021; Vanderesse et al., 2011).

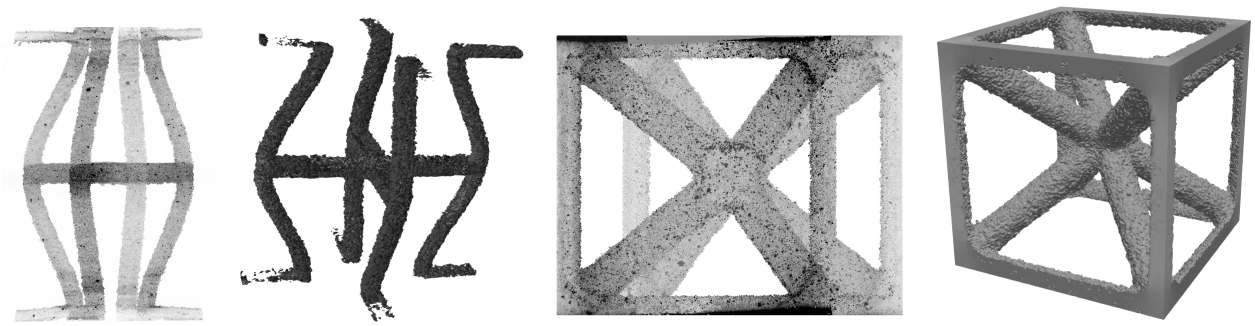

(a) **(b)** **(c)** **(d)**

Figure 3.2: Volume reconstruction of the tomographies from the PA12 samples, where (a) is a 3D tomography of part of an auxetic unit cell, (b) the reconstructed auxetic volume, (c) is a 3D tomography of a BCC unit cell, and (d) the reconstructed BCC cell volume.

3.3.2 Parametric RVE generation for as-designed geometries

A Python script has been developed to create lattice models parametrically for FFTMAD and FEM simulations. The script is published in MOAMMM, 2024 online repository and is limited to unit cell geometries composed of cylindrical struts. The script introduces the nodes and connectivities of every strut that forms the desired geometry, the dimensions of the bounding box where the geometry is embedded (unit cell), and finally, the struts' radius dimension or the volume fraction occupied by the geometry within the bounding box. The script then calculates the volume fraction or radius depending on the input introduced. The script generates 3 outputs:

The voxelized volume (Fig.3.3a) with 0 and 1 value voxels represent the voids and material properties conforming to the unit cell geometry. A *phase map* (Fig.3.3b) with values between 0 and 1 to smooth the interface between material and voids, and a folder to generate a FEM mesh (Fig.3.3c) with *gmsh* software. The first two files are used for FFT simulations.

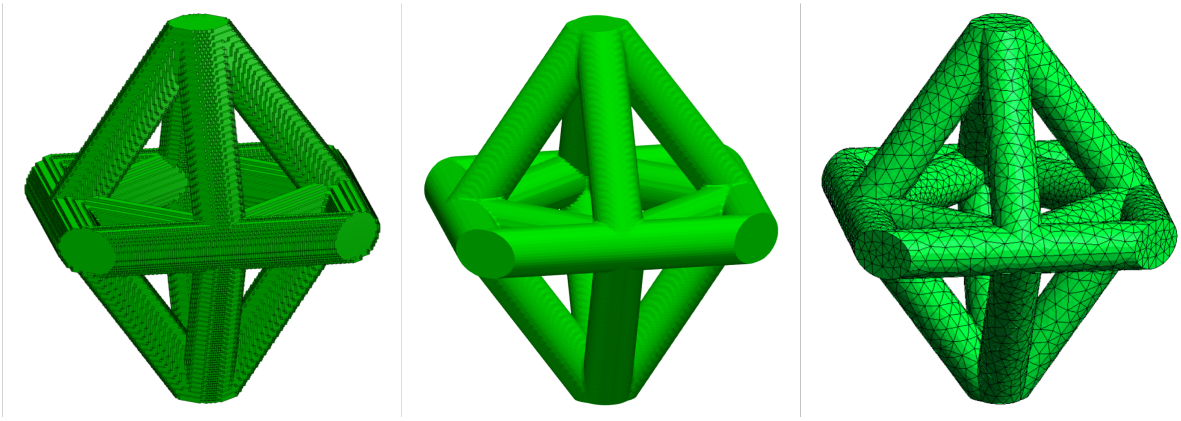

(a) **(b)** **(c)**

Figure 3.3: Example of parametric generation of a lattice unit cell, where (a) is the voxelized geometry, (b) is the voxelized geometry with the phase map implemented, and (c) is the volume mesh.

The actual geometry is rasterized to obtain the voxelized volume and phase map. To this aim, the script calculates the distance from the point representing the center of the voxel v_{ijk} to each vector representing the direction of the struts. If the distance is smaller than the radius minus half the length of a voxel, the point is inside the geometry, and the value associated with the voxel is 1. If the distance exceeds the radius plus half the voxel length, the voxel is outside the strut, and the voxel value becomes 0. The interface is defined by those distance values between the radius plus minus the distance to the voxel's center. Depending on how far the voxel's center is from this coordinate, the phase map corresponding to the location of the voxel acquires a value between 0 and 1. The voxel map is obtained from the phase map, substituting the values higher than 0 into 1.

3.3.3 FE Mesh Generation

For FEM simulations done with the commercial software Abaqus, the mesh used contained quadratic tetrahedral C3D10, and the mesh element size was proportional to 3.33 times the radius. Periodic conditions were applied to obtain the lattice behavior by homogenization from FEM simulations, as explained in section 3.2.

3.4 Phase field fracture implementation in FFTMAD

To study and compare crack nucleation and propagation with in-situ tests, a phase-field fracture model has been implemented in FFTMAD (Aranda et al., 2022; Zarzoso, 2023). The model was proposed in Miehe et al., 2010 to simulate brittle fracture in a variational form. This fracture model calculates the balance between the stored and dissipated energy during crack formation, and the crack is modeled as a smooth phase-field (ϕ), with values ranging from 0 to 1, determining the degree of damage (Miehe et al., 2010). The total energy functional is defined by the elastic stored energy (E), the dissipation energy when a new crack is forming (D), and the energy imposed by external mechanical loading (P).

$$\Pi(\boldsymbol{u}, \phi) = E(\boldsymbol{u}, \phi) + D(\phi) - P(\boldsymbol{u}) \tag{3.5}$$

The equation 3.6 determines the value of the phase field ϕ and is obtained from the first variation of the total free energy functional with respect to the phase field and enforcing it to 0 ($\partial\Pi/\partial\phi = 0$),

$$\frac{G_c}{l_{car}}\left[\phi - l_{car}^2 \Delta\phi\right] = 2(1-\phi)\mathcal{H} \tag{3.6}$$

The properties required to characterize the fracture are the characteristic length (l_{car}) and fracture energy (G_c). The field ($\mathcal{H}$) is a history variable that is obtained from the current local elastic energy density available to produce crack propagation and its maximum historic value in order to account for damage irreversibility. Although the original model does not account for nucleation (meaning that the resistance in the absence of cracks should be infinite), both

magnitudes, G_c and l_{car}, indirectly define an effective strength (σ_y). The model assumes a linear elastic behavior without cracks, characterized by E and ν.

For the mechanic problem, the equation of linear momentum at equilibrium is obtained by taking the first variation of the total free energy functional with respect to the total imposed strain and equating it to 0 ($\partial\Pi/\partial\varepsilon = 0$). Furthermore, the elastic potential E energy provides the expression of the stress, linearly related to the strain in the case of a quadratic strain energy. In this small strain framework, the strain is the symmetric spatial gradient of $\boldsymbol{u}$, which satisfies the principle of objectivity. The definition of the elastic energy density of a damaged material allows to restrict the effect of damage only to some part of the energy; here, the energy originated by positive elastic strain energy (Miehe et al., 2010). This decomposition of the energy in positive and negative is done using the spectral decomposition of the strain tensor. As a result, the degradation function $g(\phi) = (1-\phi)^2$ only affects the terms acting on the positive strain part.

$$\begin{cases} \nabla \cdot \sigma(\boldsymbol{u}, \phi) = 0 \\ \sigma = (1-\phi)^2[\lambda \langle \mathrm{tr}(\varepsilon) \rangle_+ \boldsymbol{I} + 2\mu\varepsilon_+] + [\lambda \langle \mathrm{tr}(\varepsilon) \rangle_- \boldsymbol{I} + 2\mu\varepsilon_-] \end{cases} \tag{3.7}$$

$$\varepsilon = (\nabla \boldsymbol{u} + (\nabla^T \boldsymbol{u}))/2 \tag{3.8}$$

The full mechanical problem is given by equations 3.6 and 3.7, which are solved in a staggered way. As done in the predictor-corrector algorithm, first, the mechanical problem is solved in each step with the damage frozen as the one in the last step. Then, the damage is calculated for that mechanical state until both problems converge, obtaining the strain and damage fields (Zarzoso, 2023).

The target macroscopic strain ($\boldsymbol{\varepsilon}$) is applied in small strain increments that depend on the time step (Δt) as $\delta\varepsilon = \varepsilon/t_{tot} \cdot \Delta t$. At each step, a strain increment is added to the local strains (ε_t), giving $\varepsilon_{t+1} = \varepsilon_t + \delta\varepsilon$ and taking the damage frozen from the previous step $\phi_{t+1} = \phi_t$. The local strains in the actual step $\varepsilon^k_{t+1} = \varepsilon_{t+1}$, and the damage taken for this step $\phi^k_{t+1} = \phi_{t+1}$ as taken as initial variables for the staggered scheme. Then, the mechanical equilibrium is obtained, resulting in a new local strain ε^{k+1}_{t+1}, which modifies $\mathcal{H}$ from equation 3.6, calculating a new damage ϕ^{k+1}_{t+1}. The convergence is achieved when the errors, calculated as the norm of the change in strains and damage with respect to the values at the beginning of the step, are smaller than a certain tolerance, evaluated as $err_{stagg} = \max\{err_\varepsilon, err_\phi\}$ (Zarzoso, 2023).

For the mechanical problem, the Fourier-Galerkin approximation is taken, as explained in section 3.1.1. Helmholtz equation, Eq. 3.1 is solved using the conjugate gradient, so the phase field equation is rearranged to be expressed as a linear system,

$$\left[\frac{G_c}{l_{car}} + 2\mathcal{H}\right]\phi - G_c l_{car}\Delta\phi = 2\mathcal{H} \tag{3.9}$$

This linear equation is solved by computing the laplacian of damage in Fourier space as,

$$\Delta\phi = \mathcal{F}^{-1}[\xi \cdot \xi\mathcal{F}[\phi]] \tag{3.10}$$

3.5 Non-linear response: Finite strains Viscoelastic - Viscoplastic material model

A viscoelastic-viscoplastic model for finite strains (VEVP) has been used in both FFT and FEM simulations to predict the mechanical behavior of PA12 unit cells based on the experimental data. In particular, the material model used is isotropic Linear Viscoelastic with nonassociated Perzyna-type Viscoplasticity and tension-compression asymmetry. The viscoelastic part is based on the Standard Linear Solid model with Maxwell branches and is linear in terms of driving forces. This model can capture rate-dependent plastic and elastic response, and different yield points in tension and compression are captured too. In addition, the model has isotropic hardening, which is observed in PA12 during the experiments. The viscoelastic-viscoplastic material model is explained in detail in the work by Nguyen et al., 2016 and will be summarized here,

3.5.1 Kinematics

The deformation gradient $\boldsymbol{F}$ is decomposed into a viscoelastic and a viscoplastic part (Moran et al., 1990):

$$\boldsymbol{F} = \boldsymbol{F}^{ve} \cdot \boldsymbol{F}^{vp} \tag{3.11}$$

Assuming irrotational viscoplastic flow, the asymmetric viscoplastic strain rate tensor is given by:

$$\boldsymbol{D}^{vp} = \dot{\boldsymbol{F}}^{vp} \cdot \boldsymbol{F}^{vp-1} \tag{3.12}$$

where $\dot{\boldsymbol{F}}^{vp}$ is the plastic evolution. The viscoelastic strain is defined using a logarithmic operator where $\boldsymbol{C}^{ve}$ is the right Cauchy strain tensor from the viscoelastic part:

$$\boldsymbol{E}^{ve} = \frac{1}{2} \ln \boldsymbol{C}^{ve} \tag{3.13}$$

3.5.2 Viscoelastic part

The generalized Maxwell model is used to simulate the viscoelastic behavior with free energy and flow potentials for the spring and dashpot of each branch, respectively. For the spring, the free energy is related to the bi-logarithmic potential function:

$$\Psi_i(\boldsymbol{C^{ve}}) = \frac{K_i}{2} \ln^2 J^{ve} + G_i(\mathrm{dev}\boldsymbol{E^{ve}}) : (\mathrm{dev}\boldsymbol{E^{ve}}) \text{ with } i = \infty, 1, ..., N \tag{3.14}$$

K_i and G_i with $i = \infty, 1, ..., N$ represent the bulk and shear moduli associated with the Maxwell branches. The flow potential in the dashpot is related to the quadratic dissipation

function:

$$\Upsilon_i(\boldsymbol{E^{ve}}, \boldsymbol{q_i}) = -\boldsymbol{q_i} : \boldsymbol{E^{ve}} + \left[\frac{1}{18K_i}(\mathrm{tr}\boldsymbol{q_i})^2 + \frac{1}{4G_i}\mathrm{dev}\boldsymbol{q_i} : \mathrm{dev}\boldsymbol{q_i}\right] \text{ with } i = 1, ..., N \tag{3.15}$$

where $\boldsymbol{q_i}$ are the internal tensorial variables controlling the viscoelastic process and are characterized by the retardation actions:

$$\mathrm{dev}\dot{\boldsymbol{q}}_{\boldsymbol{i}} = \frac{2G_i}{g_i}\mathrm{dev}\boldsymbol{E^{ve}} - \frac{1}{g_i}\mathrm{dev}\boldsymbol{q_i} \tag{3.16}$$

$$\mathrm{tr}\dot{\boldsymbol{q}}_{\boldsymbol{i}} = \frac{3K_i}{k_i}\mathrm{tr}\boldsymbol{E^{ve}} - \frac{1}{k_i}\mathrm{tr}\boldsymbol{q_i} \tag{3.17}$$

where the characteristic times for the deviatoric and volumetric parts are g_i and k_i, respectively. The resolution of the system of equations 3.16 and 3.17 is done by simple convolution integrals, leading to the effective Kirchoff stress, defined as:

$$\hat{\boldsymbol{\tau}} = \mathrm{dev}\hat{\boldsymbol{\tau}} + \hat{p}\boldsymbol{I} = \int_{-\infty}^{t}\left[2G(t-s) : \frac{d}{ds}\mathrm{dev}\boldsymbol{E^{ve}} + K(t-s)\frac{d}{ds}\mathrm{tr}\boldsymbol{E^{ve}}\boldsymbol{I}\right]ds \tag{3.18}$$

3.5.3 Viscoplastic part

The non-associated Perzyna-type viscoplastic flow rule is used to define the viscoplastic behavior of glassy polymers:

$$\boldsymbol{D^{vp}} = \frac{1}{\eta}\langle F\rangle^{\frac{1}{s}}\boldsymbol{Q} \tag{3.19}$$

Where $\boldsymbol{D^{vp}}$ is the viscoplastic strain rate defined in eq. 3.12, η is the viscosity parameter, $\langle\bullet\rangle$ are the McAuley brackets, s is the rate sensitivity parameter and $\boldsymbol{Q}$ is the normal to the plastic flow potential P. For this model, the Drucker Prager yield criterion is considered, where the yield function is defined using the combined stress tensor ($\boldsymbol{\phi} = \hat{\boldsymbol{\tau}} - \boldsymbol{b}$):

$$F(\boldsymbol{\phi}) = a_2(\phi_e)^\alpha - a_1\phi_p - a_0 \tag{3.20}$$

$\boldsymbol{b}$ is the corotational backstress tensor, ϕ_e is the von Misses stress, ϕ_p represents the volumetric part of the stress tensor, α is a factor that changes the shape of the yield surface, and when $\alpha = 1$, the yield function adopts the same surface as Drucker Prager. The coefficients a_2, a_1, and a_0 model the yield's surface evolution and are determined from two yielding conditions, in this case, uniaxial compressive (σ_c) and tensile (σ_t) flow stresses, where $m = \frac{\sigma_t}{\sigma_c}$:

$$a_2 = \frac{1}{\sigma_c^\alpha},\ a_1 = 3\frac{m^\alpha - 1}{m+1}\frac{1}{\sigma_c},\ a_0 = \frac{m^\alpha - 1}{m+1} \tag{3.21}$$

Due to the complex viscoplastic behavior of polymers,non-associative Perzyna-type viscoplasticity is considered for this model, as mentioned previously, and the plastic flow is determined by the gradient of the plastic flow potential P instead of by the gradient of the yield function. The viscoplastic flow potential is related to the quadratic dissipation function:

$$P = \phi_e^2 + \beta\phi^2 \tag{3.22}$$

where β is a material parameter related to the plastic Poisson ratio (Melro et al., 2013):

$$\nu_p = \frac{9 - 2\beta}{18 + 2\beta} \tag{3.23}$$

Isotropic hardening law is independently assigned in both compressive and tensile regimes, and the hardening moduli (H_c and H_t) are modeled as linear exponential polynomials:

$$H_c = c_0 + H_c^0 e^{-h_c\gamma} \tag{3.24}$$

$$H_t = t_0 + H_t^0 e^{-h_t\gamma} \tag{3.25}$$

where c_0 and t_0 are the linear hardening parameters, while H_c^0, h_c and H_t^0, h_t define the exponential part of the isotropic hardening law. γ stands for the accumulated plastic strain. These parameters will be identified and calibrated using experimental tests.

3.5.4 Bayesian inference to fit the parameters for the VEVP model

Due to the high number of parameters the finite strain viscoelastic-viscoplastic material model presents, they are identified using the Bayesian Inference (BI) framework presented in the work by L. Wu et al., 2023.

For two continuous random variables $\boldsymbol{A} \in \mathbb{R}^n$ and $\boldsymbol{B} \in \mathbb{R}^m$, where $\boldsymbol{A}$ and $\boldsymbol{B}$ are random vectors with n unknown parameters and m measurements, the Bayesian Inference (BI), based on the Bayes' theorem, is defined as the probability distribution function (π) of the unknown parameters $\boldsymbol{\alpha}$ given $\boldsymbol{\beta}$ observations:

$$\pi(\boldsymbol{\alpha}|\boldsymbol{\beta}) = \frac{\pi(\boldsymbol{\alpha})\pi(\boldsymbol{\beta}|\boldsymbol{\alpha})}{\pi(\boldsymbol{\beta})} \tag{3.26}$$

where $\pi(\boldsymbol{\alpha})$ is the probability distribution function (PDF) that includes prior observations, and $\pi(\boldsymbol{\beta}|\boldsymbol{\alpha})$ is the PDF of the observed $\boldsymbol{\beta}$ given the unknown $\boldsymbol{\alpha}$ parameters.

For the prediction of the parameters of the VEVP material model, the random parameters and observations are divided into two parts: $n, m = [1, 2]$, where 1 is associated to the elastic response ($\boldsymbol{\alpha}_1$ and $\boldsymbol{\beta}_1$), and 2 is associated to the plastic one ($\boldsymbol{\alpha}_2$ and $\boldsymbol{\beta}_2$).

As $\pi(\boldsymbol{\beta})$ is constant due to the already measured observations, for this particular case, BI can be rewritten as:

$$\pi(\boldsymbol{\alpha}_1, \boldsymbol{\alpha}_2|\boldsymbol{\beta}_1, \boldsymbol{\beta}_2) \propto \pi(\boldsymbol{\beta}_2|\boldsymbol{\alpha}_1, \boldsymbol{\alpha}_2)\pi(\boldsymbol{\alpha}_2)\pi(\boldsymbol{\alpha}_1|\boldsymbol{\beta}_1) \tag{3.27}$$

The experimental data consists here in the uniaxial stress response Σ for a monotonic applied strain (ε) at a given strain rate $\dot{\varepsilon}$. The VEVP model provides the First Piola Kirchoff stress (σ_{eng}) as a function of current strain ε, strain rate $\dot{\varepsilon}$ and time t for a given set of material parameters $\boldsymbol{\vartheta}$. For fitting the model, error-based BI is considered, and the relation between the stress measurement Σ and the model response for uniaxial monotonic loading is expressed as,

$$\Sigma = \sigma_{eng} + \omega_\Sigma = \Phi(\varepsilon, \dot{\varepsilon}, t, \boldsymbol{\vartheta}) + \omega_\Sigma \tag{3.28}$$

where ω_Σ is the stress noise that follows a Gaussian distribution $\mathcal{N}(x|0, s_\Sigma^2)$.

Using the theory of conditional independence and assuming each experimental test is independent of the others, the likelihood function of the conditional distribution of measured stress is defined as:

$$\pi(\boldsymbol{\Sigma}|\boldsymbol{\varepsilon}, \dot{\boldsymbol{\varepsilon}}, \boldsymbol{t}, \boldsymbol{\vartheta}) = \prod_{i=1}^{N_\beta} \mathcal{N}(\Sigma_i - \Phi(\varepsilon_i, \dot{\varepsilon}_i, t_i, \boldsymbol{\vartheta})|0, s_\Sigma^2) \tag{3.29}$$

where N_β is the total number of observations from each type of experimental test with loading conditions which will be explained in section 4 for the bulk material and section 5 for the single struts.

Chapter 4

Multiscale characterization of bulk PA12

The macroscopic material was characterized to analyze its mechanical behavior, develop a material model, and determine the material parameters for multiscale modeling based on experimental data. This was part of the initial steps of both this work and the European project MOAMMM, mentioned in section 1.5.

PA12 macroscopic samples printed in different directions were subjected to uniaxial tensile and compression testing at different strain rates and loading conditions to obtain their tensile, compressive, and relaxation behavior. Shear tests were also conducted on samples with different layer directions to study the shear behavior. The characterization was complemented with DMA and nanoindentation tests to analyze the dynamic behavior and the properties at a local scale.

4.1 Mechanical characterization

4.1.1 Uniaxial tensile tests

Uniaxial tensile tests were performed on PA12 specimens printed in transversal and longitudinal directions on an *INSTRON 5966* universal testing machine equipped with a load cell of 2 kN. The tests were performed on flat specimens of standard dimensions of initial length $L_0 = 113$ mm, width $W_0 = 5$ mm, and thickness $T_0 = 4.1$ mm, at 7.37×10^{-4}, 7.37×10^{-3} and 7.37×10^{-2} s^{-1} strain rates. In addition, force/displacement measurements were taken directly from the machine readings for all strain rates and with Digital Image Correlation (DIC) with the aid of *Vic-2D 2009* software for the lowest strain rates.

The average stress-strain curves represented in Figure 4.1a show an elastoplastic behavior. The material presents an anisotropic response under tensile loads. In the vertical direction, the material deforms plastically up to 18 % before failure, being ductile. In contrast, the material is brittle in the horizontal direction, as it fails with strains below 3.5 %, and test repeatability on the samples with layers in the horizontal direction was very low. This indicates that

the vertical layer direction is the most favorable under tension. It is also observed that the material's strain rate is dependent on the vertical direction, as the yield stress and ultimate tensile stress increase with the strain rate. In contrast, the elongation at fracture (A%) decreases, as observed in Figure 4.1a and Table 4.1.

Table 4.1: Average tensile mechanical properties of PA12 with standard deviation determined following ISO 527-1.

$\dot{\varepsilon}$ [s^{-1}]	Lyr. Dir.	E [GPa]	σ_y [MPa]	UTS [MPa]	A%
7.37×10^{-4}	H	1.4 ± 1	25 ± 1	21 ± 2	3.2 ± 0.4
	V	1.63 ± 0.04	30.2 ± 0.8	43.1 ± 0.7	15 ± 2
7.37×10^{-3}	H	1.47 ± 0.01	24.5 ± 0.3	29.8 ± 0.6	3.0 ± 0.2
	V	1.68 ± 0.05	34.4 ± 0.2	46 ± 1	12 ± 1
7.37×10^{-2}	H	1.55 ± 0.03	27.5 ± 0.3	30 ± 1	2.4 ± 0.1
	V	1.83 ± 0.01	41.6 ± 0.8	49.482 ± 0.006	10.2 ± 0.8

4.1.2 Uniaxial compression tests

Uniaxial compression tests were performed on PA12 specimens printed in both directions at various strains. For low strain rates (2.78×10^{-3}, 2.78×10^{-2} and 2.78×10^{-1} s^{-1}), tests were done on an *INSTRON 3384* universal testing machine equipped with a load cell of 30 kN for PA12; for medium strain rates (1 and 10 s^{-1}), tests were performed on a *Gleeble 3800 GTC*; and for high strain rates (160 to 900 s^{-1}), *Split-Hopkinson pressure bar* tests were performed. For low strain rates, flat specimens of standard dimensions of initial length $L_0 = 30$ mm and a square cross-section of 15 mm per side were used, and for medium and high strain rates, cylindrical specimens of 18 mm height and a diameter of 12 mm were used.

Table 4.2: Average compressive mechanical properties of PA12, determined following ASTM D695-15 for low and medium $\dot{\varepsilon}$. For high $\dot{\varepsilon}$, σ_y was obtained by finding the point with maximum slope change in the σ-ε curves.

$\dot{\varepsilon}$ [s^{-1}]	E [GPa]	σ_y [MPa]
2.78×10^{-3}	1.59 ± 0.01	45.6 ± 0.9
2.78×10^{-2}	1.61 ± 0.02	48 ± 2
2.78×10^{-1}	1.550± 0.004	57 ± 3
1	1.61 ± 0.06	75 ± 3
10	1.77 ± 0.06	82.25 ± 2
166	-	91 ± 2
906	-	100.2 ± 0.6

Stress-strain curves represented in Figure 4.1b show that the material presents an elastoplastic behavior with an irreversible response to deformation. In addition, different behavior between building directions is not appreciated; the material thus presents an isotropic behavior under compression. It is also observed that the material is strain-rate dependent. It can be observed, from Figure 4.1b and Table 4.2, that the yield stress increases with the strain rate, and the

elastic modulus remains constant at low strain rates but starts to increase at medium and high strain rates. In Figure 4.1b, the curve obtained at 10 s^{-1} shows oscillations in the plastic regime, which are produced by the setup vibrations when it is close to its testing limits. In addition, at high strain rates (160 to 900 s^{-1}), the samples are not in stress equilibrium as there are oscillations on the elastic regime (Siviour and Jordan, 2016; Cook et al., 2015). In addition, some oscillations can also be found in the plastic regime due to electronic noise. These oscillations prevent obtaining the elastic modulus, and the yield stress was calculated by finding the stress-strain curves' point with the maximum slope change. In addition, at high strain rates, the curves present the deformation originating from the first impact pulse, which ends before the total deformation of the sample.

4.1.3 Conventional relaxation tests

To study the stress relaxation in the elastic and plastic regimes, simple uniaxial stress relaxation tests were performed on samples of PA12 in both building directions. Some samples were compressed to a maximum strain of 0.02, and others to a maximum strain of 0.3 at (3×10^{-3} s^{-1}) with a holding period of 30 min at those constant maximum strains. These tests were performed to see if the material presented a viscoplastic, viscoelastic, or both responses. The samples' dimensions and machine used are the same as the ones mentioned in section 4.1.2 for low strain rates.

No differences are appreciated between samples built in different directions. In the elastic regime, around 16 % of stress relaxation occurs during the holding period, where 8 % occurs within the first minute (Figure 4.1c). In the Plastic region, around 28 % of stress relaxation occurs during the holding period, where 21 % occurs within the first minute, as observed in Figure 4.1c. The material recovers more stress in the plastic regime than in the elastic as part of the energy is used to deform permanently. This information is important to build the material model.

4.1.4 Single hysteresis loops

Load and unload compression tests were performed on PA12 samples built in both directions to study the behavior when loading and unloading if the material presents different loading and unloading paths. First, the samples were loaded on the elastic regime to a strain of 0.02, unloaded, then loaded again on the plastic regime to a maximum strain of 0.3, and then unloaded at 2.78×10^{-3} s^{-1}. Between load and unloading, there was no holding time. The samples' dimensions and machine used are the same as the ones used for compression at low strain rates.

Figure 4.1d represents the single hysteresis loop stress-strain curves of the samples built in both directions. The same behavior in both building directions is appreciated. There are no indications of hysteresis in the elastic regime, which indicates that the material is linear elastic. In addition, the material shows a viscoplastic response, as it presents a permanent deformation of 22 % when unloaded and a strain recovery of 27 % from the maximum strain. Schob et al., 2020 and Lammens et al., 2017 studies also mention the viscoplastic behaviour of PA12. During unloading on the plastic regime, the material presents a linear region

corresponding to elastic recovery and a non-linear region. The linear region presents a steeper slope than the loading one, an effect caused by viscoelastic relaxation. The non-linear region is a viscoplastic effect that might be caused by kinematic hardening, known as the *Bauschinger effect* (Morelle et al., 2014), which would produce hysteresis by dissipating mechanical energy and accumulating plastic deformation if the material is loaded again (Medeiros et al., 2016).

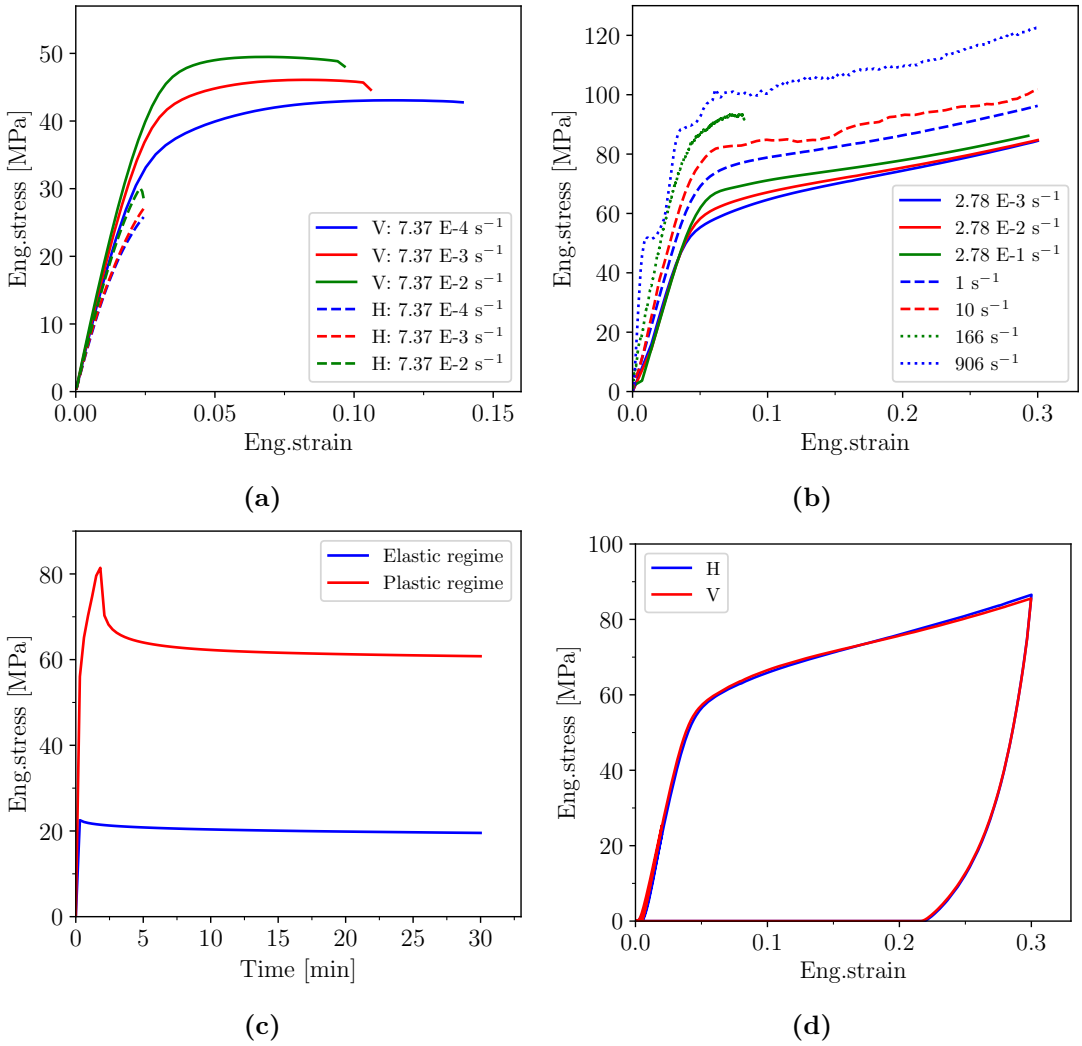

Figure 4.1: Average stress-strain curves of PA12 bulk material of different tests and at different strain rates; (a) tensile σ-ε curves, (b) compressive σ-ε curves, (c) relaxation curves, and (d) single hysteresis curves. The curves have been obtained by calculating the average stress on each strain point of every experimental curve.

4.1.5 Consecutive loading–unloading compression tests

Cyclic compressive tests were performed with PA12 to fit the constitutive material model that is explained later in section 3.5 to obtain the visco-elastic and visco-plastic parameters and analyze the viscous response of the material. The samples were the same used in the compression tests and were tested using an *INSTRON 3384*, equipped with a 30 kN load cell,

at 2.78×10^{-3}, 5.56×10^{-3} and 2.78×10^{-2} s^{-1}. The samples were subjected to 9 cycles. For the first two cycles, the samples were loaded up to 0.5 mm of strain increment to study the elastic region. After the third cycle, the samples were loaded with strain increments of 1 mm per cycle. In each cycle, the samples were unloaded up to 20 N of compressive load.

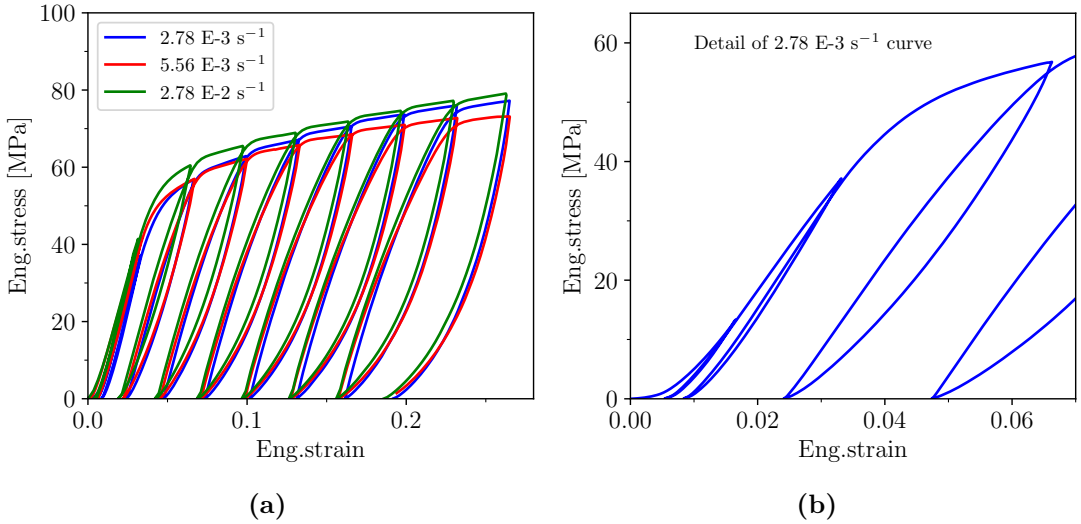

(a) **(b)**

Figure 4.2: Cyclic compressive true stress-strain curves of PA12 (a) at different strain rates and (b) detail of the first cycle.

Figure 4.2 displays the stress-strain curves for PA12 samples under consecutive loading–unloading compression. The first two cycles correspond to the linear elastic region of the material, as the load and unload curves follow the same path, presenting negligible or absence of hysteresis loops, as observed in Figure 4.2b. From the third curve, in the plastic region, the area inside the hysteresis loops increase after each cycle due to an increase in the dissipation effect, which includes the viscous and plastic behaviors, in addition, the linear regions on the loading and unloading paths decrease, which corresponds to a reduction on the elastic response, as seen in Figure 4.2a. The linear region of the loading slope is more shallow than the unloading one, as mentioned in the previous section. Although the loading and unloading paths become less linear after each cycle, the slopes from the linear region remain constant in all the cycles.

4.1.6 Shear tests

Shear tests were performed only on PA12 specimens printed in transverse (XY), perpendicular (XZ), and parallel (YZ) directions (see Figure 4.3) on an *INSTRON 5966* universal testing machine equipped with a load cell of 2 kN at an anvil speed of 2 mm/min, following ASTM 7078M-05 standard. In addition, additional pre-cracks of $\approx$ 1 mm in length and $\approx$ 0.22 mm thick were made on each indentation side of the samples to facilitate the fracture of the specimens. Shear strains were measured with the help of DIC analysis, and the tests were performed until the loading condition was no longer pure shear.

Figure 4.3 shows the shear stress-strain curves of the samples printed in the three directions. Each graph represents the stress-strain curves of 5 samples tested under the same conditions. In

addition, Table 4.3 shows the shear properties, which are calculated following the specifications on the ASTM 7078M-05 standard. XY samples present the best performance, with the highest shear ductility without compromising the strength. For this reason, this layer distribution (XY) is the most favorable.

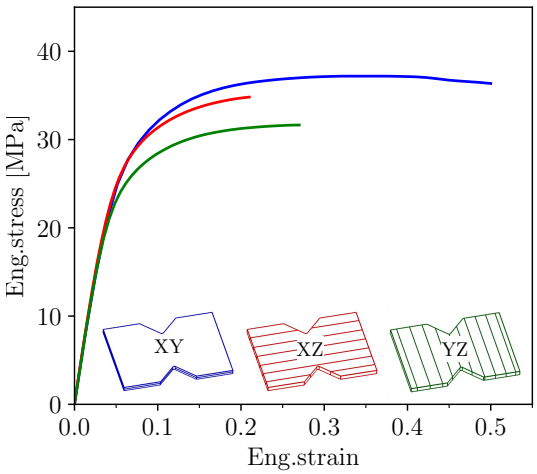

Figure 4.3: Average shear stress-strain curves at different building directions.

On the other hand, YZ samples present the least favorable layer direction for shear loads, as they present the smallest strength values, with shear strength differences of at least 6 MPA lower than the other directions, which varies from 24 to 16 MPa and 31 to 38 MPa of offset and ultimate shear strengths respectively. On the other hand, the elastic modulus is almost the same in all building directions, with an average value of 0.58 GPa. This value is very close to the expected value, 0.57 GPa, obtained from the equation that relates the elastic modulus with the shear modulus and Poisson's ratio.

Table 4.3: Average shear properties of PA12 with standard deviation, determined following ASTM 7078M-05 standard. Offset and ultimate shear strength are τ_y and τ_u, respectively.

Lyr. Dir.	**G [GPa]**	$\boldsymbol{\tau_y}$ **[MPa]**	$\boldsymbol{\tau_u}$ **[MPa]**
XY	0.54 ± 0.02	24 ± 3	38 ± 2
XZ	0.59 ± 0.0	22 ± 4	35 ± 3
YZ	0.60 ± 0.0	16 ± 1	31 ± 2

4.1.7 PA12 mechanical behavior at high temperature

Tensile tests were also done at 45 ℃ on an*INSTRON 3384* universal testing machine equipped with an environmental chamber. The strain rate used where the same: 7.37×10^{-4}, 7.37×10^{-3} and 7.37×10^{-2} s^{-1}. Due to the dimensions of the environmental chamber, the samples used for these experiments were the standard ASTM D638 - 03 Type IV samples printed in transversal and longitudinal directions. In addition, DIC was also used.

Compression tests were performed at 45 ℃ too, with the same equipment as the tensile tests,

at 2.78×10^{-3}, 2.78×10^{-2} and 2.78×10^{-1} s^{-1}; the samples used were the cuboid samples of 15x15x30 cm used for compression at low strain rates.

PA12 uniaxial tensile and compression test results are illustrated in Figure 4.4. At 45 ℃ the transition from the elastic to the plastic region is smoother than at room temperature. This indicates that there is an increase in the visco-plastic response with temperature. This behavior is also observed in the DMA analysis, which is explained later (section 4.2), shows the stress-strain curves at different curves and strain rates of compression and tensile on the samples with layers parallel/vertical (V) and perpendicular/horizontal (H) to the applied load. Tensile and compressive mechanical properties can be consulted above, in tables 4.1 and 4.2, whereas the test results at 45 ℃ are shown next.

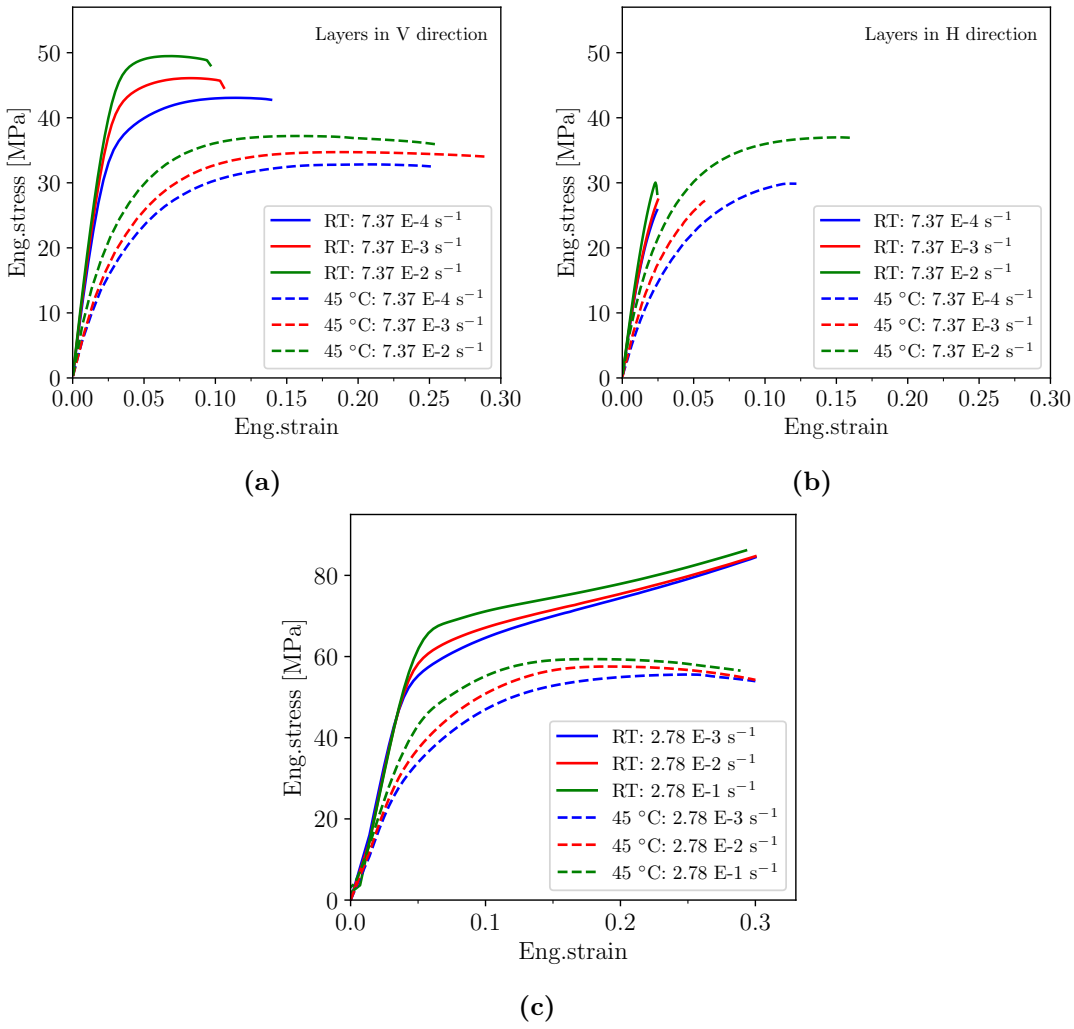

Figure 4.4: Average stress-strain curves of PA12 at 45 ℃ for uniaxial (a) tensile tests on the parallel (V), (b) tensile tests on the perpendicular (H) direction, and (c) compression tests.

Experimental results from tensile tests show a decrease in the elastic modulus and yield stress at 45 ℃. The elastic modulus decreases by 50 % at 45 ℃, approximately from 1.58 GPa at room temperature to 0.74 GPa at 45℃, where 1.58 GPa and 0.74 GPa are calculated as

the average E of all the samples regardless of their layer directions or strain rates. In both directions building (H and V), Young's modulus increases by approximately 0.1 GPa with the strain rate. In addition, temperature and strain rate also influence the yield stress and the ultimate tensile strength (UTS) in both directions but not the elongation at fracture (A%). The yield stress decreases in both directions by around 16 MPa from room temperature to 45 ℃ and increases from 8.7 to 14 MPa when the strain rate increases from 7.37×10^{-4}, to 7.37×10^{-2} s^{-1} at 45 ℃. The UTS decreases in the V direction by 11 MPa when the temperature increases from 33 to 37 MPa with the strain rate. The elongation at break increases in the V direction by at least 12 % from room temperature to 45 ℃. However, contrary to RT behavior, instead of decreasing with the strain rate, it remains constant at around 29 %. Elongation at break increases notoriously in the H direction, where it becomes ductile with an A% of around 15 % at 45 ℃. Table 4.4 shows the tensile mechanical properties at 45 ℃. Regarding the printing direction, the variability of stress-strain behavior of the samples printed in the horizontal direction at 45 ℃ increases compared to the behavior observed at room temperature.

Table 4.4: Average tensile mechanical properties of PA12 at 45 ℃ with standard deviation.

$\dot{\varepsilon}$ $[s^{-1}]$	Lyr. Dir.	E [GPa]	σ_y [MPa]	UTS [MPa]	A%
$\mathbf{7.37 \times 10^{-4}}$	**H**	0.69 ± 0.04	12 ± 1	29 ± 3	16 ± 7
	V	0.74 ± 0.04	14.1 ± 0.3	32.9 ± 0.1	24 ± 4
$\mathbf{7.37 \times 10^{-3}}$	**H**	0.85 ± 0.04	13 ± 2	28 ± 9	13 ± 10
	V	0.87 ± 0.02	14.0 ± 0.4	34.7 ± 0.2	29.5 ± 0.5
$\mathbf{7.37 \times 10^{-2}}$	**H**	0.98 ± 0.08	23.2 ± 2	37 ± 1	20 ± 4
	V	0.86 ± 0.03	23 ± 1	37.2 ± 0.07	35.8 ± 8

Experimental results from compression tests also show a decrease in the elastic modulus and yield stress at 45 ℃. Although the elastic modulus decreases by 30 % at 45 ℃, approximately from 1.58 GPa at room temperature to 0.96 GPa at 45 ℃, its value is constant at all strain rates. On the other hand, the influence of temperature and strain rate on the yield stress is observed, as it decreases by 20 MPa when it is at 45 ℃ and increases from 25 to 38 MPa when the strain rate increases from 2.78×10^{-3} to 2.78×10^{-1} s^{-1}. In Table 4.5, test results at 45 ℃ are shown.

Table 4.5: Average compressive mechanical properties of PA12 at 45 ℃ with standard deviation.

$\dot{\varepsilon}$ $[s^{-1}]$	E [GPa]	σ_y [MPa]
$\mathbf{2.78 \times 10^{-3}}$	0.94 ± 0.07	25 ± 3
$\mathbf{2.78 \times 10^{-2}}$	0.98 ± 0.03	28 ± 1
$\mathbf{2.78 \times 10^{-1}}$	0.96 ± 0.02	38 ± 1

4.1.8 Mechanical behavior of aged PA12

To see how PA12 properties change with time, an aging study was done on the remaining samples used for the previous tests. Table 4.6 shows a summary of the remaining sample

types, printing dates, and the time passed between printing and testing all the samples within the batch, regardless of whether they are aged or not. As mentioned in Chapter 2.2.2, the samples were printed in batches. The samples used for the aging analysis belong to two different batches with different fabrication dates: batch 1 was printed in September 2020, and batch 2 was printed almost half a year later, in January 2022. After the samples were fabricated, they were tested within 2 months maximum, and the remaining ones from batches 1 and 2 were tested around 41 and 22 months later, respectively. During that time, the samples were stored at room temperature and in a dry environment.

Table 4.6: Table showing the batches used for the aging study, their fabrication date, testing dates, and the time passed between fabrication and testing.

Type	**Batch**	**Fabrication date**	**Testing date**	**Time [months]**
Tensile	1	18-09-2020	05-11-2020	1.6
	2	31-01-2022	21-11-2023	22.0
	1	18-09-2020	26-02-2024	41 only V
Compression	1	18-09-2020	06-11-2020	1.6
	2	31-01-2022	04-12-2023	22.4
	1	18-09-2020	—	No samples
DSC	1	18-09-2020	26-02-2024	41
DMA	1	18-09-2020	16-11-2020	2
	1	18-09-2020	22-02-2024	41

The tensile samples were tested under the same conditions as the tensile tests carried out before, and the same machine was used. The rectangular compression samples were tested in the same machine and testing conditions as the samples tested at low strain rates. The DMA and DSC samples testing conditions, results, and discussion are explained later, in sections 4.2 and 5.2.3.2, respectively.

Table 4.7: Comparison of average compressive properties, with standard deviation, between non-aged and aged samples. Values obtained from compressive $\sigma - \varepsilon$ curves.

Batch	**1**		**2**	
Tested after	**1.6 mo**		**22.4 mo**	
$\dot{\varepsilon}$ $[s^{-}1]$	**E [GPa]**	$\boldsymbol{\sigma_y}$ **[MPa]**	**E [GPa]**	$\boldsymbol{\sigma_y}$ **[MPa]**
$\mathbf{2.78 \times 10^{-3}}$	1.59 ± 0.01	45.6 ± 0.9	1.45 ± 0.02	44.7 ± 0.5
$\mathbf{2.78 \times 10^{-2}}$	1.61 ± 0.02	48 ± 2	1.50 ± 0.02	50.6 ± 0.9
$\mathbf{2.78 \times 10^{-1}}$	1.55 ± 0.004	57 ± 3	1.43 ± 0.02	54 ± 1

Table 4.7 compares the compressive properties, elastic modulus, and yield stress of non-aged and aged samples. The values for the non-aged samples are the same as those in Table 4.2. Since the aged values closely match the non-aged ones, there is no observable trend or change in properties between the non-aged and aged samples. This phenomenon is primarily due to the comparison of samples from different batches. Regarding tensile properties, the same can

be said about the comparison between the values from batches 1, tested after 1.6 months since fabrication, and 2, tested after 22 months; they are not correlated, as shown in Tables 4.1 and Table 3 in Annex 2 corresponding to samples from batch 2 aged 22 months. Having said that, mechanical properties between aged and non-aged samples are only meaningful between tensile samples from the same batch, as is the case for batch 1, which includes samples tested after 1.6 and 41 months since fabrication.

Table 4.8: Average tensile properties with a standard deviation of aged PA12 after 41 months. 1/41 mo states for batch 1 and 41 months.

Batch	**1 / 41 mo**				
$\dot{\varepsilon}$ $[s^{-1}]$	**Lyr. Dir.**	**E [GPa]**	σ_y **[MPa]**	**UTS [MPa]**	**A%**
7.37×10^{-4}	**H**	–	–	–	–
	V	1.67 ± 0.04	31.2 ± 0.6	44 ± 1	10.8 ± 0.3
7.37×10^{-3}	**H**	–	–	–	–
	V	1.759 ± 0.009	33 ± 1	46.4 ± 4	9.2 ± 0.8
7.37×10^{-2}	**H**	–	–	–	–
	V	1.77 ± 0.06	37.1 ± 0.2	49.4 ± 0.9	8.7 ± 0.2

Table 4.8 shows the average tensile values of elastic modulus, yield stress, ultimate tensile stress, and elongation before fracture for tensile samples aged 41 months and presenting layers parallel/vertical (V) to the applied load (no H tensile samples remained). There were no remaining samples with perpendicular/horizontal (H) for aging, so the analysis is only between V samples. A comparison between the properties of tensile PA12 V samples non-aged and aged is shown in Figures 4.5. Overall, experimental results show a slight increase in the elastic modulus for the aged samples. The elastic modulus increases by approximately 1.4 %, from a total average obtained from the V samples at all strain rates of 1.71 GPa to 1.77 GPa after almost 41 months of aging. Aging also influences the yield stress and especially the elongation at fracture (A%), but not the UTS. The yield stress is the same in non-aged and aged samples at 7.37×10^{-4} s^{-1}, although decreases progressively with the strain rate by around 4 MPa at 7.37×10^{-2} s^{-1}, from 41.6 MPa to 37.1 MPa after 41 months, which means that the material becomes less sensitive to the strain rate (see section 4.1.9. The elongation at break decreases by at least 15 % at high strain rates, and 28 % at 7.37×10^{-4} s^{-1}.

The slight increase in the elastic modulus, a decrease in the strain rate sensitivity, and a significant reduction of the elongation at break indicate that with aging, Polyamide 12 presents a decrease in the viscoplastic effect and becomes stiffer and more brittle. Polyamide 12 is hygroscopic, and its properties degrade with water, as explained in sections 5.2.1 and 2.1 (Paolucci et al., 2020; Seltzer et al., 2011; Touris et al., 2020); however, in this work, the samples were stored in a dry environment, and the aging behavior they present does not correspond to the behavior that could be expected in contact with water or in a very humid environment. Instead, the mechanical behavior observed in the aged PA12 samples can be explained by a typical physical aging process affecting the polymeric microstructure.

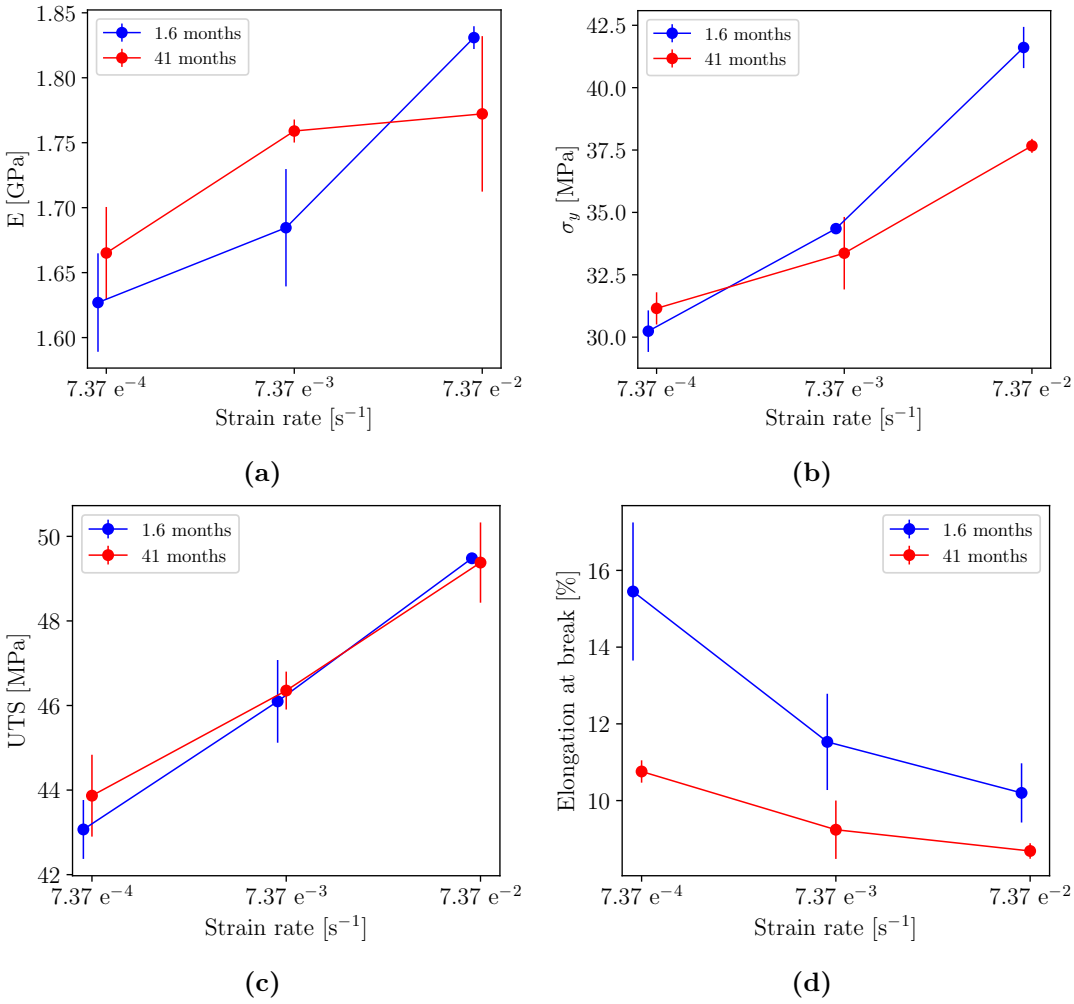

Figure 4.5: Comparison between (a) elastic modulus, (b) yield stress, (c) ultimate tensile stress, and (d) elongation at break of tensile samples from batch 1 tested at room temperature after 1.6 (blue) and 41 (red) months since printed.

After the manufacturing process of polymer components, the material cools down, causing the polymer chains to become immobilized in suboptimal positions. Over time, even at constant temperatures below their glass transition temperature (T_g), the polymer chains gradually move into more favorable positions, resulting in a self-sustaining process of volume reduction and decreased chain mobility. Therefore, the physical aging is expected to cause an increase in the density of polymer components, as well as in their tensile strength, stiffness, and brittleness, consistent with the behavior observed in the aged PA12 samples (Hutchinson, 1995).

4.1.9 Strain Rate Sensitivity of PA12

As mentioned in sections 4.1.1 and 4.1.2, the strain rate influences the yield strength, hardening the material as the strain rate increases. The values of the strain rate sensitivity, obtained from equation 4.1, are shown in Table 4.9, where m is the strain rate sensitivity parameter,

and n is the inverse of the strain rate sensitivity parameter. Figure 4.6 shows the dependence of the yield stress with the strain rate, where blue and red represent compression tests at room temperature of non-aged samples with layers in the horizontal and vertical directions, whereas green and black represent the values from tensile tests at RT of non-aged samples with layers in the horizontal and vertical directions, respectively.

$$m = \frac{\partial \log \sigma_y}{\partial \log \dot{\epsilon}} \quad \text{and} \quad n = \frac{1}{m} \tag{4.1}$$

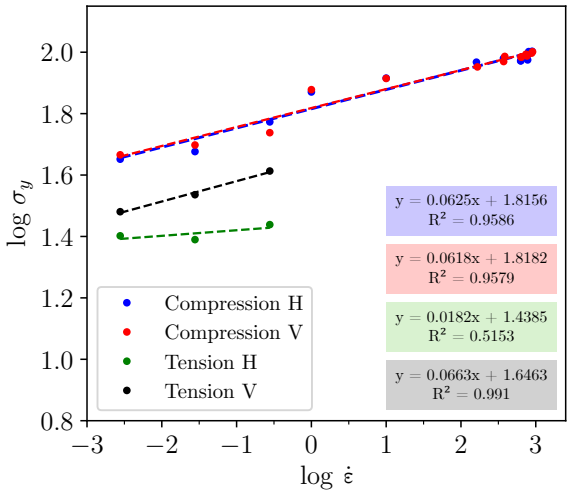

Figure 4.6: Linear regression of the logarithms of tensile and compressive yield stress and strain rate as a function of strain rate of non-aged PA12 tested at room temperature.

At room temperature, non-aged additively-manufactured PA12 presents a moderate strain rate sensitivity in the yield strength, with values around 15-16 and negligible regarding E. The strain rate sensitivity in samples with horizontal layers under tension is around 55 because the material behaves in a brittle manner and exhibits little or no plasticity.

The strain rate sensitivity is higher at 45 ℃ than at room temperature in tension and compression on yield and elastic modulus, as observed in table 4.4. The strain rate sensitivity over the Young modulus was negligible at room temperature. The strain rate sensitivity factor n for the yield point decreases from an average of 15.5 to 10, as observed in 4.9. Note that the strain sensitivity factor is inversely proportional to the strain rate sensitivity as seen in 4.1. In addition, DMA analysis also shows higher strain rate sensitivity at 45 ℃ (see section 4.2.2). An increase in strain rate sensitivity in polymers is associated with the activation of a molecular mobility process (Siviour and Jordan, 2016), which allows the material to respond faster to the applied stresses. At temperatures close to T_g, these mechanisms start to activate, which is the case of PA12 at 45 ℃.

The strain rate sensitivity decreases with age. Aged PA12 at room temperature shows a reduced strain rate sensitivity in comparison to non-aged PA12 at room temperature. The strain rate sensitivity factor increases from an average of 15.5 to values around 24. Contrary to the material subjected at 45 ℃ physically aged PA12 has undergone a self-sustaining

process of volume reduction and decreased chain mobility, allowing molecules to adopt more favorable positions. With reduced chain mobility, the material response to the applied stresses is slower at increasing strain rates, resulting in decreased strain rate sensitivity.

Table 4.9: Strain rate sensitivity factor n of PA12 at room temperature (RT), 45 ℃, and aged 22.4 and 41 months.

Condition	**RT**		**45 ℃**		**Aged 22.4 mo.**		**Aged 41 mo.**	
Lyr. Dir.	H	V	H	V	H	V	H	V
Tension	54.85	15.09	9.80	9.80	-	25.38	-	24.27
Compression	16.00		11.11		23.94		-	

4.2 Dynamic mechanical analysis of PA12

4.2.1 Isofrequency curves

Single cantilever DMA tests were performed at three different frequencies of 1, 3, and 30 Hz in a temperature range from about −100 ℃ to +200 ℃ for PA12 at a heating rate of 0.2 ℃/ min. The storage (E') and tan δ (= E´´/E´) value for non-aged and 41-month-aged PA12 samples as a function of temperature for the three studied frequencies are shown in Figure 4.7.

For non-aged PA12, the glass transition temperature (T_g), which marks the transition from a glassy to a rubbery state as the temperature rises, is approximately 53 ℃ at 3 Hz. This is identified at the maximum peak's position in the tan δ plot (Figure 4.7b). The T_g is influenced by the polymer's degree of crystallinity and is consistent with the values reported for solid nylon (Greco and Nicolais, 1976) and similarly laser-sintered nylon parts (Amel et al., 2014). Notably, there were significant differences in the E' values between the two printing orientations, as observed in Figure 4.7a, with higher values observed in the longitudinal (H) direction (represented by black lines in Figure 2.7). For the H sample, E' is around 1.9 GPa at −110 ℃, decreasing steadily with increasing temperature. On the other hand, the sample printed in the transverse (V) direction shows a maximum E' of about 1.45 GPa, which also decreases with temperature and eventually converges with the E' of the longitudinal sample. Despite these differences, both samples exhibit similar thermal behavior, with α and β relaxations occurring at almost the same temperatures (53 ℃ and −68 ℃, respectively, at 1 Hz). This indicates that the semi-crystalline structure of PA12 and the consistent linear response across the tested strain rates are unaffected by the printing orientation. At higher frequencies, both E' and tan δ values shift slightly higher due to the strain rate dependence of PA12. Similarly, the T_g shifts to slightly higher temperatures, as this transition is related to the onset of long-range cooperative mobility of chain segments in the amorphous phase. At room temperature, the storage modulus is approximately 1290 MPa in the longitudinal direction and about 970 MPa in the transverse direction, highlighting the anisotropic mechanical behavior of the PA12 samples, as revealed by DMA testing.

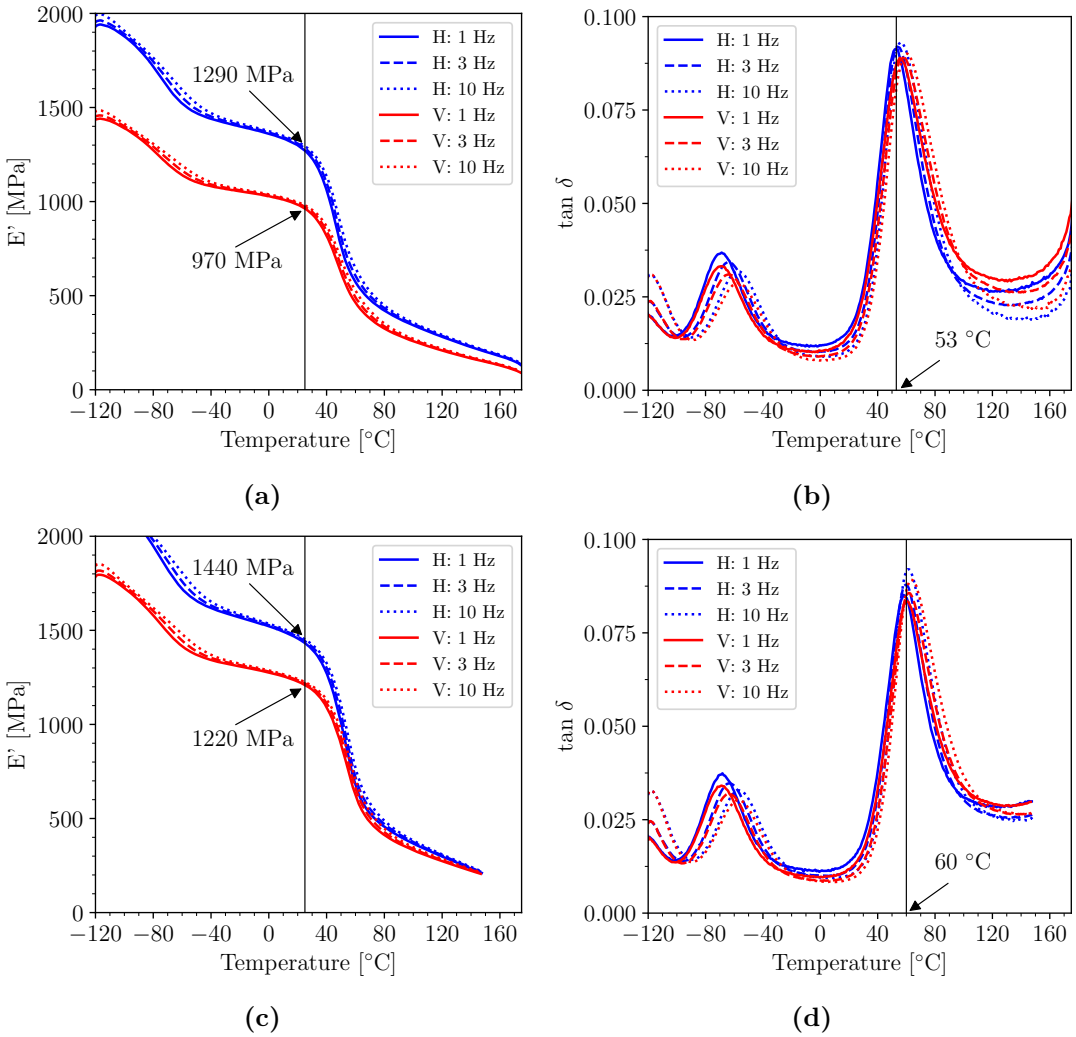

Figure 4.7: Single cantilever DMA experiments at 1, 3, and 10 Hz. Heating rate 2 ℃/min and deflection of 30 µm. (a) Storage modulus and (b) tan δ of non-aged PA12 samples printed with H and V directions. (c) Storage modulus and (d) tan δ of 41 months aged PA12 samples printed on both directions.

On the aged samples, the most notorious changes compared to the non-aged samples are in the T_g and E' values, whereas the tendencies of the curves remain similar. The T_g is shifted to 60 ℃ as Figure 4.7d shows. An increase on the T_g is expected on aged PA12 as the polymer chains, through time, have acquired more stable positions with decreased mobility, as discussed in section 4.1.8. In addition, the aging effects on the stiffness and viscoplastic effect are also reflected in an increase in the storage modulus (E') in both printing directions, maintaining the anisotropy on the mechanical behavior. At −120 ℃ E' increases to 1.84 GPa and 2.2 GPa in the samples with V and H layer directions, respectively, whereas at room temperature, the values increase to 1220 MPa in the transverse direction (V), and 1440 MPa in the longitudinal direction. The behavior observed with DMA analysis is the same as the one observed in section 4.1.8 with uniaxial tensile and compression tests at low strain rates.

4.2.2 Master curves

The analysis was conducted using a frequency sweep at constant temperatures ranging from 1 to 30 Hz, with 10 data points collected per preset temperature. The amplitude was set at 20 µm, and the temperature varied from −130 to 120 ℃, with a heating rate of 2 ℃/min. The master curves were generated using a custom-developed code, applying the time-temperature superposition principle (TTSP) according to the procedure outlined in the work by Rueda-Ruiz, 2021.

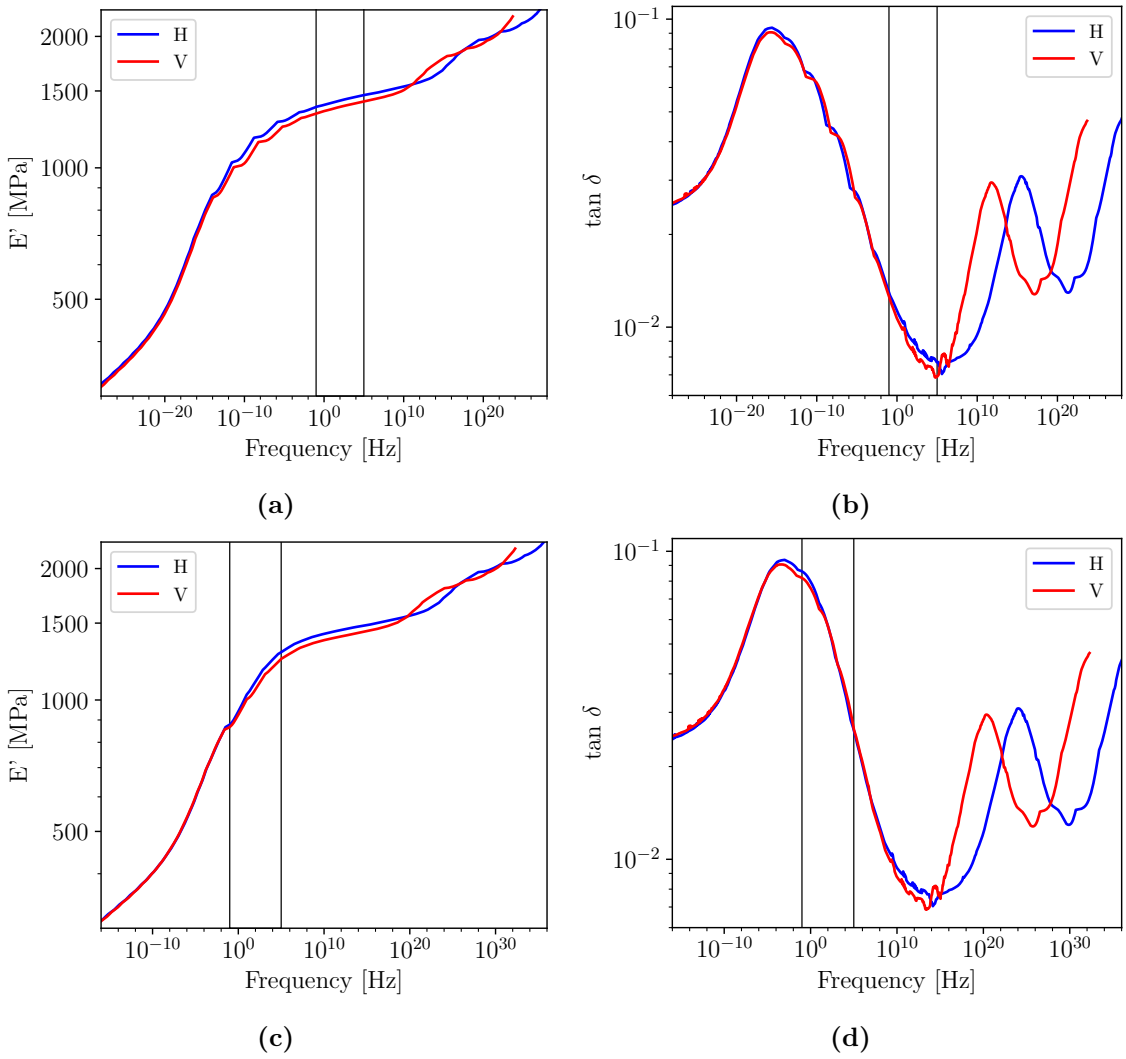

Figure 4.8: Master curves of PA12 samples printed on both directions obtained from single cantilever DMA frequency sweep experiments. Heating rate 2 ℃/min and deflection of 20 µm. Master curves for (a) storage modulus and (b) tan δ at room temperature, and for (c) storage modulus and (d) tan δ at 45 ℃.

Figure 4.8 shows the master curves at room temperature and 45 ℃. The black rectangles indicate the areas whose frequencies are equivalent to the strain rates studied in the compression

tests and have been obtained with the following formula:

$$\dot{\varepsilon} = 2\pi\mathcal{F}\frac{\delta}{L} \tag{4.2}$$

where $\dot{\varepsilon}$ is the strain rate, $\mathcal{F}$ is the frequency, δ is the maximum deflection, and L is the effective sample length in the equipment, which is 17.5 mm.

At both temperatures, the material's elastic behavior dominates over its viscoelastic behavior, as indicated by the storage modulus (E') being about two orders of magnitude greater than the loss modulus (E'/tan δ) and the loss factor (tan δ) remaining below 1. However, at 45 ℃, there is a greater variation in E' and tan δ with frequency, which indicates that the material behavior becomes more strain rate dependent. At 45 ℃, the material dissipates more energy, with E" increasing from around 100 MPa at high frequencies to 120-160 MPa at low frequencies, as tan δ significantly increases (Figures 4.8b and 4.8c), while E' decreases from 1500 MPa at high frequencies to 900-1200 MPa at low frequencies (Figures 4.8a and 4.8c). The viscoelastic behavior is more pronounced at lower frequencies, where the polymer chains have more time to move, whereas, at higher frequencies, the material exhibits more elastic behavior due to the restricted movement of the chains over time.

4.3 Nanoindentation tests for dynamic analysis of PA12 on the macroscopic scale

Conventional quasi-static and nano-impact tests were done to compare the dynamic mechanical properties between the lattices and bulk material.

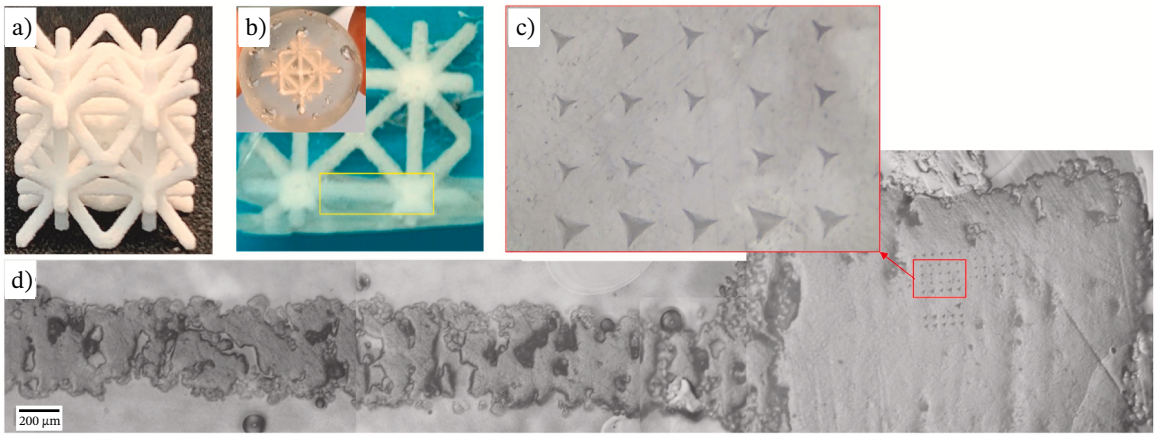

Figure 4.9: (a) SLS printed octet-like lattice structure; (b) Lattice structure embedded in the resin mount; (c) Array of indentation imprints performed at different maximum loads; (d) Optical image of the strut and node surface area enclosed by the yellow rectangle in (b): the location of selected indentations performed in the node area is enclosed within the red rectangle.

For the nanoindentation tests, a printed lattice structure made from PA12 with an octet geometry and a strut diameter of 1 mm (see Figure 4.9a) was embedded in epoxy resin. The

sample's surface was ground and polished with 1 µm diamond paste to reveal a node/strut area and create a smooth surface appropriate for the nanoindentation tests, as depicted in Figure 4.9b. Figure 4.9d shows an enlarged optical image of the area outlined by the yellow rectangle in Figure 4.9b, illustrating that the strut area has significantly higher porosity compared to the node area, where the indentation tests were performed.

Conventional quasi-static nanoindentation tests were performed using a *NanoTest* nanoindentation instrument from *Micro Materials Ltd. (UK)*, equipped with a diamond Berkovich indenter. The tests were conducted with 25 and 50 mN peak loads at three different strain rates: 0.005, 0.05, and 0.5 s^{-1}. An exponential loading scheme was applied for these tests. Each test included a dwell time of 20 seconds at the peak load, followed by unloading at a constant rate of 10 mN/s.

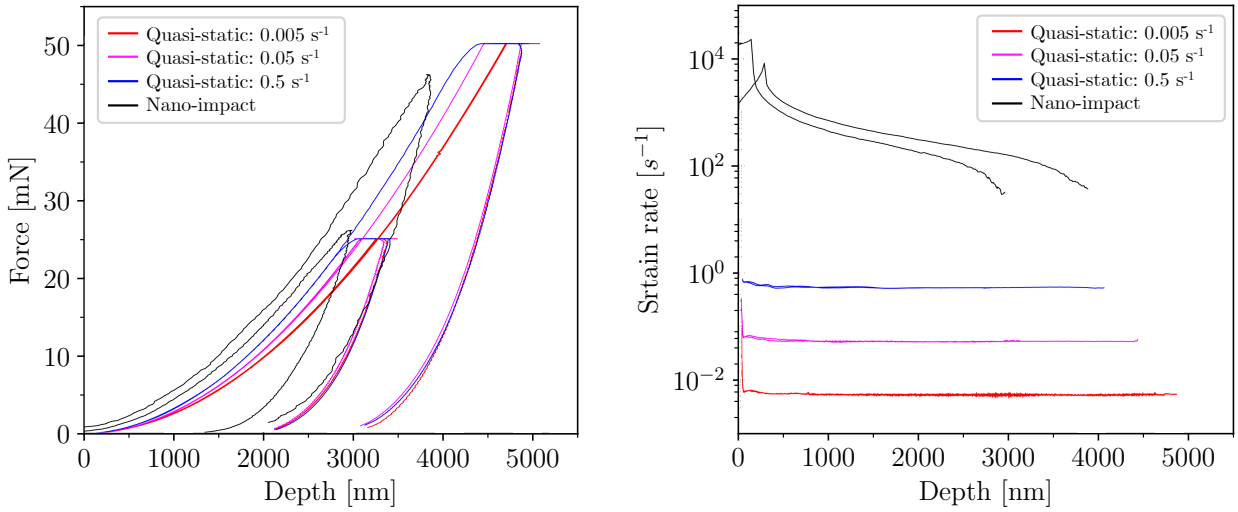

Figure 4.10: a) Force-displacement curves from quasi-static nanoindentation (colored lines) and nano-impact (black lines). Each nano-impact curve corresponds to each of the impact conditions. Higher impulse force leads to higher applied forces and maximum depths. (b) Strain rate signals for quasi-static nanoindentation (colored lines) and nano-impact (black lines) tests.

Load-displacement curves from both quasi-static nanoindentation and nano-impact testing are compared in Figure 4.10. For both methods, the curves were generated by averaging five repetitions for each condition: maximum forces of 25 and 50 mN and strain rates of 0.005, 0.05, and 0.5 s^{-1} for the quasi-static indents, and impulse forces of 2 and 4 mN for the nano-impact indents. The force-displacement curves reflect the strain rate sensitivity of the PA12 material, shown by a decrease in maximum indentation depth with increasing strain rate. This suggests that the material becomes harder at higher strain rates, consistent with the observed increase in yield and flow stresses in macro-scale tests (section 4.1. Additionally, at maximum depth, the quasi-static test curves show the characteristic time-dependent deformation observed in nanoindentation of polymers under constant load (Briscoe et al., 1998), which is attributed to the material's viscoelastic behavior. In contrast, the nano-impact curves do not display this

depth dwell, as the indenter rebounds immediately after impact, whereas in the quasi-static tests, a 20-second hold was introduced before unloading.

Table 4.10: Hardness (H) and indentation modulus (E_r) obtained from the nanoindentation test over a wide range of strain rates. The maximum force (Max. F) in the case of the nano-impact tests is the impulse force applied at a distance of 20 µm resulting in the strain rates shown in Figure 4.10b.

	$\dot{\varepsilon}$ $[s^{-1}]$	Max.F [mN]	H [MPa]	E_r[GPa]
Quasi-static indentation	0.005	25	127 ± 7	2.5±0.1
		50	122 ± 7	2.4 ± 0.1
	0.05	25	144 ± 10	2.5 ± 0.1
		50	137±2	2.5 ± 0.04
	0.5	25	155 ± 5	2.5 ± 0.1
		50	148 ± 3	2.5 ± 0.1
Nano-impact		2	181 ± 11	2.6 ± 0.1
		4	188 ± 17	2.8 ± 0.1

Figure 4.11 shows the apparent hardness distributions for PA12 as a function of depth for the different tests. The apparent hardness increases with the increasing indentation strain rate, as expected. Additionally, the apparent hardness of the nano-impact tests shows a more significant size effect compared to the relatively stable apparent hardness in quasi-static tests. This variation is caused by the progressively decreasing strain rate during the impact tests, as observed in Figure 4.10b.

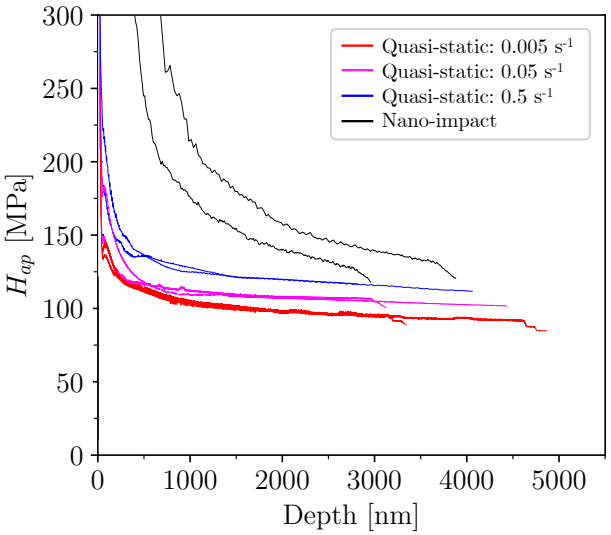

Figure 4.11: Apparent hardness values as a function of indenter penetration depth of quasi-static and nano-impact indentation tests.

The master curves from Rueda-Ruiz, 2021 were used to determine the strain rate sensitivity of the yield stress and the constraint factor linking apparent hardness with the yield stress.

Figure 4.12a depicts the apparent hardness as a function of strain rate for PA12, derived by combining the data from Figures 4.11 and 4.10b. Since the strain rate varies during the nano-impact test, the distribution of apparent hardness was obtained across a range of strain rates, but for simplicity, an average value was used to estimate the yield stress. Figure 4.12b shows the predicted yield stress of PA12 as determined through inverse analysis.

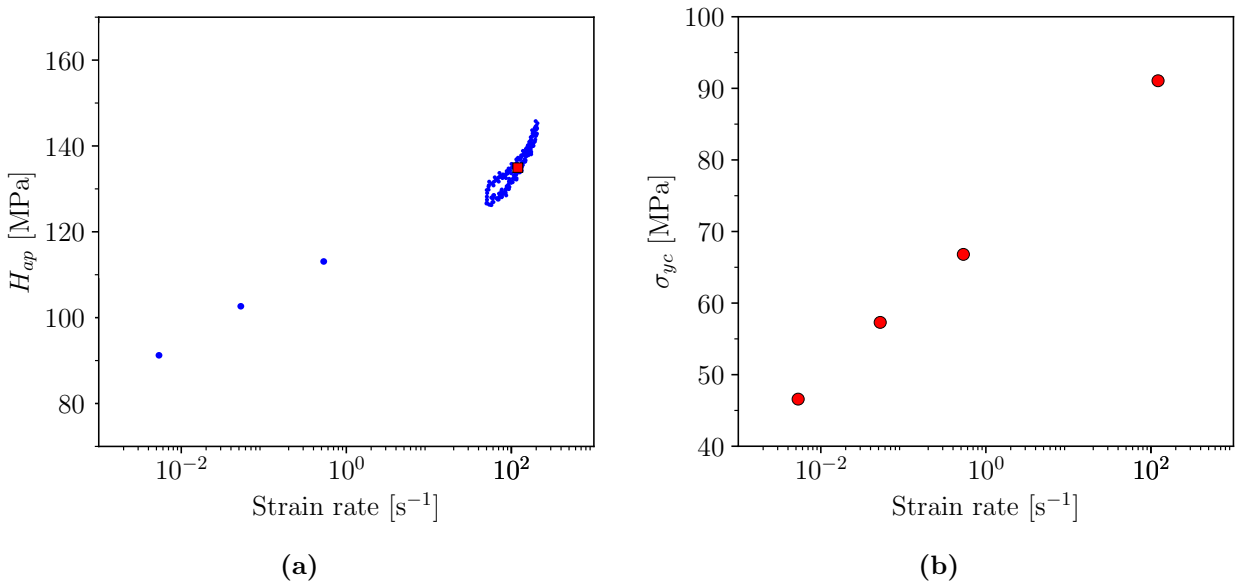

Figure 4.12: a) Apparent hardness as a function of strain rate. The red dot represents the average of the nano-impact values. (b) Compression yield stress was predicted using the inverse analysis in the work Rueda-Ruiz, 2021 and the nanoindentation results.

4.3.1 Comparison between nanoindentation values and macro-scale values

The indentation modulus of approximately 2.5 GPa for low and moderate strain rates obtained in indentation is higher than the values obtained in the macro-scale tests ($\approx$ 1.59 GPa). This is in line with previous reports and has been attributed to the assumption of linear elasticity, when in reality, the polymer is viscoelastic to some degree and, therefore, does not fulfill totally the assumptions of the standard unloading analysis of the nanoindentation curves, which is based on elastic contact mechanics (Hardiman et al., 2017). Moreover, the much lower volume tested in nanoindentation leads to other issues that can affect the measured indentation modulus, such as material homogeneity and skin (size) effects, as generally, there is an increase in the viscosity and modulus at lower depths where the contact is more elastic, which tends to increase the measured modulus (Monclus and Jennett, 2011).

The macro-scale tests performed on the PA12 bulk samples and the micro-scale tests performed on the surface of the PA12 lattice structure both reveal a significant strain rate sensitivity. This is the typical behavior found in polymers, and it is attributed to the characteristic times for activation of the different motions (rotations, chain alignment, etc.) of the molecular chain that constitutes the polymer. The estimations of nanoindentation yield stress values for

PA12 agree very well with those calculated from macro-scale tests. Also, the agreement in the estimations of the strain rate sensitivities is surprisingly good, with a value of $n = 15.36$, very similar to the ones obtained for tensile tests ($n = 15.09$) and compression tests ($n = 16.00$) at room temperature, as seen in Table 4.9 and mentioned in section 4.1.9.

This close correlation of results suggests that there is no size-dependent plastic behavior of the material and should imply that the material properties determined from a bulk sample can be used to model the material behavior of the PA12 polymer printed in a lattice form as long as the lattice contains the same level of porosity as the bulk. However, as mentioned at the beginning of section 4.3, the indentation analysis was done on a node instead of a strut (Figure 4.9d) as the struts had a significant level of porosity. In the case of unit cells and lattices, the node acts as the junction of the struts, but they do not participate in the structural integrity of these metamaterials. In section 5, a size effect was observed in single struts and unit cells as the mechanical properties were diminished for decreasing strut diameters. In addition, tensile tests from single struts showed stiffness values 50 % lower than stiffness values obtained on bulk samples (sections 4.1 and 5).

Chapter 5

Characterization of PA12 on lattices and the microscopic scale

The mechanical characterization of PA12 on the microscale was carried out by doing uniaxial tensile and compression tests at three different microscopic levels: single struts, unit cells, and lattices. Due to the dimensions and geometry of the samples used for each level, single struts were only tensile tested, whereas unit cells and lattices were only subjected to compression testing.

The purpose of these tests was to validate the numerical simulations by comparing them with the experimental data, ensuring that the material model used and parameters obtained from the experimental data of the bulk material predicted the behavior observed in the real tests. In this section, the mechanical behavior of the struts, unit cells, and lattices is compared with the behavior of the macroscopic material to see if there is a size effect between the macroscopic and microscopic scales.

The findings shown in this chapter are written in Cobian et al., 2024. In addition, all the experimental data can be found in the MOAMMM, 2024 online repository.

5.1 Mechanical analysis

5.1.1 BCC lattices

The lattices were printed in two sizes, as shown in Figure 2.5c. The lattices comprise 10 x 10 x 10 BCC unit cells with the geometry observed in Figure 2.5b, without the plates, and constant strut diameters of 0.5 and 1.0 mm for each lattice size. The dimensions of each side of the lattices are 36 mm and 71 mm for the 0.5 and 1.5 mm diameter lattice struts, respectively. The compressive response of the lattices was tested using the same machine and conditions used with the unit cell of the largest dimensions.

The compression tests on the two lattices considered, containing cells with struts of 0.5 and 1 mm of diameter, are shown in Figure 2.5c. Depending on the cell size, the lattices present different behavior. The smaller lattice, composed of 0.5 mm diameter struts, behaves as

linear elastic before failure, reaching strain and stress values of ≈ 3.5 % and ≈ 0.85 MPa, respectively. After failure, there was a sharp decrease in stress, and the lattice started to collapse progressively row by row as the strain increased from 3.5 % to 50 %, which is appreciated as a series of stress peaks in the plateau region on the corresponding stress-strain curve in Figure 5.1a. On the other hand, the lattice with struts of 1.0 mm in diameter presented a linear elastic behavior before catastrophic failure when it reached approximately 7 % of strain and 1 MPa of maximum stress.

In the case of full lattices, the effective Young's modulus of the block was not influenced by its size, being ≈ 36 MPa in both cases.

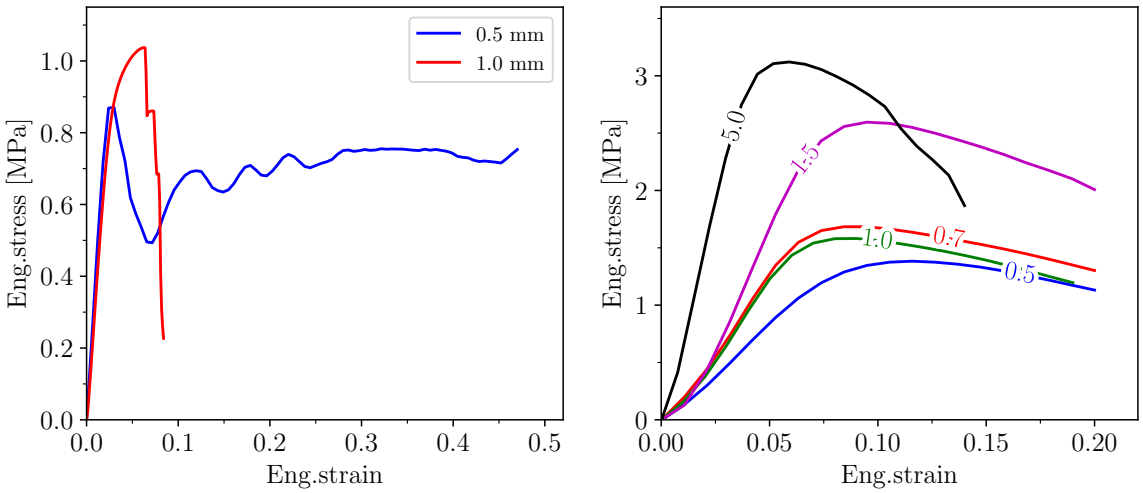

Figure 5.1: (a) Average stress-strain curves at $1.5 \times 10^{-3}\ s^{-1}$ of (a) lattices and (b) unit cells. The labels on the legends for each curve refer to the diameter of the strut in mm.

5.1.2 Unit cells

The unit cells were printed using a body-centered cubic (BCC) geometry in five different sizes, all designed to maintain a constant volume fraction of 0.074 while varying the strut diameters: 0.5, 0.7, 1.0, 1.5, and 5.0 mm for each size. To ensure better control of boundary conditions in both experimental and numerical analyses, two plates were added to opposite faces of the unit cells, as shown in Figure 2.5b. The dimensions of these unit cells are detailed in Table 5.1. The largest unit cell, featuring a 5 mm strut diameter, was produced to study and compare the material properties of the cells across micro and macro scales. Compression tests on the smaller unit cells were conducted using an *INSTRON 5966* machine equipped with a 500 N load cell, while the largest unit cell was tested with an *INSTRON 3384* fitted with a 30 kN load cell. All tests were performed at a strain rate of $1.5 \times 10^{-3}\ s^{-1}$. As mentioned in section 2.2.2, some unit cells were vapor-smoothened to reduce surface roughness. For each size and surface condition (treated and non-treated), five unit cell samples were tested.

Figure 5.1b shows the average engineering stress-strain curves for each unit cell size obtained under compression testing. In the curves, the strain was directly measured as displacement

divided by the initial cell height, and the average engineering stress was obtained as the force divided by the cross-section of the cell. The dimensions of the samples can be consulted in Table 5.1, where the cross-sections are 4.02 x 4.02 mm^2, 6.03 x 6.03 mm^2, 8.04 x 8.04 mm^2, 12.05 x 12.05 mm^2, and 38.80 x 38.80 mm^2.

Table 5.1: Dimensions of unit cell samples.

Unit cell struts diameter	**Dimensions [mm]**
0.5 mm	4.02 x 4.02 x 4.54
0.7 mm	6.03 x 6.03 x 6.80
1.0 mm	8.04 x 8.04 x 9.07
1.5 mm	12.05 x 12.05 x 13.61
5.0 mm	38.80 x 38.8 x 43.80

In the graph, each curve is labeled after the diameter in mm of the struts of the unit cell. All the curves present a linear region and a gradual transition to a non-linear plastic regime until reaching fracture. The stiffness and ultimate compressive strength are directly related to the unit cell size, as shown in Table 5.2, which contains the effective Young's modulus and ultimate compressive strength (UCS) values for the unit cells with different strut diameters. From the smallest to the biggest cell, there is a fourfold increase in the effective Young's modulus from 21 to 84 MPa, while the UCS doubles its value from 1.42 to 3 MPa. The largest unit cell, printed in the macroscopic scale with 5 mm diameter struts, presented a more brittle behavior, failing at approximately 15 % of strain after an accused softening phase, compared to the microscopic scale cells, which sustained a larger softening plastic phase until a final collapse at $\approx$ 20 % strain. The size effects found in tensile strut specimens were very similar to size effects in single unit cells.

Table 5.2: Effective stiffness and ultimate compressive strength of unit cells obtained from compression tests at 1.5×10^{-3} s^{-1}.

	Non-treated		**Surface treated**	
Diameter [mm]	$\boldsymbol{E_{eff}}$ **[MPa]**	**UCS [MPa]**	$\boldsymbol{E_{eff}}$ **[MPa]**	**UCS [MPa]**
0.5	21 ± 2	1.42 ± 0.09	26 ± 3	2.34 ± 0.01
0.7	29.0 ± 0.8	1.69 ± 0.02	31 ± 1	2.00 ± 0.03
1.0	28.8 ± 0.6	1.58 ± 0.02	31 ± 1	1.76 ± 0.01
1.5	44.1 ± 0.5	2.60 ± 0.03	49 ± 2	2.60 ± 0.02
5.0	84 ± 4	3.0 ± 0.2	-	-

Regarding surface roughness, there is only a noticeable difference in the mechanical behavior between the unit cells with 0.5 mm diameter. The effective stiffness difference in these samples is around 20 %, 21 MPa in the non-surface treated and 26 MPa in the vapor smoothened. In addition, the UTS doubles its value on the surface-treated unit cells with 0.5 mm diameter, which increases from 1.42 MPa for the non-treated to 2.34 MPa for the surface-treated. On the rest of the sizes, the mechanical behavior between the non-treated and vapor smoothened becomes gradually negligible as the sample size increases.

5.1.3 Single struts

The tensile response of the struts was characterized using an *INSTRON 5966* equipped with a load cell of 100N. Samples were tested at four different strain rates: 2.78×10^{-3}, 1.67×10^{-2}, 1.67×10^{-1}, and $1.67\ s^{-1}$. The tensile specimens were in the form of cylindrical struts of diameters 0.5, 0.7, 1.0, 1.5 mm, and 5 mm initial length, as shown in Figure 2.5a. As mentioned at the beginning of section 2.2.2, the struts were printed in two sprues to simplify the shipping process. In most of the cases, the struts tested at the highest strain rates, 1.67×10^{-1} and $1.67\ s^{-1}$, were from the second sprue.

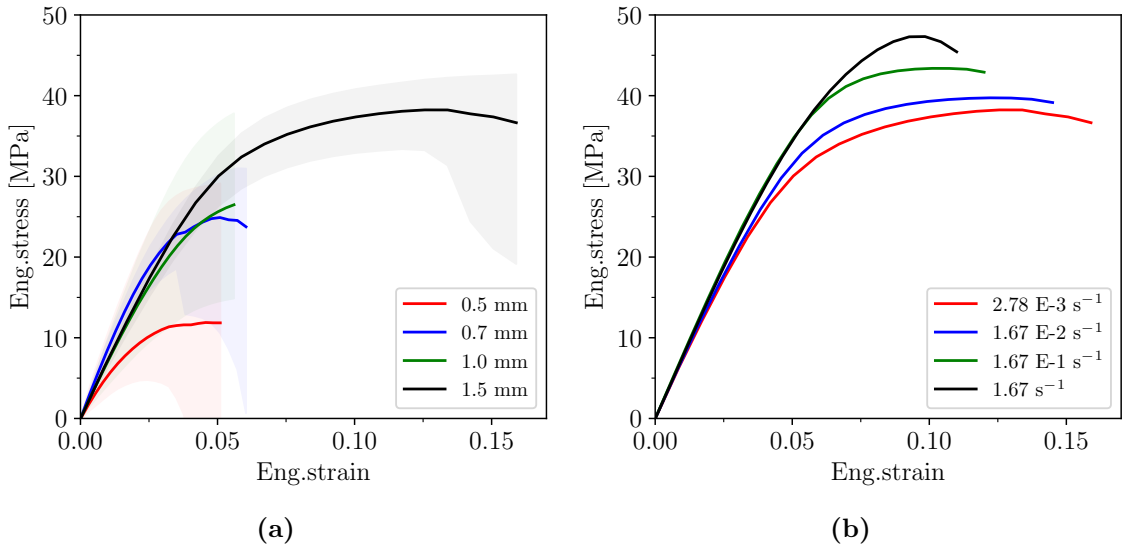

Figure 5.2: Mechanical tests of single struts. a) Average stress-strain curves of single struts at $2.78 \times 10^{-3}\ s^{-1}$ and b) tensile curves at different strain rates of 1.5 mm diameter struts.

The average stress-strain curves obtained from the tensile tests of single struts are represented in Figure 5.2. Each curve in Figure 5.2a represents the average stress-strain curve of the struts with a specific diameter at the lowest strain rate ($2.78 \times 10^{-3}\ s^{-1}$). The average has been calculated considering all the printing directions for each diameter, as there was no correlation between the mechanical behavior and the printing direction within the different specimen sizes. In addition, the grey semi-transparent areas surrounding each curve represent the corresponding dispersion of results obtained for each diameter. A wide dispersion of the mechanical behavior between samples printed with the same diameter can be appreciated. The dispersion is inversely proportional to the strut diameter, with the largest dispersion corresponding to the 0.5 mm diameter struts and the smallest dispersion to the 1.5 mm diameter struts. Within the same dimensions and printing direction, the dispersion is incremented by the specimens of different sprues. The average elastic modulus obtained is in the range of 700 MPa for all the diameters, which is around 50 % lower than the elastic modulus obtained in PA12 on the macroscopic scale (Cobian et al., 2022). In addition, the samples were tested at different strain rates, and, as Figure 5.2b shows, they are strain rate sensitive. The calculated strain rate sensitivity factor n for 1.5 mm struts is around 16, which is in line with the macroscopic PA12 values shown in 4.1.9 (Cobian et al., 2022). However,

due to the dispersion of results within different sprues, it was not reliable to calculate the strain rate sensitivity for the other diameters. Despite the low repetitiveness, a linear and non-linear regime is observed in all the samples.

5.2 Exploring the origins of the size effect in unit cells

In section 5.1, it was noted that the stiffness of the bulk material is 50 % greater than the values observed at the microscopic scale, single struts, and unit cells but not in the lattices. Moreover, in section 5, a size effect is highlighted among struts of varying diameters, whether they are isolated or part of unit cells. In addition, the impact of surface roughness was studied with vapor-smoothened unit cells, and the effects were only notorious on the cells with 0.5 mm diameter struts. Factors contributing to stiffness variations may include porosity, other geometrical features that affect the effective cross-section along the struts, and thermal history during sample fabrication. Additionally, environmental conditions such as humidity can affect the mechanical properties of materials, particularly in hygroscopic polymers like PA12, where a water content exceeding 0.6 % (Touris et al., 2020) degrades its mechanical performance, leading to a deterioration of tensile strength and fracture resistance (Seltzer et al., 2011). Understanding the causes behind the differences in behavior between monolithic (bulk) parts and strut-sized components is crucial for designing lattice-based structures manufactured through 3D printing.

For this reason, in addition to the mechanical characterization, a deeper material characterization was carried out to analyze water content, microstructure, and nanostructure using advanced characterization techniques, namely: thermogravimetric analysis (TGA), differential scanning calorimetry (DSC), scanning electron microscopy (SEM), nanoindentation mapping, X-ray analysis, including X-ray tomography and scattering (WAXS and SAXS). Microstructure refers to the structure that can be observed through microscopy analysis, such as porosity and entrapped or unmelted particles in the samples. In contrast, nanostructure refers to the molecular arrangement of the polymer chains that determine the degree of crystallinity and crystalline phases in the sample material.

5.2.1 Effect of humidity on struts

The effect of humidity on the struts was studied as it could be a possible cause for the difference between the stiffness of bulk and struts. It is well known that PA12 presents water affinity, and its mechanical properties are affected by it (Paolucci et al., 2020; Seltzer et al., 2011; Touris et al., 2020).

The water content of PA12 samples was measured using a *Q50* thermogravimetric analyzer from *TA Instruments*. The thermogravimetric analysis (TGA) was carried out on pieces belonging to a macroscopic sample and a 0.7 mm single strut. The pieces were heated up to 900 ℃ at 10 ℃/min. The water content percentage was calculated as the weight loss up to 150ºC, a temperature where water has already evaporated.

Weight loss as a function of temperature on both macroscopic samples and struts can be observed in Figure 5.3. The blue curve represents the weight percentage as a function of

temperature, whereas the red curve represents the first derivative of the weight percentage with respect to temperature.

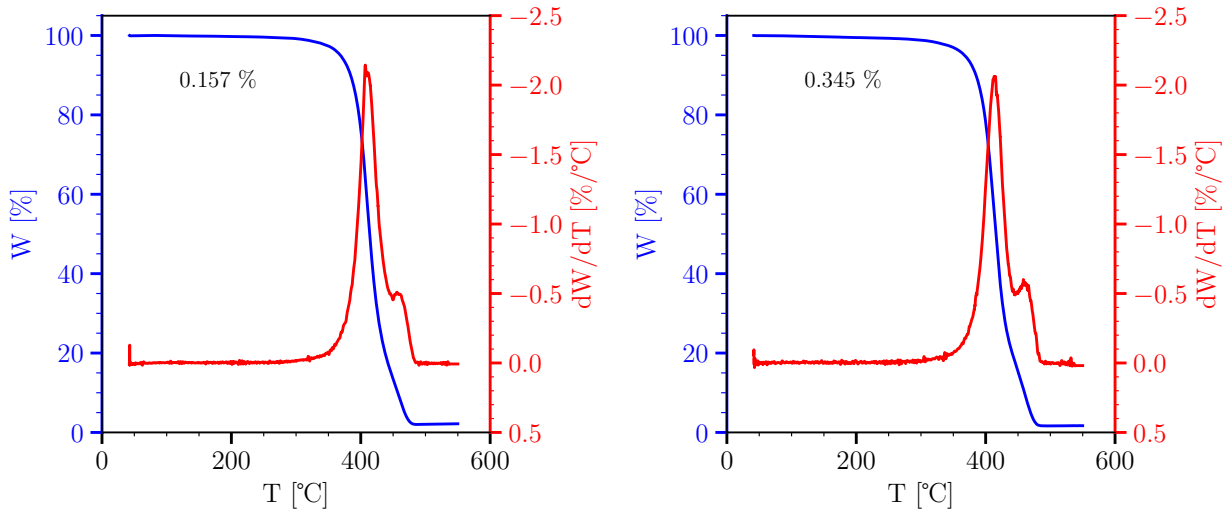

(a) **(b)**

Figure 5.3: Weight loss and second derivative curves obtained from TGA analysis for (a) bulk sample and (b) 0.7 mm diameter strut. The percentage values shown in each graph correspond to the water content in each sample.

Water content percentage was calculated as the weight loss up to 150 °C. The macroscopic samples contain 0.157 % of water, corresponding to the water content of PA12 in dry conditions (Seltzer et al., 2011). On the other hand, struts contain 0.345 % of water. In addition, the first derivatives show only a peak at 420 °C, indicating material degradation at that temperature, but no indications of water content in the material, as the curve is flat up to 350 °C. The work by Touris et al., 2020 reported that 0.6 % of water intake is detrimental to the mechanical properties of PA12. Paolucci et al., 2020 mentioned that during testing, the samples may lose water. In addition, Touris et al., 2020 reported that the material loses moisture quickly at room temperature and also the effects produced by water. In this work, the water intake difference between the macroscopic material and the strut is less than 0.2 %; the higher absorbed water content on the struts is probably due to their larger surface/volume ratio due to their cylindrical geometry and porosity. Nonetheless, the struts were only exposed to a dry environment, like the macroscopic material, and the water content is still insignificant and plays no role in reducing the elastic modulus of PA12 when it is used to print samples on the microscale.

5.2.2 Effect of surface roughness and porosity

After seeing that water has no effect on the mechanical properties of PA12, the first hypothesis for a size effect of the type "the *smaller, the weaker/softer*" is an increase of porosity and surface roughness for decreasing strut diameters or, at least, a higher influence of these features on the cell response.

Experimentally, the topology of the samples was analyzed with SEM imaging of struts extracted from the different samples. The porosity and internal defects of 3D-printed single struts and unit cells were characterized with X-ray tomography.

To quantitatively determine the influence of these features, the actual microstructure maps of the as-printed cells and struts with different sizes acquired by X-ray tomography were used in direct numerical simulations. In particular, FFT-based simulations were performed using the voxelized tomographies of the as-printed unit cells as Representative Volume Elements.

5.2.2.1 Scanning electron microscopy

All the sample surfaces, including struts from unit cells (non-treated and treated) and lattices, were analyzed using the scanning electron microscope (SEM) *Apreo 25 LoVac*. The surface morphology of the struts from the lattices was analyzed at two different locations of the lattice by observing struts taken from the outer part (edges) and inner part (center) of the lattice.

Figure 5.4 shows SEM images of two unit cells with 1 mm diameter struts, non-surface treated and treated. In addition, Figure 5.4 also shows 1 mm diameter struts from the 10x10x10 lattice. Overall, a rough surface is clearly observed in all the non-surface treated samples: single struts, unit cells, and lattices.

Four emerging struts from the central node of non-treated and surface-treated unit cells with 1 mm diameter struts can be compared in Figures 5.4a and 5.4b, respectively. On surface-treated unit cells, the surface roughness was erased entirely due to the vapor smoothing treatment. However, the characteristic layer discontinuity of additively manufactured parts is slightly noticeable on the struts as periodic wrinkles along the struts.

From the 1 mm diameter struts from the 10x10x10 lattice, one of them was extracted from the center of the lattice (Figure 5.4c), whereas the other was extracted from the perimeter of the lattice (Figure 5.4d). Figures 5.4e and 5.4f show higher magnification images of the edge and center struts' surface, respectively. The appearance of the single and unit cell struts is like the one observed on the perimeter lattice struts, shown in Figures 5.4d and 5.4f.

The rough surface results from the presence of powder particles that were partially sintered during the printing process. In addition, very small SiC particles were observed in all samples, which are residual particles left over by the sandblasting process and not removed after the cleaning process. In Figure 5.4f, SiC particles are observed as small white dots uniformly distributed over the surface of the samples. These SiC particles act as small projectiles that deform and fuse the PA12 powder grains exposed on the surface of the samples, as observed in the edge strut surface in Figure 5.4d. As mentioned at the end of section 2.2.2, the lattices contained leftover powder entrapped in the center, especially the ones with 0.5 mm diameter struts; sometimes, powder particles need to be removed manually as the sandblasting with SiC particles cannot reach the central part of the lattice, depending in the lattice dimensions. Therefore, much fewer SiC particles were found in the central part of the lattice (Figure 5.4e) than in the outer part (Figure 5.4f). In addition, the struts in the center present a diameter ≈ 50 % larger than the outer struts, which is close to the design value of 1 mm, as observed in Figures 5.4d. Therefore, the surface of the central struts was slightly affected by the SiC projectiles during sandblasting. Since the entrapped powder gets partially sintered

and attaches to the surface, the resulting diameter increases. In the 0.5 mm-diameter strut lattice, the sandblasting effect is more notorious than in the other lattice type. The outer struts had the characteristic color of over-sandblasted components, whereas the interior of the lattice was full of entrapped loose powder.

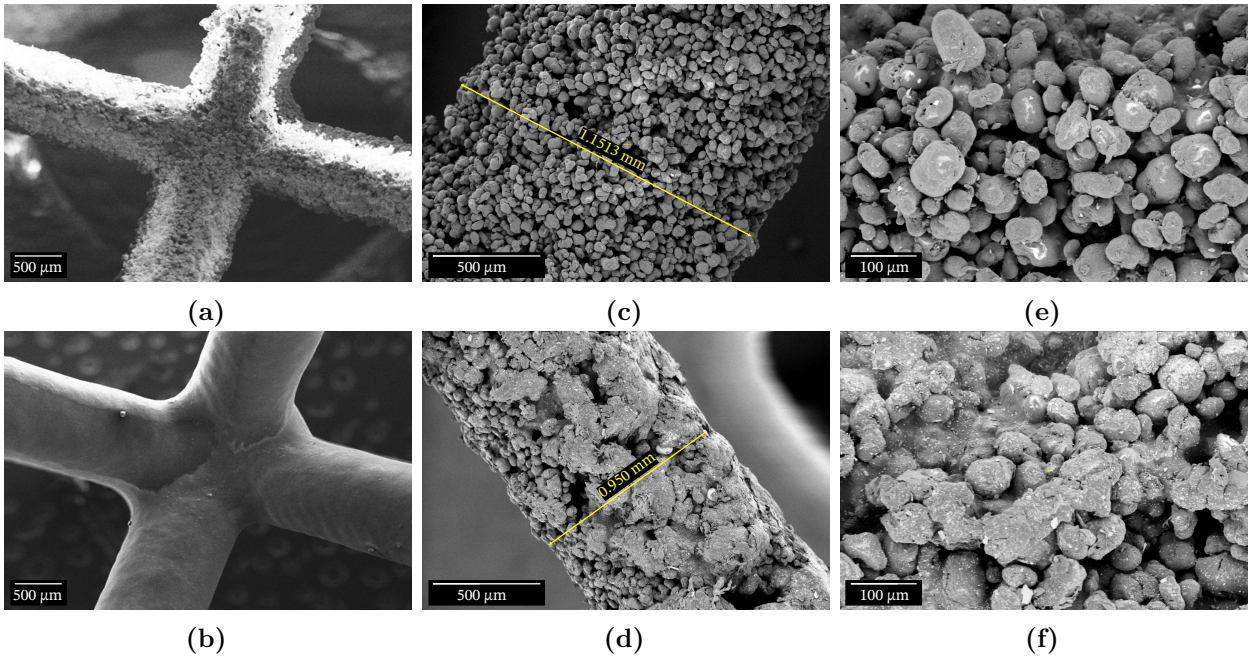

Figure 5.4: SEM images of 1mm diameter unit cells and lattice struts. (a) Non-treated unit cell, (b) surface-treated unit cell, (c) strut from the center of the lattice, (d) strut from the edge of the lattice, (e) magnification of the central strut, and (f) magnification of the perimeter strut.

5.2.2.2 X-ray tomography

Experimental set up and experiments

The architecture and internal defects of single struts and BCC unit cells were analyzed with X-ray tomography. The struts of different diameters were characterized at the *MatéIS* facilities in INSA Lyon, France. The samples were scanned using an *RX Solutions EasyTom Nano* with a resolution of 4 µm, and the tomograph was operated at a voltage of 80 kV and an intensity of 100 µA. The unit cells with diameters from 0.5 to 1.5 mm were scanned at *IMDEA Materials* facilities with a *GE (Phoenix) Nanotom 160 kV* working at 60 kV and 200 µA. No filter was used to reduce the beam hardening. Each unit cell sample size was scanned at a different resolution, as shown in Table 5.3.

Porosity characterization

The criteria explained in section 2.7.1 were followed to analyze the defects on the printed samples. In addition, internal and virtual porosities were calculated globally (P_{ig}, P_{vg}), through the whole image stack, and locally in two individual slices (P_{il1}, P_{il2}, P_{vl1}, P_{vl2}) to

see if the porosity was uniformly distributed. In the struts, the slices were chosen randomly, whereas in the unit cells, a slice after the plate and the slice at the center of symmetry of the geometry, which contains the central node, were used. Tables 5.5 and 5.6 show the porosity results and will be explained later in this section.

Table 5.3: X-Ray tomography scan resolution for each type of sample.

Sample	Diameter [mm]	Raw vol. res. [µm/px]	RVE res. [µm/px]
Strut	all	4.0	36.3
Unit cells	0.5	2.7	16.9
	0.7	4.0	25.0
	1.0	5.4	33.6
	1.5	8.0	50.0

Figure 5.5 shows a selection of cross-section images taken with X-ray tomography from single struts with diameters of 0.7, 1.0, and 1.5 mm, unit cells with struts of 0.5, 0.7, 1.0, and 1.5 mm diameter. The images have been thresholded and converted into binary to enhance the contrast between material and voids. Slices from the tomography showing the interior longitudinal cross-section of each strut are shown in Figure 5.5a, and the central part of reconstructed volumes of unit cells are shown in Figure 5.5b. Surface roughness and internal pores are the main types of defects observed by X-ray tomography. Surface roughness is appreciated as protuberances and cavities due to inappropriate powder sintering during 3D printing (Flodberg et al., 2018). Surface roughness becomes less notorious for the struts with a larger diameter in both single struts and unit cells. With vapor smoothing, the surface roughness is eliminated, as observed in 5.5b; however, the internal porosity remains. The measured strut diameter is in the theoretical diameter range. However, depending on the printing direction, sample geometry, and size, the measured diameter can deviate up to 15 % from the theoretical value as observed in Table 5.4. The samples printed with layers in the horizontal direction (denoted by H) present the largest diameter, while those printed with oblique layers (denoted by T) present the lowest diameter. The strut diameters were accurately measured only on single struts, as the geometry and tomographic processing were more straightforward than in the BCC unit cells. On the other hand, the strut diameters on the unit cells were, in general, 15 % larger than the as-designed one.

The pores are irregularly shaped and mostly appear isolated with an average diameter of ≈ 32 µm regardless of the strut diameter dimension. Some pores also appear joined to other pores, forming elongated cavities of more than 0.5 mm long, creating discontinuities between the printed layers of the unit cells. As the average pore size is almost constant in all samples, the specimens containing the smallest diameter present the most significant defect size/diameter ratio. In Figure 5.5b, in the smallest unit cell, it is observed how discontinuous the vertical struts are due to the layer printing direction and defect size. In the medium-sized unit cells (0.7 and 1.0 mm), the elongated discontinuities that correspond to interfaces between layers are clearly visible.

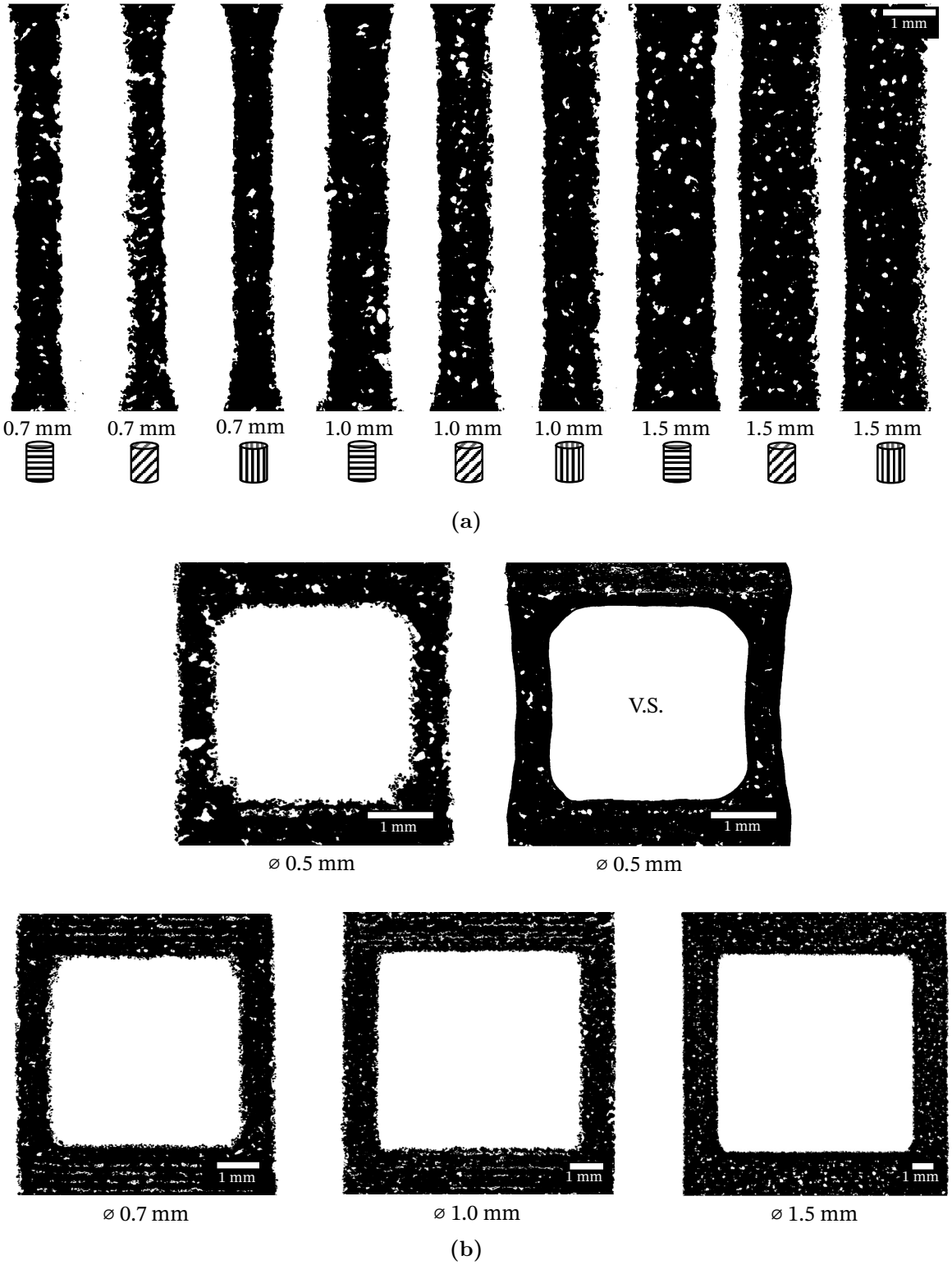

Figure 5.5: Thresholded longitudinal cross-sections from X-ray tomography. (a) single struts with different printing directions and diameters (0.7 - 1.5 mm), where the cylinder drawings at the bottom indicate the layer direction deposited in horizontal (H), vertical (V), and oblique (T), (b) unit cells with strut diameters of 0.5 - 1.5 mm. V.S. refers to vapor smoothing.

Tables 5.5 and 5.6 show the values of porosity calculated following the criterion explained previously. The virtual porosities relate the as-designed and as-printed volumes (P_{vg}) or cross sections (P_{vl1}, P_{vl2}). In contrast, the internal porosities compare the as-printed sample volume (P_{ig}) or cross-sections (P_{il1}, P_{il2}) with as-printed samples with artificially removed internal porosity.

Table 5.4: Comparison of theoretical and measured diameters from single struts, where H, V, and T represent the layer directions perpendicular, parallel, and oblique to the strut length, respectively. Measurements of struts from unit cells were not possible.

Theoretical diameter [mm]	**Measured diameter [mm]**		
	H	**T**	**V**
0.70	0.82	0.70	0.75
1.00	1.06	0.98	0.98
1.50	1.50	1.41	1.49

From Table 5.5, two tendencies are observed. The struts printed with layers in the oblique direction (T) present the lowest volume among the struts with layers in the three directions, as the virtual global porosity (P_{vg}) in all the T cases is close to 15 %. This means that the volume of the as-designed sample is 15 % larger than the as-printed one in that direction. This is related to the information from Table 5.4, where it was observed that the struts with the layers in the oblique direction presented the lowest as-printed diameters compared to the theoretical ones. The second tendency observed among the struts of different diameters is that the volumes of the as-printed samples become closer to the as-designed one as the diameter increases, where the closest volume corresponds to the 1.5 mm diameter strut with H layer, with a volume 4 % smaller than the as-designed one. In addition, as the strut diameter becomes smaller, the printed volume can be up to 25 % larger than the as-designed one due to the inappropriate powder sintering during fabrication that contributes to the notorious surface roughness in the samples with the smallest diameters. In Table 5.6, P_{vg} also shows the same tendency in the BCC unit cells where the printed volume is bigger in the unit cells with smaller diameters, up to 31 % larger in the case of the 0.7 mm diameter unit cell volume, whereas in the samples with larger strut diameters, the printed volume is closer to the as-designed one, reaching to a minor difference of 2 % in the case of the unit cell with 1.0 mm strut diameters. Moreover, the printed material is not uniformly distributed, as the virtual local results are not similar in most of the cases, especially in the samples with small strut diameters.

Although the volume difference is significant in samples with struts diameters below 1.0 mm, internal porosity P_{ig} has an average value of $\approx$ 3.2 % in all samples, and it is homogeneously distributed, as the local internal porosities present similar values. Still, as the strut diameter decreases, porosity distribution becomes more uneven.

The porosity results from tables 5.5 and 5.6 indicates that the printing resolution for a 1 mm strut diameter starts to be an adequate size for the machine's resolution. According to the 3D printer *EOS FORMIGA P100* specifications, the struts' diameter dimensions are very small and close to the machine's resolution. The AM machine is calibrated to optimally print macroscopic parts of 2 - 5 cm at minimum, limiting the machine parameters for the

Table 5.5: Porosity from single struts calculated from tomographies.

	Single struts								
Strut diameter [mm]	**0.7**			**1.0**			**1.5**		
Porosity	**H**	**T**	**V**	**H**	**T**	**V**	**H**	**T**	**V**
P_{vg} [%]	- 25	12	-12	- 10	13	11	4	15	6
P_{vl1} [%]	- 30	- 2	- 11	- 7	9	11	4	18	3
P_{vl2} [%]	- 26	4	- 23	6	7	9	7	15	3
P_{ig} [%]	2	2	2	2	3	3	4	4	4
P_{il1} [%]	> 1	> 1	7	1	4	1	3	3	6
P_{il2} [%]	1	1	4	6	4	2	3	2	2

Table 5.6: Porosity of unit cells calculated from tomographies. V.S. refers to vapor smoothing and NON to non-surface treated.

	Unit cells				
Strut diameter [mm]	**0.5**		**0.7**	**1.0**	**1.5**
Porosity	**V.S.**	**NON**	**NON**	**NON**	**NON**
P_{vg} [%]	- 19	- 13	-31	2	- 8
P_{vl1} [%]	- 22	- 21	-22	6	- 5
P_{vl2} [%]	- 26	-31	-25	1	- 9
P_{ig} [%]	3	4	4	4	2
P_{il1} [%]	5	3	3	4	2
P_{il2} [%]	8	2	5	6	2

lattice magnitudes. The laser beam has a diameter of 0.4 mm, and although the printing machine automatically compensates the laser beam, the calculations are inaccurate. In addition, the powder diameter is around 50 µm, and even with the laser compensations, the wall temperature of the struts is high, and the extra powder gets attached to the struts, increasing the average diameter and producing surface roughness. It can also be observed that imperfections are related to the decreasing diameter of the struts, which is an indication of the limited resolution of the machine when printing very small diameters (Flodberg et al., 2018).

5.2.2.3 Numerical analysis of unit cells and lattices

Uniaxial compression tests were simulated to study the mechanical response of the voxelized tomographic and CAD volumes of unit cells and lattices. Attention was focused on the elastic behavior with the aim of analyzing if the porosity and roughness distribution reduces the load-carrying capacity of the cell struts, leading to a lower effective Young's modulus of the cell. The material model used was linear elastic under small deformations with the material parameters obtained from the macroscopic characterization of PA12 reported in Cobian et al., 2022 and in Chapter 4, with an elastic modulus of 1.59 GPa and a Poisson's ratio of 0.4. A strain of -0.1 was imposed in the z-direction, and the simulations were performed under strain control.

Simulation of full lattice specimens

The 10x10x10 lattice CAD design compression tests were simulated with FE simulations using the commercial software *Abaqus*. FEM is used because, in these simulations, attention was not paid to local fields or defects but to the global response, and adaptive finite element meshes allowed a more accurate description of the strut's behavior for the exact discretization than a voxelized model. Quadratic tetrahedral elements (C3D10) with full integration were used. The material model and material parameters used and the strain conditions were the ones mentioned at the beginning of section 5.2.2.3. The volume was constrained in x and y in the top and bottom faces, and the movement was controlled in the top face, as these were the boundary conditions that best fit the behavior during the experimental compression tests.

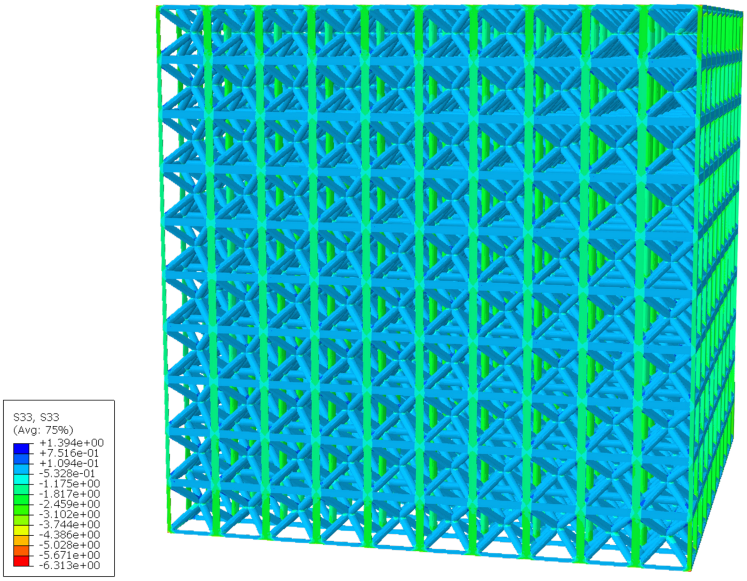

Figure 5.6: Stress map of lattice 10x10x10, simulated with FEM. Stress units in MPa.

An image of the stress map on the designed lattice geometry used for the simulation is shown in Figure 5.6. With the constraint boundaries at the top and bottom faces, the behavior of the lattice during the experimental compression test is captured with precision, as the lattice presents a slight barreling effect during the simulation and experiments. The effective elastic modulus obtained from the numerical simulation is 47.95 MPa, 25 % higher than the experimental results, which was $\approx$ 36 MPa.

Unit cells simulations

The summary of the results obtained in the simulation of the unit cells obtained from the tomographic and defect-free (CAD) RVEs are shown in Table 5.7. Results include the effective Young's modulus obtained by introducing the macroscopic measured Young's modulus ($E_{macro} = 1590$MPa) and the effective Young's modulus of the cell obtained using the cell microstructure from tomography (including surface roughness and internal defects) or

a defect-free perfect lattice. The general trend observed is that the experimental results in Table 5.2 are 50 %-75 % lower than the results obtained, assuming Young's modulus equal to the macroscopic value E_{macro}. To further quantify these differences, the table includes, for each cell, the value of Young's modulus of the material in the unit cell, which provides an effective Young's modulus of the cell equal to the one measured experimentally. These values of Young's modulus are named using the diameter of the cell ($E_{diameter} = E_{0.5}, E_{0.7}, E_{1.0}, E_{1.5}$).

It can be observed that Young's modulus $E_{diameter}$ required to match the experimental values depends on the sample size and increases with it, being 75 % lower than the macroscopic for the 0.5 mm strut cell and 50 % lower for the 1.5 mm strut cell. Note that this type of discrepancy was observed in Amani et al., 2018 and Youssef et al., 2005 for different types of cellular materials.

The differences found between the effective Young's modulus of a cell using the ideal CAD geometry and the actual tomographic microstructure, including surface roughness and porosity, are close, with a maximum deviation of $\approx$ 10 %. Moreover, in the case of the largest unit cell in which tomographic microstructure is measured (1.5 mm diameter struts), the stiffness of the cell using the actual microstructure obtained from X-ray tomography is higher than the one obtained using the defect-free cad geometry. This difference is probably due to the dimension variations between 3D printed cells and CAD volumes. Table 5.4 shows the values of strut diameter obtained from single struts measurements, not the struts of unit cells, as it is more difficult to measure correctly the strut diameter in unit cells. It has been seen that unit cells with theoretical 1.5 mm struts present larger diameters in real life than single struts, which is a dimension variation between as-designed (CAD) and printed volumes.

Table 5.7: Effective elastic modulus predictions of unit cells using defect-free (CAD design) and tomographic RVEs. Material parameters are inputs for the material model, and the predicted stiffness is the one obtained in the simulation. E_{macro} represents the effective Young's modulus value obtained from the macroscopic characterization, whereas $E_{diameter}$ is the input material parameter used with each of the respective RVEs to obtain the closest values to the experimental results of the respective unit cell sizes.

RVE	Material parameter [MPa]	Predicted effective E [MPa]
As-designed (defect-free)	$E_{macro} = 1590$	85.15
Tomo 0.5 mm	$E_{macro} = 1590$	79.15
	$E_{0.5} = 410$	20.41
Tomo 0.7 mm	$E_{macro} = 1590$	80.35
	$E_{0.7} = 580$	29.31
Tomo 1.0 mm	$E_{macro} = 1590$	76.51
	$E_{1.0} = 600$	28.87
Tomo 1.5 mm	$E_{macro} = 1590$	91.46
	$E_{1.5} = 820$	47.17

Finally, to show the effect of the porosity and cell geometry on the stress distribution, the normal component of the stress tensor in the loading directions is represented in Figure 5.7 for the four cells analyzed. As the cell size decreases, the defects become coarser due to the

relation between the sample and average particle size (55 µm). Therefore, the stresses on the vertical struts become less homogeneously distributed, where some topological features, such as pores, act as stress concentration regions. This effect can be notoriously differentiated between 5.7a and 5.7d.

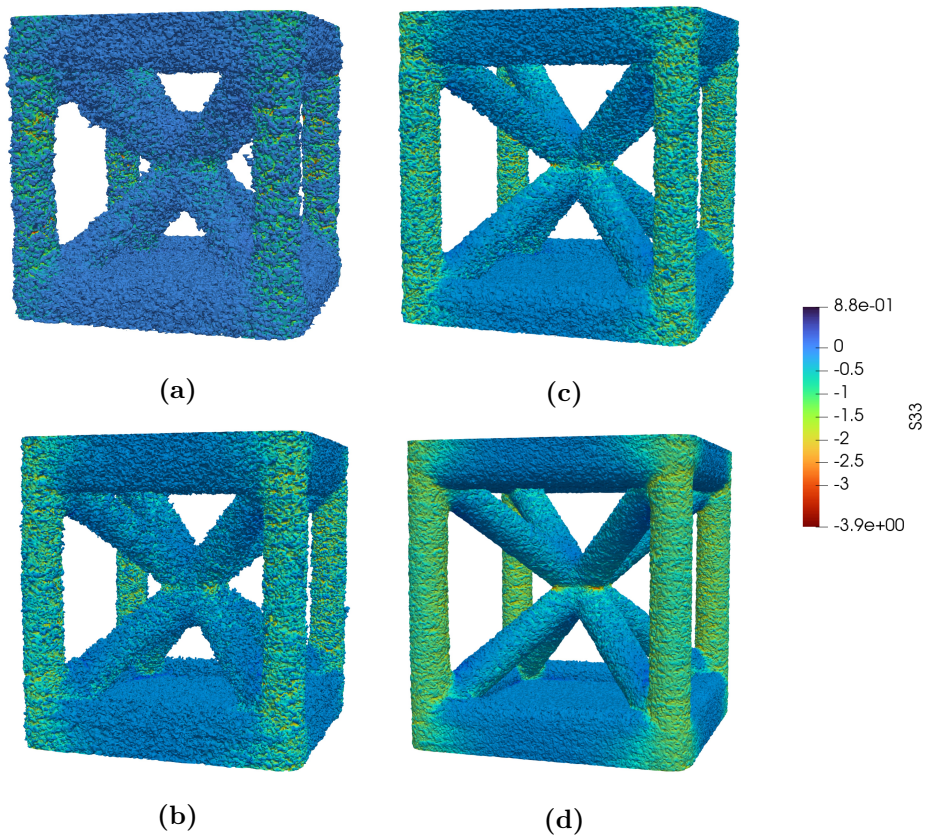

Figure 5.7: Stress maps over tomographic RVEs of unit cells with diameter struts of a) 0.5 mm, b) 0.7 mm, c) 1.0 mm and d) 1.5 mm. Stress units in MPa.

5.2.2.4 Summary

Experimentally, the porosity and surface roughness were analyzed by SEM and X-ray tomography. Figure 5.5 shows that the average pore size and surface roughness are almost identical in all samples, so the specimens with the smallest diameter present the largest defect size/diameter ratio and qualitatively might be more affected by these features.

The results of the simulations using the voxelized tomographies of the as-printed cells show that if the same material parameters are used for the as-designed cell (defect-free) and the actual as-printed cells, including the defects, the predicted effective Young's modulus of the real cells is only 10 % below the value of the as-designed cell for all strut sizes, as observed on Table 5.7. Therefore, it can be concluded that the effect of the defects is not enough to justify solely why the experimental effective elastic modulus of the unit cells, shown in Table 5.2, is around 50 % lower than the predicted numerical results using the tomographic volumes and material parameters from macroscopic tests.

To estimate the actual PA12 elastic properties that result in numerical responses identical to the experimental ones, the *elastic parameters* ($E_{diameter}$) that match the model predictions and the experimental values were computed. The results are shown in Table 5.7, and show how $E_{diameter}$ becomes closer to E_{macro} as the sample size increases, regardless of the effect the defects may have on the sample mechanical behavior. This reduction of the effective Young's modulus is observed in all the small unit cells. On the contrary, the largest unit cell (5.0 mm strut diameter, in the order of macroscopic specimens) presents the same stiffness as the one predicted for the as-designed RVE (Table 5.7).

This analysis concludes that porosity and surface roughness have a limited effect on the weaker response of smaller specimens (maximum 10 %), and their presence cannot uniquely justify the reduction of modulus found experimentally with respect to macroscopic cells. Therefore, the PA12 in the cells fabricated in different sizes must have a different behavior than the one resulting in fabricating a macroscopic specimen. This difference can be due to insufficient melting and particle coalescence during printing or differences in the PA12 nanostructure due to the different thermal histories suffered. Different micro-characterization techniques were used to analyze and quantify these features, and the discussion of these results is provided next, in section 5.2.3.

5.2.3 Effect of particle coalescence and annealing during additive manufacturing

In the previous section, it was found that porosity and surface roughness have a minimal impact (up to 10 %) on the reduced stiffness response of the microscopic scale specimens, suggesting other influencing factors like incomplete melting, particle coalescence, or changes in PA12 nanostructure from varying thermal histories, as mentioned in section 1.4.

The microstructure was analyzed by nanoindentation mapping together with optical microscopy in powders, lattice, and macroscopic material to evaluate the coalescence between particles and different structures present on the surface. To analyze in detail the internal nanostructure, such as crystallinity and phase transitions, as well as study the thermal history of all the additive manufacture samples, powder and printed PA12 material in different shapes and sizes were subjected to differential scanning calorimetry (DSC) analysis and small (SAXS) and wide (WAXS) angle X-ray scattering analysis. The analysis was done on samples from the powders used to 3D print the specimens, struts of diameters 0.5, 0.7, 1.0, and 1.5 mm, 1 mm diameter lattice struts, and the macroscopic bulk material. In the case of DSC, a macroscopic sample aged for 41 months was also analyzed.

The samples were taken from virgin powder (P.new), remaining powder after a printing process, named old powder (P.old), 3D printed macroscopic PA12 material (Macro), struts of all diameters (0.5 to 1.5 mm), and struts from lattices (0.5 L and 1.0 L). The struts come from single strut specimens and also from the lattices.

For this section, the samples will be addressed by the names given between the parenthesis.

Two additional samples went through this analysis to investigate the cooling rate's influence on the microstructure's evolution during solidification and to understand better the results

from WAXS, SAXS, and DSC experiments. Two portions of the same powder used to 3D print the samples (50/50 ratio of P.new and P.old) were melted at 220 ℃ in a hot press without applying pressure. One sample was left cooling inside the hot press with a cooling rate of around 5 ℃/min, and the other sample was quenched at room temperature between two steel plates. These extra samples are addressed as M.s and M.q for the melts subjected to a slow cooling rate and quenched, respectively.

5.2.3.1 Microstructural characterization by nanoindentation mapping

Nanoindentation modulus maps were carried out to characterize the microstructure's different phase distribution in the material. The measurements were taken from polished cross-sections of bulk material, struts, and powders to identify the different structures present and evaluate the coalescence between powder particles. Specimens of powders, struts, and bulk material were embedded in epoxy resin, and their surface was ground and polished down to 1 µm diamond paste to expose a smooth material surface suitable for nanoindentation measurements.

Nanoindentation maps were done using a *Hysitron TI950 Triboindenter* from *Bruker (US)*, fitted with a diamond Berkovich indenter calibrated with a standard fused silica sample. Nanoindentation modulus maps were obtained by performing 20 x 20 nanoindentations spaced 3.8 µm over an area size of 72.2 x 72.2 μm^2, with maximum loads of 1.5 mN, and loading, holding, and unloading times of 0.1 s.

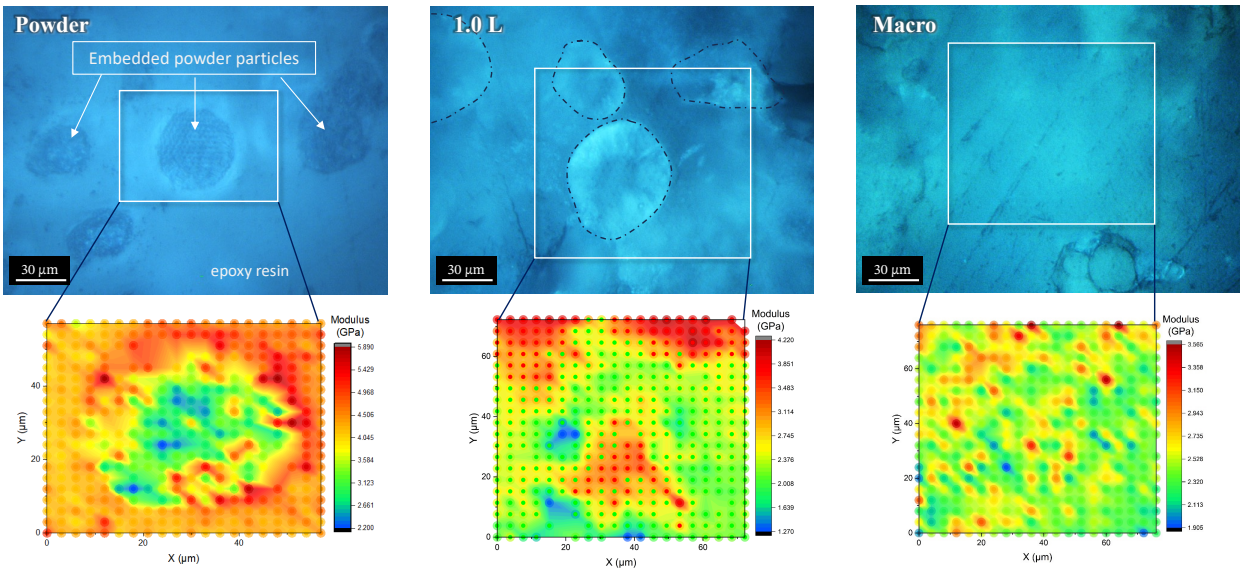

(a) **(b)** **(c)**

Figure 5.8: Optical microscopy images (up) and micromechanical maps (down) obtained by nanoindentation of (a) powders, (b) node from a 1.0 mm strut diameter lattice structure, and (c) macroscopic sample. The rectangle on the optical microscopy images represents the area corresponding to the nanoindentation maps.

Optical microscopy images of the polished sample surfaces prepared for nanoindentation alongside the nanoindentation modulus maps of the powder, node of the lattice with 1.0

mm diameter struts, and a macroscopic sample are shown in Figures 5.8a, 5.8b and 5.8c respectively. In the optical microscopy images, particles are observed in the three types of samples. In the case of raw powder, the powder particles are mounted in an epoxy matrix. In the 3D printed samples (strut and macro), unmelted and partially melted particles are found on the surface embedded in a matrix of fused material. Unmelted particles are observed as round areas of a darker color delimited with the matrix, where a continuous interface is observed, as in the optical microscopy images from Figure 5.8b on the middle and Figure 5.8c at the bottom center-right. Unmelted particles present the same shape and size as the particles in the raw powder samples, with an approximate diameter of 50 µm. Partially melted powder particles are observed in Figure 5.8b as rounded areas where part of the particle is delimited by the matrix, but other particle areas are gradually fused with the matrix. In this case, the interface observed is discontinuous. On the sample obtained from the lattice, the matrix presents color heterogeneities corresponding to partially melted powders, with unmelted particles also frequently present. On the other hand, the macroscopic sample presents a uniform and continuous matrix (see Figure 5.8c) where unmelted or partially melted particles can also be observed but are less common.

The nanoindentation map corresponding to the powder particle is shown in Figure 5.8a. The particles present an effective Young's modulus with a uniform distribution and an average value of 3.26 GPa, which is surrounded by an epoxy matrix with a modulus value surpassing 4.5 GPa. The powder particles are embedded in epoxy resin, which is stiffer than PA12. Figure 5.8b presents a nanoindentation map made over a node of a lattice with 1.0 mm diameter struts, where the unmelted particle presents a nucleus with an average modulus value of 3.40 GPa, stiffer than the surrounding matrix, which presents similar values to the matrix with fused particles corresponding to the macroscopic sample, with a modulus of $\approx$ 2.45 GPa. A nanoindentation map of the macroscopic material is shown in Figure 5.8c, where a uniform distribution of the effective elastic modulus is observed with an average value of 2.61 GPa, representing a wide area of completely melted particles. The value from the macroscopic sample coincides with the values reported in section 4.3, where nanoindentation values are compared with the values obtained from the characterization of bulk macroscopic PA12 samples. The average values of the particles and matrix of each sample are presented in Table 5.8.

Table 5.8: PA12 average modulus of powder, strut, and macroscopic samples nanoindented areas.

	Powder	**Strut**	**Macro**
Particles Modulus (GPa)	3.26 ± 0.53	3.4 ± 0.1	–
Matrix Modulus (GPa)	–	2.45 ± 0.05	2.61 ± 0.25

5.2.3.2 Differential scanning calorimetry

Samples weighing around 5mg were introduced in a *Q200* differential scanning calorimeter from *TA instruments* to perform DSC. The samples were subjected to a heating - cooling - heating cycle with a heating/cooling rate of 10 ℃/min. The maximum heating temperature was set to 210 ℃ and the minimum was set to room temperature.

Figure 5.9a shows the full DSC curve obtained from the heating-cooling-heating cycle of old powder, where the y-axis is inverted, with positive values representing endothermic processes. There are 3 main peaks: two endothermic, corresponding to the melting processes, and one exothermic, corresponding to the crystallization process. Regarding the other samples, the position and shape of the second peak, obtained during the cooling cycle, and the third peak, obtained during the second heating step, are similar for all. On the contrary, the position and shape of the first peak that appears during the first heating process depends on each sample and is shown in Figure 5.9b. The melting and crystallization temperatures are obtained from the location of the maximum of the endothermic and exothermic peaks, respectively. After the first melt, the material crystallizes in the range of 146 - 147 ℃, except for the virgin powder, which crystallizes at ≈150 ℃. The measured crystallization temperatures are close to the value found in the work by Kwiatkowska et al., 2020. On the other hand, the second melt occurs at 177 ℃ on all samples, which coincides with the melting temperature reported in the specification sheet of the virgin powder EOS PA2200.

The 3D printed samples present two melting peaks; the first melting point (T_{m1}) is in the range of 180 -184 ℃, and the second (T_{m2}) is in the range of 187-188 ℃, with no difference between the struts, the macroscopic or the macroscopic aged sample. On the other hand, the powders present only one melting peak, with their maximum at 183.7 ℃ for the virgin powder (P.new) and 186.2 ℃ for the old powder (P.old). For the melt samples, slowly cooled (M.s) and quenched (M.q), the melting point appears at a lower temperature of ≈ 177 ℃, which is similar to the values found in the literature (Kwiatkowska et al., 2020) and coincides with the melting temperature during the second heating process of all samples as the thermal history or aging in a polymer resets when it is melted. Table 5.9 shows the melting points, melting enthalpy, and crystallinity of all samples.

Table 5.9: Melting points, melting enthalpy and crystallinity of powders, melt samples, and 3D printed samples.

Sample	T_{m1} [℃]	T_{m2} [℃]	ΔH_m [J/g]	χ_c [%]
P.new	183.7	–	127.7	61.0
P.old	186.2	–	106.2	50.7
0.5 mm	181.0	186.6	102.7	49.1
0.7 mm	183.7	188.1	103.4	49.4
1.0 mm	182.1	187.4	107.2	51.2
1.5 mm	184.3	189.6	92.7	44.3
0.5 L	179.5	186.7	104.2	49.8
1.0 L	183.8	188.8	98.7	47.1
Macro	183.4	188.1	106.8	51.0
Aged	179.2	186.4	96.9	46.3
M.s	176.5	–	79.5	38.0
M.q	177.1	–	67.6	32.3

Melting enthalpy (ΔH_m) is in the range of 101-105 J/g for the 3D printed samples. The virgin powder presents the highest ΔH_m, with a value of 127.7 J/g, whereas the melt samples present the lowest values: 67.6 and 79.5 J/g for the quenched and slow-cooled, respectively.

The crystallinity degree was calculated from ΔH_m, being in the range of 48-50 % for most of the 3D printed samples, again, with no significant difference between the microscopic samples, the bulk, and the macroscopic aged sample. The virgin powder presents a crystallinity of 61 %, whereas melt samples present the lowest crystallinities, which are in the range of 32-38 %. Melting enthalpy and crystallinity are shown in Table 5.9.

Depending on the type of sample type (strut, cell, or full lattice) and its size, the endothermic peaks during the first heating cycle (see Figure 5.9b) present different positions and shapes. Crystallinity and the presence of different crystalline phases in the specimens can be estimated from this data and are directly related to the unmelted fraction of powders in the samples.

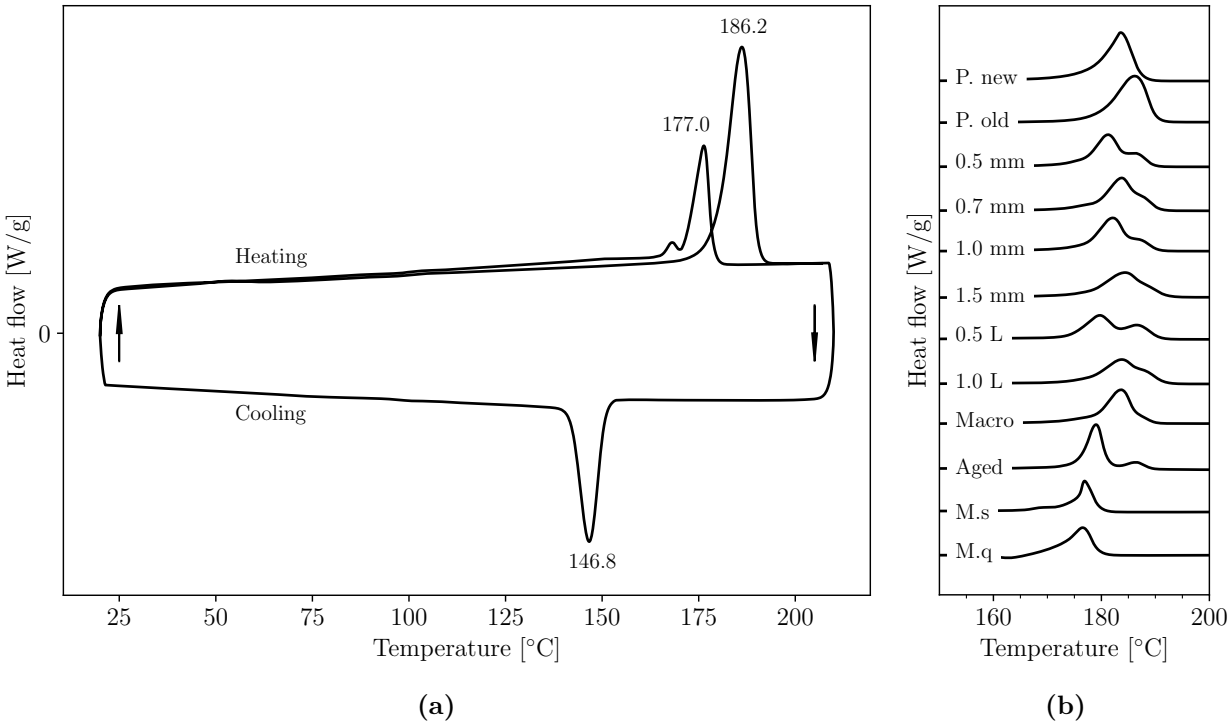

Figure 5.9: DSC thermograms of PA12 samples. The y-axis is inverted. (a) Full DSC curve from old powders and (b) melting peaks of all samples.

In the 3D printed samples, two melting peaks are usually found (Figure 5.9b), indicating the co-existence of two phases, while in the raw powder, only a single peak is observed. The position of the second peak emerging at a higher temperature in the printed specimens coincides with the position of the peak in the powders. The presence of these two peaks is a clear indication of the presence of unmelted or partially melted powder particles with an unmelted nucleus (Dadbakhsh et al., 2017; Zarringhalam et al., 2006), represented by the second peak at 187-188 ℃. On single struts, the second peak's height decreases with sample size until it becomes barely noticeable in the bulk sample (Macro), where full melting is expected. On the melted samples (M.s and M.q), the presence of a single peak indicates that all the powders were fully melted during the elaboration of the samples.

5.2.3.3 Small and wide-angle X-ray scattering

The crystallinity degree, phase transitions, and the effect of the thermal history of all the samples characterized with DSC were also analyzed with small (SAXS) and wide (WAXS) angle X-ray scattering. SAXS and WAXS analyses were conducted using a *SAXSpoint 5.0 Anton Paar laboratory* beamline with nickel-filtered CuKα radiation and X-ray wavelength of 0.15418 nm. The 2D patterns were obtained in a vacuum below 1 mbar and at room temperature. The specimens were fixed to a sample holder placed 60 mm and 800 mm away from the detector for WAXS and SAXS, respectively. The 2D data was post-processed to calculate crystallinity, d-spacing, and peak position corresponding to different crystalline phases in the case of WAXS patterns, as well as long spacing thickness and its distribution from SAXS patterns.

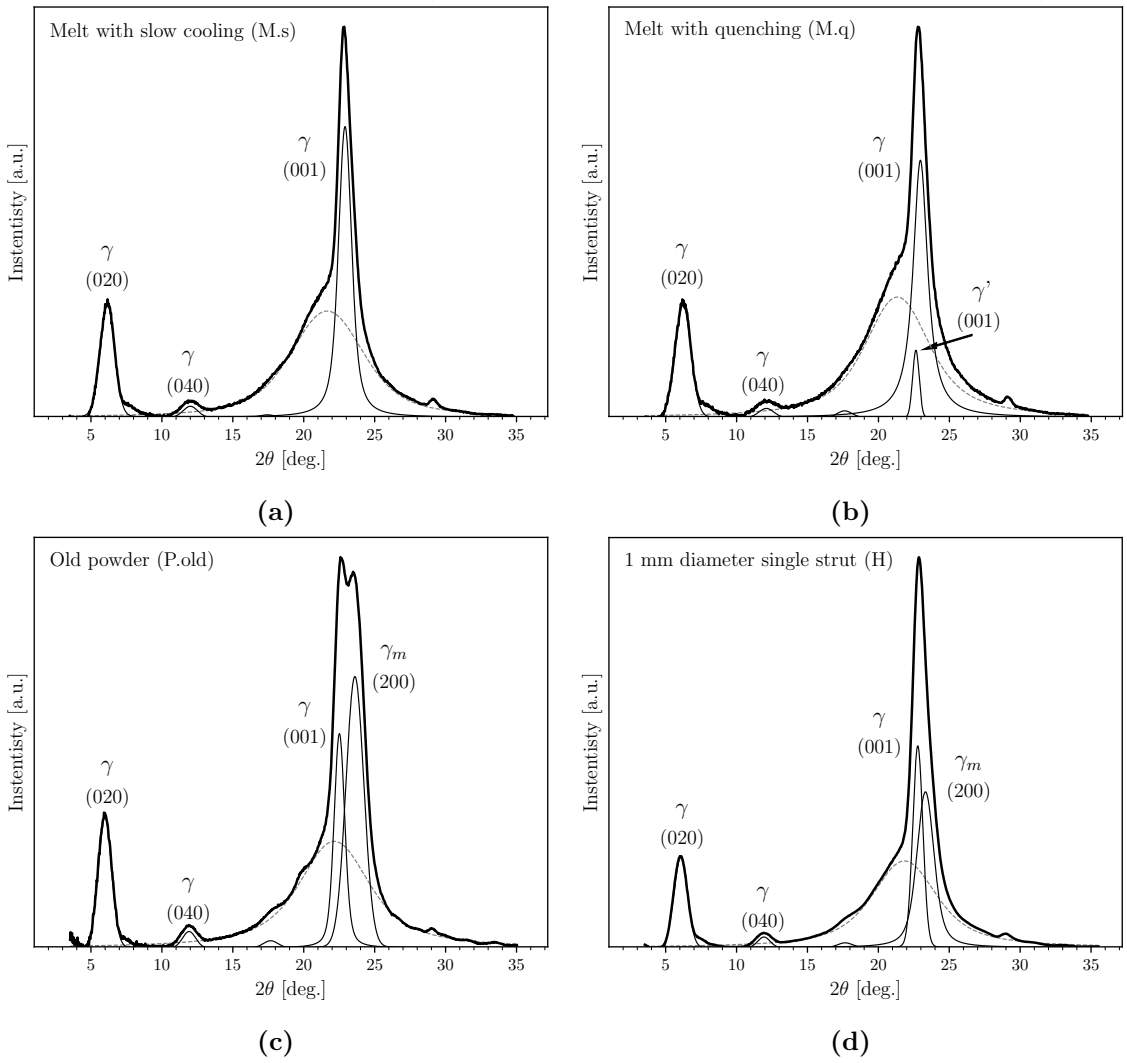

Figure 5.10: Graphs presenting WAXS patterns, peak deconvolution, and identification of the crystalline peaks and amorphous phase (discontinuous line) of PA12 samples of (a) melt with slow cooling (M.s), (b) melt and quenched (M.q), (c) old powder and (d) 1 mm diameter single strut.

The samples were characterized by WAXS and SAXS to identify the crystalline phases that appear in the 3D printed samples, compare them with the ones that are present in the melt samples, and calculate d-spacing values and the long spacing thickness (L). WAXS patterns and crystalline peaks identification of the old powder, melt samples (M.s and M.q), and a 1.0 mm diameter single strut are shown in Figure 5.10. The WAXS patterns of all the samples can be consulted in the additional material. It is important to mention that, due to the sandblasting effect on the 0.5L lattice and the difficult extraction and manipulation of its struts, 0.5L struts were not analyzed with WAXS and SAXS.

All analyzed samples present two strong peaks: (020) and (001) at $\approx 6.0°$ and 22.7° respectively, and a weak reflection (040) at $\approx 11.9°$, all corresponding to the γ crystalline phase. The melt sample with slow cooling (M.s) presents the three peaks mentioned (Figure 5.10a), which shows the standard WAXS pattern of PA12 subjected to slow cooling. The melt and quenched sample (M.q) presents a peak at 22.9°, corresponding to the mesomorphic γ' (Figure 5.10b). In addition, at approximately 29° there is a scattering peak that could be related to the additives present in *EOS PA2200* to enhance its printability, as no literature has been found about a peak in this region related to PA12.

On the powders and 3D printed samples, a fourth additional scattering peak is present, identified at $\approx 23.5°$ as the (200) peak, related to a metastable modification, γ_m, of the γ crystalline phase (Chen et al., 2018). In both new and old powders, the intensity of γ_m peak is higher than the $\gamma_{(001)}$ peak one (Figure 5.10c), whereas for the 3D printed samples, the $\gamma_{(001)}$ peak is more intense than the γ_m peak (Figure 5.10d). The intensity of the γ_m peak on the 3D printed samples decreases, becoming indistinguishable as the diameter or size of the sample increases. In contrast, the $\gamma_{(001)}$ peak becomes more prominent, as it can be observed in the WAXS patterns present in the additional material. The peak's intensity difference was calculated with the percentage difference formula between $\gamma_{(001)}$ and γ_m peaks. Figure 5.11a shows the intensity difference between the $\gamma_{(001)}$ and γ_m peaks, where positive y-axis values indicate that the $\gamma_{(001)}$ peak presents a higher intensity than the γ_m peak. The letters H, V, and T in the sample names represent the layer directions perpendicular, parallel, and oblique to the strut length. As mentioned before, the strut diameter depends on the printing direction, and in general, the diameter goes like H > V > T. Figure 5.11a shows a clear trend where the γ_m peak's intensity decreases with respect to the $\gamma_{(001)}$ peak as the diameter of the sample size increases as well as the sample size; the height difference corresponding to a strut of the full lattice with struts of 1mm is also shown. In this case, it can be observed that this value is near to the bulk specimen and considerably higher than the struts fabricated isolated.

From the WAXS patterns, d-spacings (d) are estimated using equation 2.7 and represented in Figure 5.11b. In most of the phases and directions there is no correlation between d-spacings and the sample size, and the variation is less than 2 %. The exception are the $\gamma_{(001)}$ and γ_m directions. For $\gamma_{(001)}$ direction, the calculated d-spacing is around 3.95 Å in the powders, slightly lower in the old powders, and 3.90 Å in the struts, which increases slightly with the sample size until it reaches 3.91Å in the macroscopic samples, which can be observed in Figure 5.11b. On the contrary, in the γ_m direction, the d-spacing decreases slightly with the sample size, starting from 3.82 Å for the 0.5 mm struts until it reaches 3.77 Å for the macroscopic sample. In addition, the virgin powder presents the lowest d-spacing on the

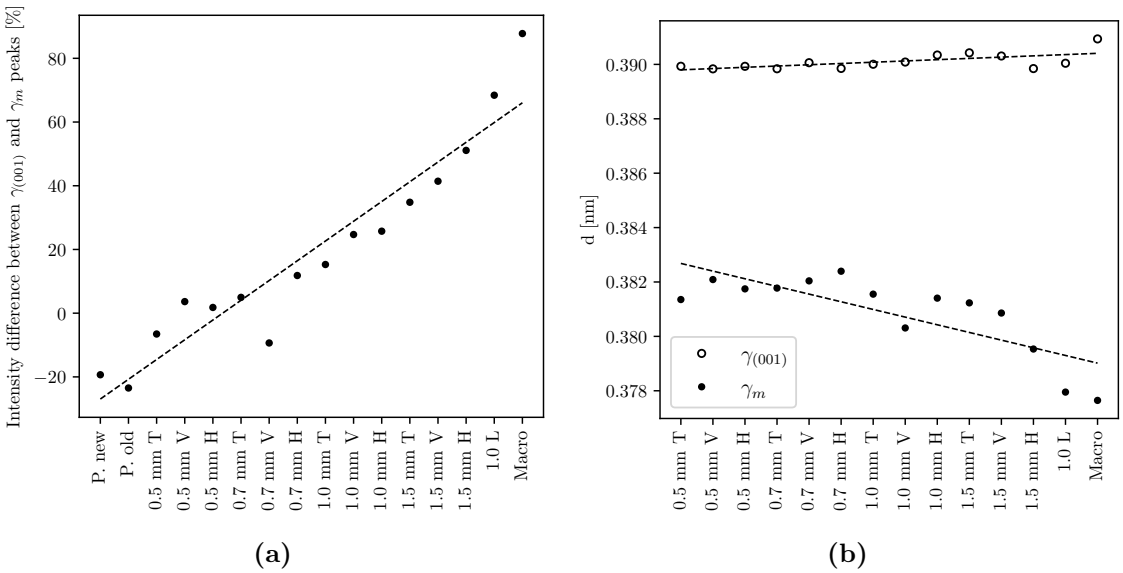

Figure 5.11: Graphs obtained from WAXS patterns of a) height difference between $\gamma_{(001)}$ and γ_m peaks of all samples, and b) evolution of d-spacings calculated for $\gamma_{(001)}$ and γ_m directions from printed samples only.

γ_m direction, with a value of 3.74 Å, whereas the old powder value is 3.77 Å. The average estimated d-spacing values of the γ_m and $\gamma_{(001)}$ directions, 3.80 and 3.90 Å are in accordance with the values of Ma et al., 2020.

Crystallinity values were also estimated from WAXS patterns using equation 2.10. The results were in accordance with the ones calculated from DSC curves, shown in Table 5.9.

SAXS patterns of powders, the macroscopic material, and 1 mm struts coming from the lattice and single strut samples are shown in Figure 5.12a. The peaks observed are related to the long spacing thickness. All the samples present a peak at $\approx 0.55\ nm^{-1}$, and as the sample size increases, a second peak emerges at $\approx 0.4\ nm^{-1}$. It is observed how the powders present a small peak in comparison with the 3D-printed samples.

In addition, the peak broadens with the sample size. From the peak maximum of SAXS patterns, the lamellar thickness was estimated using equations 2.8 and 2.7. The evolution of the long spacing with the sample size is shown in Figure 5.12b. When the sample presented two peaks with approximately the same intensity, the average between the values obtained from both peaks was calculated to get the lamellar thickness. There is an increasing trend in the observed thickness with the sample size, from 12 nm of the powders and smaller diameter struts up to 15 nm for the largest samples, a 25 % increase.

WAXS and SAXS results were used to analyze the crystalline phases present for the different cell sizes and their characteristics. All the samples present the γ phase, but only the quenched sample presents the mesomorphic γ' phase. This indicates that all the 3D printed samples, from struts to macroscopic samples, have been subjected to slow cooling.

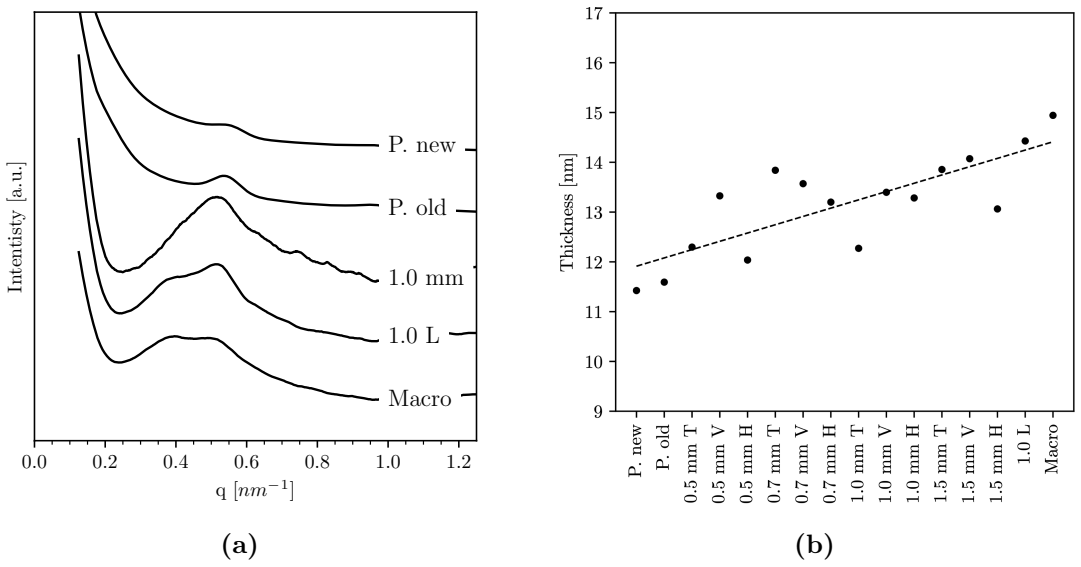

(a) **(b)**

Figure 5.12: Graphs from SAXS showing a) SAXS patterns of powders and all 1 mm struts obtained from different geometries, and b) long spacing thickness estimations.

All the WAXS patterns from the 3D printed samples present the peaks observed in Figures 5.10c and 5.10d. The peak γ_m presents the highest intensity in the powders, and although this phase is thermally metastable, the powders have been produced by solution-precipitation, where γ_m is stable (Dadbakhsh et al., 2017). Moreover, it has been observed how the γ_m, stable in powder, fades away and evolves progressively towards the stable $\gamma_{(001)}$ as the sample size increases, as shown in Figure 5.11 and the rest of the graphs included in Annex 3. This evolution of the γ_m peak on 3D printed samples, and the fact that γ_m is absent in the melted M.s sample, where it was ensured that the particles were fully melted, reinforces the hypotheses that the 3D printed samples contain a fraction of unmelted or partially melted powder. This fraction increases as the sample becomes smaller, and the γ_m peak appears higher as the fraction of poorly sintered powders increases in the sample. If the sample is composed of partially melted powders, the powders are joined by necks located in the region where the powders have sintered. As the cross-section decreases, there is less surface that is printed with the hatching parameters resulting in larger amounts of unmelted or partially melted particles and poor bonding quality between them (Hejmady et al., 2022).

5.2.3.4 Summary

Besides the roughness, one of the main differences between macroscopic and microscopic cells that can be observed by the optical microscopy images and nanoindentation maps (Figure 5.8) is the presence of unmelted particles or partially melted particles. These particles may not be well bonded to the interior of the struts and might reduce the effective cross-section of the struts.

The origin of unmelted particles is related to the resolution of the machine with respect to the strut diameter. In the case of samples that present struts with small diameters (0.5 to 1.5 mm), the dimensions are close to the minimum resolution the machine can achieve.

In fact, the laser spot size is 0.4 mm, which is very close to the dimensions of the struts. When a strut is printed with diameters below 0.96 mm, the machine can only use the contour process parameters to manufacture them, as the strut diameters are too small to use hatching parameters. As the cross-section diameter increases, the fraction of the sintered material surface during the hatching step increases, resulting in more material manufactured with the optimal process parameters. Contour strategies typically use a lower energy density than hatching because the primary goal is to ensure precision than building bulk material, which is the case of hatching strategies (Gibson et al., 2021). Using contour parameters to manufacture struts, either in unit cells or lattices, may not provide enough energy density to fully melt the powder particles and produce them. The result is struts with unmelted and partially melted particles on the surface and the interior, especially in the smallest diameter struts (0.5 and 0.7 mm). Some authors have already studied the effect of energy density on the particle melting of PA12 fabricated by PBF, showing the same trends found in this work. Zhu and Majewski, 2020 showed that due to insufficient energy, there is an incomplete melting of powders in PA12. Chatham et al. demonstrated that the ultimate tensile strength and Young modulus PA12 samples were drastically enhanced when they were printed with energy densities over a threshold value, which ensured the coalescence of melted powder particles during additive manufacturing (Chatham et al., 2021). It is also well reported that the strength of the union between particles depends on the quality of the coalescence (Chatham et al., 2021; Hejmady et al., 2022; Picard et al., 2020; Sun et al., 2008).

Although the lack of particle coalescence is observed in microscopic images, its degree and influence on the mechanical response cannot be quantified solely from these images. Moreover, other changes affecting the nanostructure of melted particles might have occurred during processing. To analyze the degree of coalescence of particles and the changes in the nanostructure during the processing of cells of different sizes, DSC, WAXS, and SAXS analyses were performed. From these analyses, it was concluded that the root cause for the reduction of stiffness and UCS is the presence of unmelted powder in the printed unit cells (0.5-1.5 mm diameter). Unmelted particles have been observed in the microscope images, and DSC and WAXS-SAXS experiments have shown that their volume fraction decays with increasing strut diameter due to non-ideal printing parameters, related to the use of the contour strategy, which uses less energy density on the material compared to the hatching strategy.

5.3 From unit cells to lattices

The substantial reduction found in the effective Young's modulus unit cells with smaller strut sizes is much more severe (up to 50 % reduction) than for macroscopic (large) specimens fabricated with unit cells having decreasing strut diameters. The effective Young's modulus of lattices was only 25 % lower than the one obtained numerically, assuming perfect lattices and strut material behaving as the one found in macroscopic specimens (see section 3.1). Since the same contour parameters used in cells are kept for lattices with the same strut diameters, full lattice specimens are also expected to have an important amount of unmelted particles. This fact is confirmed by DSC analysis, and in Figure 5.9b, it can be observed that the peak associated with unmelted powder is also present in lattice specimens. Therefore, the discrepancy in the mechanical behavior between unit cells and lattices should be related to

other features during fabrication and postprocessing, related to the large size and internal connectivity of the printed specimens. Two main potential factors are identified behind this discrepancy.

5.3.1 Postprocessing after manufacturing

Compared with the unit cells, the lattice core presents struts with diameters larger than the designed ones due to the diminished effect of the sandblasting process on that region, as shown in section 5.2.2.1. The lattice struts present a varying degree of sandblasting from the interior to the edge of the lattice, as observed in Figure 5.4, and the struts on the core present larger diameters than the edge and design diameter. This larger effective diameter could be associated with an increase in stiffness.

However, it is more probable that the larger diameters in the interior of the lattice are related to the attached entrapped powder that was not removed during the sandblasting process. Therefore, this apparently larger diameter does not contribute to an effective increase in the load-bearing capacity of the struts that could affect the mechanical properties.

5.3.2 Annealing effect during additive manufacturing on the lattices

Assuming a small effect of the apparent larger diameter on the response, the smaller reduction of stiffness of lattices (25 % deviation from bulk) respect unit cells (50 % deviation from bulk) have to be related to the nanostructure of the resulting material, affected by the different thermal histories suffered during fabrication.

There is wide experimental evidence about the effect of thermal history during processing, which resembles an annealing treatment and determines the quality and mechanical properties of PA12 components fabricated with additive manufacturing (Li et al., 2021; Salmoria et al., 2012; Zhu and Majewski, 2020). The different thermal history between samples with different overall sizes is related to the number of times the laser passes through the same area, originating heat-affected zones in the neighboring areas, which are influenced by the thermal cycles produced by the passing of the laser. If the sample size decreases, the laser will pass fewer times through the same area, reducing the thermal cycles in the heat-affected zone and the number of times the area is re-melted (Lupone et al., 2021). The minimum laser diameter in EOS Formiga P100 is 0.4 mm, and in this work, unit cells and lattices made with struts (with diameters of 0.5, 0.7, and 1 mm) that present dimensions close to the minimum resolution are analyzed. It is to be expected that the laser will pass fewer times per layer when making a 0.5 mm single strut sample than when making a lattice with 0.5 mm struts with larger overall sample dimensions, where the laser will pass more times across the neighboring areas of a given point, which resembles an annealing process, as the amount of time the sample is subjected to high temperatures (globally and locally) depends on the sample size. Ferreira et al., 2020, Ali et al., 2021, and X. Liu et al., 2021 reported an increase in mechanical properties with annealing, suggesting that the annealing degree between the macroscopic-sized (lattices) and microscopic-sized (unit cells) samples could be the main cause for the difference in mechanical behavior between samples with struts of the same diameter. It is important to mention that coalescence between two polymer particles is

driven by thermal energy, and during the sintering process, the surface of the particles come in contact and fuse together, forming a neck that grows at a rate that depends on the molecular diffusion, randomization, and crystallization of the polymer chains across the interface. The polymer chains need enough temperature and time to diffuse, randomize, and crystallize across the neck region, and the strength of the joint between particles depends on the quality of the coalescence (Chatham et al., 2021; Hejmady et al., 2022; Picard et al., 2020; Sun et al., 2008). In macroscopic-sized samples, such as lattices, the laser passes through the neighboring regions more times than in a unit cell sample with the same strut diameters, suggesting that the increasing annealing time with sample size can favor the diffusion, randomization, and crystallization of polymer chains in the neck region, improving the quality of the bonding between the polymer particles in the lattices. To validate this hypothesis and quantify the changes in the nanostructure of bonded particles, WAXS and SAXS results were further discussed in the next section.

Crystal structure analysis from WAXS and SAXS

As in the case of individual cell specimens, the WAXS patterns of full lattice specimens also show the presence of γ and γ_m, suggesting that there is also a portion of unmelted particles and partially melted particles poorly joined by a sintered region called the neck. The nanostructure of the sintered portion evolves differently for different sample sizes because the laser passes more times through the same area, increasing the annealing degree on the samples. As the annealing degree increases, γ_m evolves towards the preferred and stable $\gamma_{(001)}$ (see Figure 5.11b), which becomes notorious in the lattice and bulk sample, as high temperatures facilitate the chain mobility in the crystalline region (Chen et al., 2018). In the work by Chen et al., 2018, the same peak merging is reported and resembles this behavior in the Brill transition.

An indication reinforcing the hypothesis that the annealing degree depends on the sample size can be seen in the SAXS patterns in Figure 5.12, where it is observed how the annealing degree on the sample influences the long spacing. Figure 5.12b shows how the long spacing thickness increases with sample size, which indicates a higher annealing degree as the sample size increases. In addition, a peak broadening is observed in Figure 5.12a from the single strut to the macroscopic sample. This indicates that the lamellar thickness distribution increases with the sample size. These curves provide insight into the crystal structure evolution with the annealing degree. With a low annealing degree, the long spacing is about 13 nm (peak maximum at 0.5 nm^{-1}). As the annealing continues, some long spacings start to increase towards 15 nm (peak maximum at 0.35 nm^{-1}), but 13 nm spacing predominates, and, as the annealing continues, the crystal structure continues evolving towards the 15 nm spacing. This can be observed in the SAXS pattern of the 1.0 mm diameter strut lattice. In addition, the increase of long spacing towards 15 nm is related to the appearance of a second peak on the samples SAXS patterns, which indicates a rearrangement of the crystal structure, from γ_m towards the stable form, $\gamma_{(001)}$. It has been reported a long spacing increase from 8.5 to 15.9 nm for 50 to 100 h of annealing on PA12, which reinforces this estimation (S. Gogolewski and Gastorek, 1980).

5.3.2.1 Summary

On top of porosity and the effect of strut diameter, the size of the full specimen also plays an important role in the mechanical behavior of a lattice-based material. This can be observed by the very similar response of full lattice specimens with macroscopic dimensions (side lengths of 36 and 71 mm), made of cells with different strut diameters (1mm and 0.5mm), which, when fabricated as single cells, presented a strong size effect.

DSC thermographs indicate that both single cells and full lattice samples contain partially melted powder particles, but the struts from the lattices present a long spacing 15 % thicker than the single struts (Figure 5.12b) due to the different annealing degree between a sample with macroscopic dimensions and a single strut, although they present the same diameter. This suggests the thermal history of the lattices can be conditioned by their size. For this reason, the annealing degree, and thus the bonding quality of partially melted particles of unit cells and lattices, is different even if the diameter of the struts is kept the same.